POLITECNICO DI MILANO

Scuola di Ingegneria Industriale e dell'Informazione

Corso di Laurea Magistrale in Ingegneria Energetica

Dipartimento di Energia

Modelling and simulation of a scroll expander for micro-ORC applications

Relatore:
Ing. Antonio Giuffrida

Co-Relatore:
Ing. Davide Bonalumi

Autore:
Nicola Giupponi Matr. 801082

Anno Accademico 2014-2015

"Che il raggiungimento di questo traguardo

possa ispirare l'inseguimento di Sogni ancora più ambiziosi"

Ringraziamenti

Desidero ringraziare il Professor Antonio Giuffrida per avermi dato la possibilità di svolgere questo lavoro di tesi, che chiude il mio percorso formativo presso il POLITECNICO DI MILANO. Molto utili si sono rivelati i suoi consigli durante tutta la durata del progetto. Un doveroso ringraziamento va al dott. Miao Zheng e al preside Jinliang Xu della School of Mechanical and Power Engineering - North China Electric Power University di Beijing (Cina) per aver evitato allo scrivente una noiosa fase di digitizzazione dei dati da loro pubblicati.
Un grazie speciale va alla famiglia, agli amici e alle persone care che mi hanno sempre sostenuto nel corso degli anni.

Abstract

In the field of low-grade heat utilization, organic Rankine cycle (ORC) technology has gained enough worldwide attention in recent years. The Scroll expander is a good candidate for micro and small scale ORC applications because of its reliability, compact structure, few moving parts, lower level of noise and vibration than small-scale turbine expander which is also expensive and not commercially viable. This thesis proposes a useful tool for the micro-scale ORC plant designer in terms of a model to predict the performance of the scroll expander once the boundary conditions such as evaporation and condensation pressures, generator speed revolution and the working fluid are known. The work starts from an experimental campaign on a 4 kW open drive scroll compressor derived from the air conditioning system of a bus and modified to be operated as an expander in a ORC with R123 as working fluid. Then the expansion model is realized and presented with significant improvements from the thermodynamic point of view if compared to those present in the literature. The major revisions concerns the expander inlet pressure throttling, the heat loss to the surroundings and the mechanical power loss which occurs due to friction between the sliding metal spirals. For this purpose, an analogy with internal combustion engines as regards of the mean indicated pressure in the cylinder is used. After a calibration of the model over the most interesting experimental points from a mechanical power point of view, the next validation on the remaining experimental data was performed. Once the model parameters have been fixed, a numerical investigation on the performance of the scroll in a wide range of operation point was carried out. The results show that the expander efficiency is maximum when the expansion ratio is close to the adapted conditions, which depend on the internal geometry of the machine. The scroll expander cannot be considered an adiabatic machine because the thermal losses are comparable to the shaft power in all operating conditions. Superheating must be limited as much as possible because it does not bring about a gain in terms of mechanical power but increases the heat losses to the environment. 2D and 3D operation maps are plotted to provide a clear and straightforward overview of the investigated scroll expander performance. Finally, an exergy analysis is conducted to analyze the main irreversibility involved in the expansion processes. This last analysis points out that scroll expanders should have low leakages and good lubrication between the sliding spirals.

Keywords: *lumped-parameter model, non-adiabatic behavior, Organic Rankine Cycle (ORC), performance analysis, semi-empirical model, scroll expander*

Sommario

La macchina scroll come espansore dell'impianto micro-ORC è sempre più giustificata dalla sua affidabilità, dal numero ridotto di parti in movimento, bassa rumorosità e vibrazioni, se paragonate alle micro turbine che non sono ad oggi molto competitive. Questa tesi ha come obiettivo quello di realizzare uno strumento utile al progettista di impianti micro-ORC per prevedere le prestazioni dell'espansore scroll una volta note le condizioni al conorno quali le pressioni di evaporazione e condensazione, la velocità di rotazione del generatore elettrico e il fluido circolante nell'impianto. Il lavoro si basa su una campagna sperimentale effettuata su un compressore da 4 kW estratto dall'impianto di condizionamento di un pullman e modificato per essere impiegato come espansore in un impianto ORC che elabora R123. Il cuore del lavoro è la realizzazione di un modello di espansione che presenta sostanziali cambiamenti dal punto di vista termodinamico rispetto a quelli presenti in letteratura. Le maggiori modifiche riguardano la caduta di pressione all'aspirazione, le dissipazioni termiche verso l'ambiente e la modellazione delle perdite meccaniche delle spirali metalliche. Per questo scopo è stata utilizzata l'analogia con la pressione media indicata presente nel cilindro dei motori a combustione interna. Dopo una calibrazione del modello sui punti sperimentali che presentano un maggiore interesse dal punto di vista della produzione di potenza, si è proceduto con la validazione sui punti rimanenti per fissare i parametri del modello. Dopodichè è stato possibile effettuare un indagine numerica sull'intero campo di funzionamento dell'espansore. I risultati mostrano che il rendimento di espansione è massimo quando il rapporto di espansione è vicino a quello di "adattamento", che dipende dalle caratteristiche geometriche interne alla macchina. L'espansore non può considerarsi una macchina adiabatica in quanto le dispersioni termiche sono sempre paragonabili alla potenza utile in ogni condizione di funzionamento. Il surriscaldamento deve essere il più limitato possibile perchè non porta ad un guadagno di potenza estraibile ma aumenta le dispersioni termiche.
Inoltre sono presentate delle mappe di funzionamento 2D e 3D per consentire una chiara ed esaustiva panoramica sulle prestazioni dell'espansore in tutto il campo di funzionamento analizzato. Infine è stata effettuata un analisi exergetica per analizzare le principali irreversibilità dei processi coinvolti nell'espansione e ne risulta che gli espansori di tipo scroll dovrebbero avere bassi trafilamenti e una buona lubrificazione tra le spirali striscianti.

Parole chiave: *analisi prestazionale, ciclo Rankine a fluido Organico (ORC), comportamento non adiabatico, espansore scroll, modello a parametri concentrati, modello semi-empirico*

Riassunto esteso

Nel campo del recupero energetico da sorgenti termiche a bassa temperatura, il ciclo Rankine a fluido organico (ORC) ha guadagnato negli ultimi anni sempre più interesse con riferimento a potenze non superiori ai 10 kW. L'utilizzo di una macchina scroll come espansore del ciclo è sempre più giustificata dalla sua affidabilità, dal numero ridotto di parti in movimento, bassa rumorosità e vibrazioni, se paragonate alle micro turbine ad oggi molto più costose. Questo lavoro di tesi ha come obiettivo quello di realizzare un modello di espansione utile al progettista di impianti micro-ORC per prevedere le prestazioni dell'espansore scroll una volta note le condizioni al contorno quali le pressioni di evaporazione e condensazione del ciclo, la velocità di rotazione del generatore elettrico e il fluido circolante nell'impianto.
Il lavoro si fonda su una campagna sperimentale effettuata da Zheng et al. [25] su un impianto micro-ORC che elabora R123 e che impiega, come espansore del ciclo, un compressore scroll da 4 kW nominali proveniente dall'impianto di condizionamento di un pullman e modificato per essere impiegato come espansore. La campagna sperimentale ha permesso di osservare il comportamento dell'espansore scroll con diverse portate in massa, pressioni e temperature all'ingresso e all'uscita e numero di giri. Queste informanzioni sono tutte utilizzate come valori di riferimento per decretare l'accuratezza del modello di espansione proposto. Quest'ultimo infatti risulta essere il cuore di questo lavoro di tesi e si inquadra come un miglioramento di modelli presenti in letteratura che presentano però diverse lacune sia dal punto di vista termodinamico che prettamente meccanico. Con riferimento allo schema concettuale sottostante, Le trasformazioni che sono state considerate nel modello prevedono:

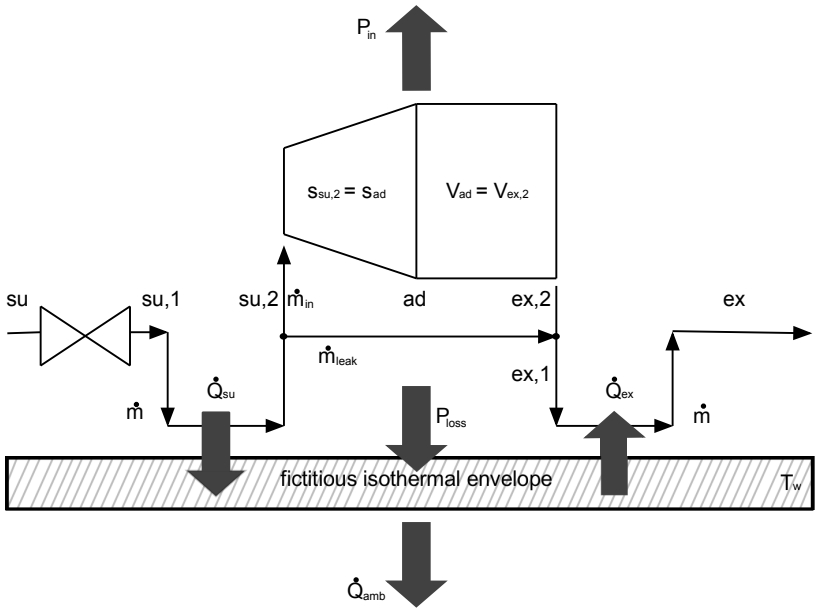

Schema concettuale del modello di espansione

- Laminazione isoentalpica in ingresso ($su \rightarrow su,1$): Tutte le perdite di pressione del fluido sono concentrate all'ingresso della macchina. Questo è giustificato dal fatto che durante il processo di ammissione, parte della sezione di passaggio a disposizione del fluido di lavoro (per l'ammissione nella cavità più interna racchiusa dalle due spirali) è parzialmente ostruita dal moto della spirale orbitante, con conseguente diminuzione della sezione utile a disposizione del fluido e incremento delle perdite di carico. Questa è la prima modifica apportata al modello proposto. In letteratura si adotta sorprendentemente una trasformazione isoentropica.

- Raffreddamento isobaro del fluido con l'involucro metallico della macchina ($su,1 \rightarrow su,2$): Questo scambio di calore, insieme al riscaldamento del fluido in uscita dalla macchina, porta ad avere una potenza termica trasferita molto elevata, nonostante la superficie di scambio dell'ordine dei centimetri quadrati. Questo è dato dal fatto che il fluido elaborato tra le spirali della macchina acquisisce una forte componente di squish, con una turbolenza tale che i coefficienti convettivi di scambio termico assumono valori molto più elevati rispetto a quelli suggeriti dalle correlazioni tradizionali per fluidi organici circolanti in tubi. Tale conclusione si basa sulla indagine CFD sugli scambi termici interni di un compressore scroll condotta da K.T.Ooi et al. [36].

Visione d'insieme delle principali formule adottate nel modello di espansore scroll

equazioni	**incognite**	**risultato**	**trasformazione**
$\mathring{m} = A_{su} \cdot \rho_{thr,su} \cdot \sqrt{2(h_{su} - h_{thr,su})}$ $h_{su,1} = h_{su}$	ρ,$h_{thr,su} = f(p_{su,1}, h_{su})$	$\mathring{m}$	$(su \rightarrow su, 1)$
$\mathring{Q}_{su} = \mathring{m} \cdot (h_{su,1} - h_{su,2}) = \left[1 - e^{\left(\frac{-AU_{su}}{\mathring{m} \cdot cp}\right)}\right] \cdot \mathring{m} \cdot cp \cdot (T_{su,1} - T_w)$	$AU_{su,nom}$; Tw	$\rho_{su,2}, h_{su,2} = f(p_{su,1}, T_{su,2})$	$(su, 1 \rightarrow su, 2)$
$AU_{su} = AU_{su,nom} \cdot \left(\frac{\mathring{m}}{\mathring{m}_{nom}}\right)^{0,8}$	-	-	-
$\mathring{m}_{leak} = A_{leak} \cdot \rho_{thr,su} \cdot \sqrt{2(h_{su,2} - h_{thr,leak})}$	$h_{thr,leak} = f(p_{thr,leak})$	$\mathring{m}_{leak}$	$(su, 2 \rightarrow ex, 2)$
$p_{thr,leak} = MAX(p_{ex,2}; p_{crit,leak})$	-	-	-
$p_{crit,leak} = p_{su,2} \cdot \left[\left(\frac{2}{\gamma+1}\right)^{\left(\frac{\gamma}{\gamma-1}\right)}\right]$	-	-	-
$\frac{\rho_{ad}}{\rho_{su,2}} = \frac{1}{BVR}$	-	$h_{ad} = f(\rho_{ad}, s_{su,2})$	$(su, 2 \rightarrow ad)$
$h_{ex,2} = h_{ad} - \frac{(p_{ad} - p_{cond})}{\rho_{ad}}$	-	$h_{ex,2}$	-
$\mathring{m}_{leak} \cdot h_{su,2} + \mathring{m}_{in} \cdot h_{ex,2} = (\mathring{m}_{leak} + \mathring{m}_{in}) \cdot h_{ex,1}$	-	$T_{ex,1} = f(p_{cond}, h_{ex,1})$	$(ex, 2 \rightarrow ex, 1)$
$\mathring{Q}_{ex} = \mathring{m} \cdot (h_{ex,1} - h_{ex}) = \left[1 - e^{\left(\frac{-AU_{ex}}{\mathring{m} \cdot cp}\right)}\right] \cdot \mathring{m} \cdot cp \cdot (T_{ex,1} - T_w)$	$AU_{ex,nom}$; Tw	h_{ex}	$(ex, 1 \rightarrow ex)$
$p_{me} = \rho_{ad} \cdot (h_{su,2} - h_{ex,2})$	-	-	-
$\omega_{loss} = (a + b \cdot N^n)$	-	.	-
$\mathring{P}_{loss} = p_{me} \cdot \omega_{loss} \cdot N$	-	-	-

- Espansione isoentropica ($su, 2 \rightarrow ad$): Parte dell'espansione è modellata come adiabatica reversibile, portando il fluido dalla pressione $su, 1$ alla condizione ad, che coinciderebbe con la condizione di adattamento della macchina, per cui non ci sarebbe differenza tra la pressione all'uscita delle camere di espansione e la pressione di scarico della macchina (che corrisponde a quella di condensazione).

- Espansione isovolumica ($ad \rightarrow ex, 2$): Per tutti gli altri casi in cui il rapporto di espansione è diverso da quello adattato, il modello prevede una espansione a volume costante che porta il fluido uscente dall'espansione isoentropica alla pressione di condensazione. Quest'ultima può essere superiore alla pressione di adattamento, e in questo caso la macchina si trova in condizioni di sovra-espansione, mentre se è inferiore alla pressione di adattamento, si è in condizioni di sotto-espansione. In termini di lavoro, la condizione di sovra-espansione decreta un peggioramento delle prestazioni più significativo rispetto al caso di sotto-espansione.

- Perdite di trafilamento ($su, 2 \rightarrow ex, 2$): Sono simulate per mezzo di un ugello semplicemente convergente e la portata è determinata dalla pressione che sussiste nella gola del suddetto convergente; Questa è la massima tra la pressione di condensazione e quella limite che innesca la condizione di blocco, per la quale la portata non può più aumentare.

- Miscelamento adiabatico ($ex, 2 \rightarrow ex, 1$): Questo avviene all'uscita dell'espansione a volume costante, alla pressione di condensazione, e vede coinvolti il flusso in condizioni $ex, 2$ e il flusso proveniente dalle perdite di trafilamento, alla pressione di gola del convergente.

- Riscaldamento o raffreddamento isobaro ($ex, 1 \rightarrow ex$): Come il riscaldamento illustrato sopra, la differenza sta nel fatto che il verso di questo flusso termico non è noto a priori in quanto dipende dalla temperatura dell' involucro metallico contenente le spirali.

Le equazioni che descrivono le trasformazioni appena introdotte sono riassunte nella Tabella per una chiara panoramica del processo di espansione e delle equazioni adottate. Si può inoltre notare dallo schema concettuale che la convergenza del modello per un'assegnata espansione prevede anche un bilancio energetico alla parete che deve essere risolto per determinare la temperatura dell'involucro metallico che è assunta uniforme. In questo bilancio rientrano 4 flussi di potenza: i due flussi di potenza termica provenienti dal raffreddamento del fluido in ingresso e dallo scambio di calore col fluido in uscita, dalle dispersioni termiche verso l'ambiente, sempre uscenti dal

volume di controllo, e dalla potenza meccanica dissipata in calore risultante dall'attrito delle spirali che strisciano l'una contro l'altra. Proprio questi due ultimi flussi di potenza presentano una nuova modellazione rispetto ai modelli semplificati presenti nei lavori di letteratura [16]. Per quanto riguarda le dispersioni termiche è stato implementato un modello in base a quanto proposto da Mc Adams per la convezione naturale su cilindri orizzontali che prevede la dipendenza del numero di Nusselt dal paramentro più significativo per la convezione naturale che è il numero di Rayleigh:

$$Nu = C_{wall} \cdot (Ra)^{1/4}$$

Il calore disperso in ambiente sarà:

$$\mathring{Q}_{amb} = \frac{C_{wall} \cdot (Ra)^{1/4} \cdot \lambda}{L} \cdot A_{ext} \cdot (T_{wall} - T_{amb})$$

dove C_{wall} è un parametro da determinare (in fase di calibrazione del modello), L e A_{ext} sono rispettivamente il diamtero $[m]$ e l'area esterna $[m^2]$ dell'involucro e λ è la conduttività termica dell'aria $[W \cdot m^{-1} \cdot K^{-1}]$. L'altro flusso termico che presenta una modellazione innovativa e di cui non vi è traccia nella letteratura scientifica è la perdita di potenza meccanica utile per attrito tra le spirali striscianti che viene degradata a calore, successivamente entrante nel bilancio energetico alla parete. Questa potenza è modellata tenendo conto della dipendenza da tre parametri: il carico della macchina φ, il coefficiente di attrito f_{frict} tra le spirali e la velocità di rotazione N:

$$\mathring{P}_{loss} = \mathring{P}_{loss}(\varphi, f_{frict}, N)$$

Al fine di tenere conto del carico all'albero è stata effettuata una analogia con i motori a combustione interna per quanto riguarda la pressione media indicata. Allo stesso modo si è ritenuto opportuno ricavare dalla definizione di lavoro per ciclo una pressione media sulle spirali, e quindi nelle camere di espansione, che sarà tanto più elevata quanto maggiore è il rapporto di espansione che la macchina è chiamata ad elaborare. Per quanto riguarda il coefficiente di attrito si è assunto un regime di moto in accordo alla curva di Stribek. Pertanto, le perdite meccaniche da sottrarre al bilancio della potenza lorda saranno:

$$\mathring{P}_{loss} = p_{me} \cdot (a + b \cdot \omega^n) \cdot \omega = p_{me} \cdot (a \cdot \omega + b \cdot \omega^{n+1})$$

Per meglio comprendere come viene risolto l'algoritmo che determina la soluzione del modello di espansione, si può notare dalla Tabella contenente le equazioni che la pressione risultante a valle della laminizione iniziale $p_{su,1}$ è coinvolta nel calcolo della portata massica di refrigerante elaborata dall'espansore e non è nota a priori. Quindi il problema è iterativo in $p_{su,1}$ ed un valore di primo tentativo deve essere fornito. Allo stesso modo, anche la temperatura T_{wall} non è nota. Essa dipende da molti fattori e agisce come variabile di chiusura per i bilanci energetici sul volume di controllo (le incognite dell'algoritmo sono segnate in verde nella tabella). A questo punto altre due equazioni indipendenti devono essere scritte per ricavare queste due incognite. La prima è l'equazione di continuità all'ingresso delle camere di espansione, in cui avviene l'espansione. Qui la portata totale si divide in due percorsi come illustrato nello schema concettuale. La portata massica efficace inizia l'espansione per la quale si estrarrà potenza utile all'albero. Questa è proporzionale alla velocità dell'albero N, alla densità in ingresso $\rho_{su,2}$ e alla cilindrata dell'espansore $V_{exp,sw}$. L'altra portata massica è quella che trafila e non è utile per la produzione di lavoro.
La seconda equazione si riferisce al bilancio energetico alla parete. In questo modello la temperatura della parete deve essere uniforme e i quattro flussi prima menzionati sono responsabili per il mantenimento delle condizioni stazionarie. Il sistema seguente è quindi fondamentale per la convergenza dell'algoritmo:

$$\begin{cases} \mathring{m} = \rho_{su,2} \cdot V_{exp,sw} \cdot N + \mathring{m}_{leak} = \mathring{m}_{in} + \mathring{m}_{leak} \\ \\ \mathring{Q}_{su} + \mathring{P}_{loss} - \mathring{Q}_{ex} - \mathring{Q}_{amb} = 0 \end{cases}$$

Una volta allestito ed implementato il modello in ambiente Matlab si è proceduto alla calibrazione di quest'ultimo sui punti sperimentali forniti dalla campagna sperimentale di Zheng et al. [25]. La calibrazione è stata ottenuta mediante la minimizzazione delle discrepanze tra il dato sperimentale e la predizione del modello, calcolate come media pesata di portata massica, potenza all'albero e temperatura all'uscita.
La procedura di calibrazione porta all'ottenimento di un vettore di 10 parametri (evidenziati in blu nella Tabella delle equazioni e nel sistema a 2 equazioni). Questo vettore è ottenuto mediante l'implementazione di una funzione in Matlab denominata *"Optim_scroll"* nella quale è stata utilizzata la funzione proveniente dal Toolbox di Matlab "*fmincon*" che risolve un sistema di equazioni non lineari e restituisce i parametri che minimizzano lo scarto

con i parametri di confronto. I parametri così ottenuti sono riportati nella Tabella riassuntiva.

A_{su} $[mm^2]$	$AU_{su,nom}$ $[W/K]$	$AU_{ex,nom}$ $[W/K]$	C_{wall} $[W/K^{5/4}]$	$V_{exp,sw}$ $[cm^3/rev]$
97.4	50	110	2.2	94.1

BVR [-]	A_{leak} $[mm^2]$	a $[N \cdot m]$	b $[N \cdot m/s^{1.83}]$	n [-]
2.83	8.5	$3.4 \cdot 10^{-3}$	$1 \cdot 10^{-3}$	1.83

Una volta fissati i parametri del modello con il processo di calibrazione, è stata condotta la validazione sui rimanenti dati sperimentali. Nelle immagini qui sotto riportate è possibile apprezzare l'accuratezza del modello per i punti sperimentali riservati alla calibrazione e alla validazione.

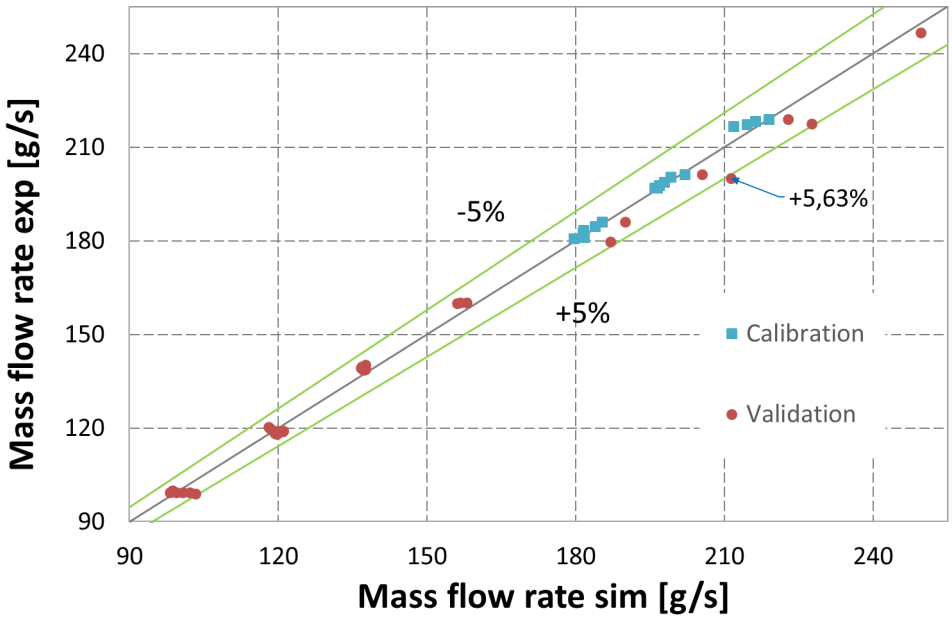

Margini di errore nella previsione della portata massica. E' possibile osservare come i punti sperimentali impiegati per la calibrazione (quadratini blu) abbiano un errore nella previsione del ±2%, mentre quelli su cui è ottenuta la validazione (puntini rossi) rientrano in un margine del ±5%.

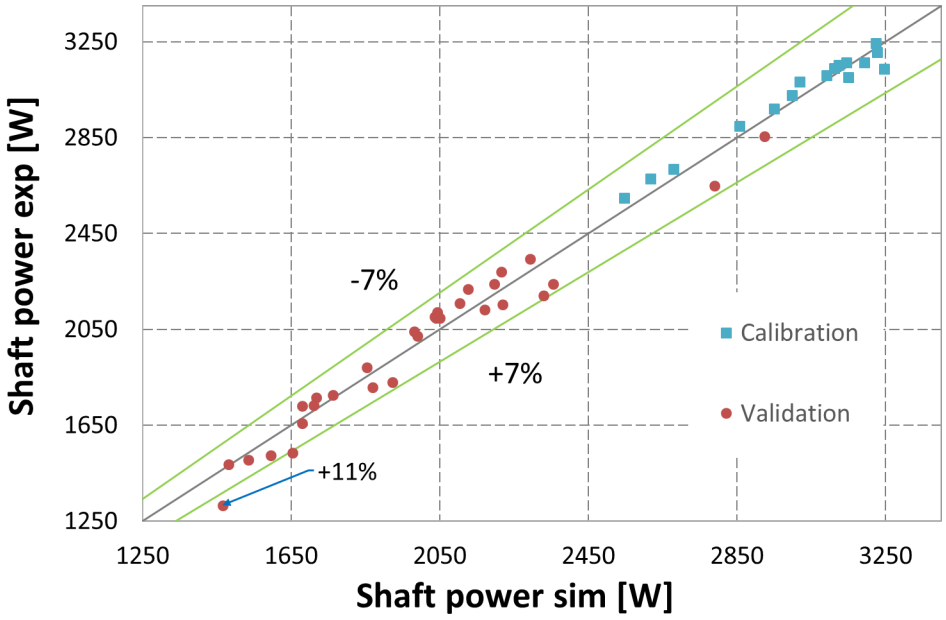

Margini di errore nella previsione della potenza all'albero. E' possibile osservare come i punti sperimentali impiegati per la calibrazione (quadratini blu) abbiano un errore nella previsione del ±3.5%, mentre quelli su cui è ottenuta la validazione (puntini rossi) rientrano in un margine del ±7%.

Inoltre è stata anche sviluppata un analisi di sensitività rispetto ai parametri che più influenzano la risposta del modello e questi sono la cilindrata $V_{exp,sw}$, il BVR e il parametro di potenza n. Una volta confermati i parametri del modello, è possibile sganciarsi dall'analisi sperimentale e indagare più velocemente le potenziali prestazioni dell'espansore scroll in questione, al variare dei parametri sensibili. I parametri studiati sono il rapporto di espansione, il numero di giri della macchina e la temperatura di surriscaldamento.
Il rapporto di espansione determina sempre un aumento di potenza meccanica, al pari di altre condizioni, in quanto l'area sottesa nel diagramma $p - V$ aumenta sempre al diminuire della pressione di condensazione, anche se la potenza viene estratta dall'espansione isovolumica, meno efficiente dell'isoentropica. Proprio per questo motivo, il rendimento isoentropico di espansione si ricuce allontanandosi dalle condizioni di adattamento, e la penalizzazione del rendimento è più pesante nelle condizioni di sovra-espansione rispetto a quelle di sotto-espansione.
Dalla teoria delle macchine volumetriche, si ricava che almeno nel caso ideale il rapporto di espansione dovrebbe essere pari a $\beta = BVR^{\gamma}$ per ottenere estrazione di lavoro con la massima efficienza. Inoltre è molto importante

ai fini della regolazione della macchina variare il rapporto di espansione mediante un adeguamento della pressione di condensazione piuttosto che quella di evaporazione, quando possibile, perchè il rendimeno isoentropico è fortemente penalizzato dall'abbassamento di pressione massima, causato da una laminazione all'ingresso dell'espansore. Inoltre la diversa modalità di regolazione del rapporto di espansione condiziona anche la portata massica di refrigerante elaborata dalla macchina, che diminusce al diminuire di questo. Infatti a parità del numero di giri, un abbassamento di pressione all'ingresso causa una riduzione della densità del fluido che a pari portata volumetrica, causa una riduzione dei g/s entranti nella camera di aspirazione.
Per quanto riguarda la velocità di rotazione si può dire che la potenza presenta sempre un massimo nel range dagli 800 ai 2300 rpm. Questo è dato dal fatto che le perdite di potenza per attrito sono preponderanti rispetto all'aumento di portata conseguentemente ad un aumento della velocità di rotazione, e quindi la potenza massima si ottiene da un trade-off tra queste due grandezze.
E' interessante notare che il salto entalpico alla macchina si riduce all'aumentare della velocità di rotazione. Questo risultato è spiegato dal fatto che il bilancio alla parete scarica la potenza meccanica dissipata in maniera consistente nel riscaldamento isobaro del fluido in coda alla macchina, che quindi aumenta il carico termico da smaltire nel successivo condensatore.
Per quanto riguarda il grado di surriscaldamento assunto dal fluido, è risultato dal modello che deve essere il più limitato possibile. Infatti aumenta il salto entalpico disponibile ai capi dell'espansore, ma in maniera opposta espande il fluido all'ingresso della camera di aspirazione, determinando una riduzione di portata massica elaborata. Il risultato è che questi due effetti si controbilanciano quasi perfettamente, e non si nota un aumento della potenza meccanica.
D'altro canto aumentando la temperatura del fluido in ingresso si aumenta la potenza termica trasferita alla parete metallica che aumenta la sua temperatura, aumentando di conseguenza le dissipazioni termiche verso l'esterno. Queste dissipazioni sono la causa della perplessità mostrata dai Zheng et al. [25], non giustificate. Questa tesi dimostra che è proprio la dissipazione di potenza termica verso l'ambiente a determinare lo scostamento verso il basso della potenza calcolata come $\mathring{m} \cdot \triangle h$ rispetto alla potenza misurata all'albero. Di conseguenza, ne è affetto pure il calcolo del rendimento isoentropico. Ecco allora che questi espansori non possono essere considerati adiabatici, in quanto la dispersione di calore è sempre paragonabile in ordini di grandezza alla potenza estratta all'albero. Tali dispersioni aumentano in maniera consistente con l'aumentare del surriscaldamento del fluido, causando un peggioramento nel rendimento dell'intero ciclo termodinamico.

Per valutare la possibilità di recuperare questa potenza dissipata, si è azzerato il coefficiente convettivo verso l'aria esterna, come se all'espansore venisse applicato un isolamento ideale. Il risultato del modello è stato simile al comportamento che si ha per il surriscaldamento e l'aumento delle dissipazioni per attrito. Infatti quando il flusso termico uscente verso l'ambiente viene a mancare, nel caso di espansore isolato, il bilancio energetico è obbligato a spalmare tale potenza sugli altri flussi ancora presenti. Si vede allora che parte della potenza viene scaricata sul raffreddamento iniziale, facendo espandere il fluido, e la maggior parte di calore viene scaricata al flusso in uscita aumentandone la temperatura, senza osservare una significativa modifica nel valore di potenza raccolta all'albero.
Dato il ΔT guadagnato in uscita, uno sforzo per isolare la macchina ha senso se l'impianto ORC ha scopi cogenerativi, altrimenti questa potenza aggiuntiva è tutta a carico del condensatore che deve essere sovradimensionato.
Alla luce di questi risultati si propongono delle mappe di funzionamneto 2D e 3D che consentono di avere una panoramica chiara del range di funzionamento dell'espansore come rappresentato nell'ultima figura del riassunto esteso, dove sono mostrate le curve di iso-potenza e iso-rendimento, utili al progettista per conoscere le prestazioni della macchina, una volta noti i parametri principali del ciclo termodinamico, ovvero il rapporto di espansione e il numero di giri del generatore elettrico.
La temperatura del fluido in ingresso deve essere la più vicina possibile a quella di saturazione alla pressione di evaporazione per non cadere nella campana bifase. Il fatto che si voglia evitare di entrare nella regione bifase è giustificato dal fatto che la campagna sperimentale si arresta laddove si presentano evidenti segni di presenza di liquido, non fornendo così punti di funzionamento utili per una calibrazione più estesa.
Alla luce di rendimenti modesti e inferiori a quelli delle turbomacchine è stata condotta un'analisi exergetica per indagare in quali trasformazioni si nascondessero le irreversibilità maggiori. E' stata quindi analizzata una curva di isopotenza della mappa di funzionamento per analizzare le fonti di irreversibilità prendendo le coppie di N e β agli estremi della curva e una coppia nel mezzo, dove il rendimento di espansione è un pò più elevato (è evidente che per fornire la stessa potenza a basse velocità di rotazione è necessario un maggiore rapporto di espansione e viceversa).
Da questa analisi è emerso che le 3 principali cause di dissipazioni exergetiche sono i trafilamenti di portata, l'attrito di strisciamento e la cattiva scelta del rapporto di espansione volumetrico (BVR) della machina. La prima è dannosa in quanto, oltre a privare la camera a volume variabile di portata utile, il flusso che trafila arriva a monte del miscelamento adiabatico con una pressione circa pari alla metà della pressione in ingresso, mentre incontra

la portata principale che si trova alla pressione di condensazione, molto distante dalla propria, causando elevati fenomeni di irreversilità, specialmente all'aumentare del rapporto di espansione.

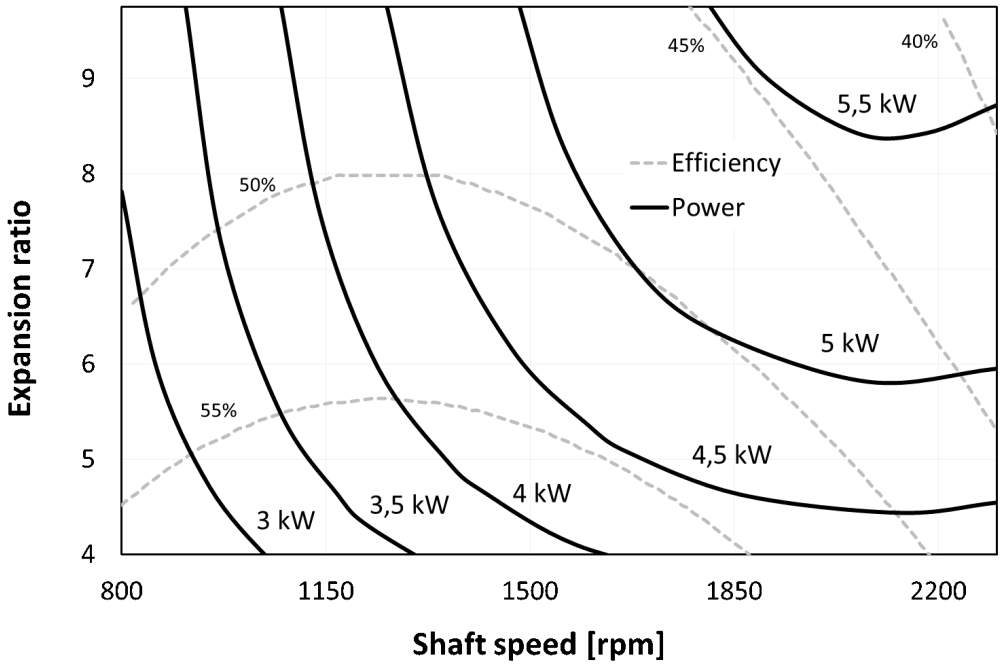

Mappa di funzionamento dell'espansore scroll al variare del rapporto di espansione e velocità di rotazione. La pressione di ingresso è pari a 15 bar e la temperatura in ingresso è fissata e pari 8 K maggiore della temperatura di condensazione corrispondente alla pressione di ingresso

L'attrito è importante per velocità di rotazione elevate, in quanto energia meccanica utile che viene degradata in calore, causando una dissipazione netta di exergia disponibile.
L'ultimo fattore è fondamentale per il funzionamento della macchina in quanto il rapporto di espansione nominale del ciclo deve cadere sempre in un intorno del rapporto di espansione adattato che è funzione del BVR, pena la cessione di una buona parte dell'espansione alla trasformazione a volume costante, meno efficiente della isoentropica.
Le irreversibilità legate agli scambi termici sia interni che esterni sono relativamente meno incisive nel bilancio exergetico, in quanto le temperature interessate dallo scambio termico sono sempre vicine tra loro, mentre la temperatura della parete metallica non è assolutamente lontana da quella ambiente. Infine l'irreversibilità derivante dalla laminazione in ingresso è quasi

sempre trascurabile a meno dei casi con portate massiche più importanti dove l'exergia dissipata raggiunge qualche percentuale sul totale.

Contents

List of Figures

List of Tables

Introduction

Over the past few decades, great amounts of conventional energy resources have been consumed, especially the fossil fuels which account for a larger portion of the global energy consumption. It is worth mentioning that a huge amount of thermal energy is rejected into the surrounding environment in the form of waste heat produced in industrial processes, rejected from internal combustion engines (ICE) through exhaust gases and cooling systems, waste heat from gas turbine exhaust, etc. Many strategies and technologies have been adopted to reduce the fossil fuel consumption and handle the environmental issues.

Currently, Organic Rankine Cycle (ORC) technology is widely applied in low grade heat recovery because of the low boiling point of its working fluid, non-complexity and easy maintenance. ORC is not a new technology, however in recent years it is extensively exploited in small-scale energy systems. Many researchers have specifically paid great attention to waste heat recovery from internal combustion engines using ORC.

As an external combustion engine, the ORC system is particularly suitable for such applications, allowing for the conversion of a very large range of heat sources into mechanical or electrical power. The heat source can be of various origins: solar radiation, geothermal, biomass combustion, ground heat source or waste heat from factories. Besides ORC systems are one of the most promising energy conversion technologies for remote areas for about 2 billion people worldwide who do not have access to electricity and most of them live in sub-Saharan Africa and South Asia where there is plenty of solar energy as only possibility to obtain it. An ORC system works like a conventional Rankine cycle but, instead of water, it uses an organic compound as working fluid. The use of this organic compound allows lower temperatures at the cycle without multistage expanders, providing good efficiency levels in less complex expanders.

As a core component of the ORC system, the expander has a vital role in the overall system performance. To date, two main types of expanders are applied in ORC which can be classified into two types: the first one is the velocity type, such as axial and radial-flow turbines; the other is positive dis-

placement type, such as scroll expanders, screw expanders, piston expanders and rotary vane expanders. Turbine expanders are usually applied in relatively large-scale systems with the output power above 50 kW. However, turbine expanders are not suitable for small scale units, mainly because their rotational speed increases exponentially with the decrease in turbine output power. Furthermore, a small-scale turbine expander is expensive and not commercially viable.
Over the past few decades, scroll machines have been widely used in the fields of air conditioning and refrigeration. The scroll machine working principle is based on the interaction of two nested spirals, often called scrolls, which move relatively and form some variable volume chambers, filled by the working fluid.
With the development of manufacturing technologies and continuous innovation and improvements, the scroll machine technology has also become more and more mature in the residential and commercial markets. Currently, the majority of scroll expanders integrated into the low grade energy utilization systems are almost modified from scroll compressors and the main advantages are the small number of moving parts and the reduced noise and vibrations. Meanwhile, some commercial and in-house designed scroll expanders are also manufactured. However, great performance differences exist between practical applications and theoretical researches because of several major loss factors such as under- and over-expansion, friction losses, internal leakage, supply pressure drop and heat transfer.
This work proposes a tool that simulates the behavior and performance of a scroll expander once the main ORC parameters are defined as the evaporation and condensation pressures, the ΔT of superheating, the working fluid and the shaft speed of the machine. The work starts from the experimental campaign carried out by Zheng et al. [25], which provides several experimental data in terms of thermodynamics points in a wide range of mass flow rates and expansion ratios for a bus air conditioning system scroll compressor modified to work as ORC expander with R123.
The idea was to retrieve and improve a basic model of scroll expander in literature [16] in which there are some inaccuracies from the thermodynamic point of view and make it absolutely solid, to give the micro-ORC designers a reliable tool. Among the model outputs there are the mass flow rate, the outlet temperature, the shaft power, the heat lost to the surroundings and the expansion efficiency. In order to achieve this purpose, the present thesis was organized in a number of chapters:
The first chapter reports a bibliographic review of previous works on the use of scroll machines as expanders to obtain mechanical power. It turns out that only a few manufacturers begin to design the first-use scroll expanders

while all the other studies are performed on compressors derived from air-conditioning system or air compressors, and modified in order to employ them as expanders in micro-ORC systems.
In Chapter 2 the Zheng et al. [25] experimental campaign performed on an ORC-plant is presented, with particular attention to the scroll machine employed as cycle expander derived from a modified 4 kW bus air-conditioning system scroll compressor. This expander shows a remarkable volume displacement if compared to scroll machines presented in the literature review and therefore able to process generous mass flow rates. The expander, is capable of producing 3200 W of peak power while it is possible to reach a declared isentropic efficiency of 83% with low mass flow rate values and expansion ratio close to that corresponding to the adapted condition. In particular the attention is focused on the fact that the researchers do not explain why the performance measured by the AC dynamometer unit is shifted downwards compared to performance calculated as a product of mass flow rate and enthalpy drop from inlet to outlet of the machine.
Chapter 3 presents the model that attempts to describe the expansion process inside the scroll machine. The model provides a first lumped pressure throttling at the inlet by a simple convergent nozzle, a constant pressure heat transfer with the metallic casing considered as isothermal, an isentropic expansion in the expander chambers which are formed between the spirals, an isovolumic expansion to the discharge condition which coincides with the condensation pressure, an adiabatic mixing with the leakage flow from both radial and axial gaps formed by the imperfect contact between metal surfaces and finally a heat transfer with the metal casing which carries the fluid at the outlet machine temperature. This algorithm is then implemented in the Matlab environment with the creation of functions that will be the tool that the ORC-plant designers can rely on for the expander behavior.
In Chapter 4 the model is calibrated over experimental points to get a set of 10 parameters that characterize this specific scroll expander. As mentioned before the most interesting points for the application in a micro-ORC system are those at highest mass flow rate values, because bring about the highest mechanical shaft power and so the calibration is conducted on them. In detail, the deviation of the model prediction is less than $\pm$ 2% for the mass flow rate, $\pm$ 3.5% for the shaft power and ± 2 K for the outlet temperature.
In Chapter 5 the validation on the remaining points is conducted and turns out that the deviation of the model prediction is less than 5% for the mass flow rate, 7.5% for the shaft power and ± 2.5 K for the outlet temperature. This is an indication that some disturbance phenomena may exist in operating a generous volume displacement expander with reduced mass flow rates. At the end of this chapter a sensitivity analysis of the most significant pa-

rameters of the prediction model is included.
Chapter 6 presents a numerical investigation of power fluxes and performance characterizing the scroll expander over a wide operation range. These purposes are achieved by setting all parameters except the one, under study, by varying it with continuity and analyzing the sensitivity on the scroll performance accordingly. It is seen that the parameters of greater influence on the behavior are the shaft speed and the expansion ratio, while the superheat temperature must be as limited as possible in order to not increase the temperature of the metal envelope which affects the heat loss to the environment. Useful 2D and 3D operational maps are plotted in analogy to internal combustion engines to provide an immediate tool to effectively assess the performance of the scroll expander once the main design parameters of the ORC are known.
Finally, an exergy analysis was conducted to understand which irreversibility of the processes involved in the expansion model induces the greater net shaft power degradation. It turns out that, at least for the expanders derived from original compressors, the major irreversibility comes from the mechanical power dissipated into heat due to the sliding spirals and the leakage mass flow rate. The latter deprives the expansion chambers of a substantial part of the useful mass flow rate and brings this relatively high pressure flow to mix with the stream at the condensation pressure flowing out of the constant volume expansion, introducing detrimental irreversibility in the whole expansion process. The other power losses as heat transfers and pressure throttling at the intake introduce lower irreversibility when compared to those mentioned above.

Chapter 1

Scroll expander overview

Scroll machines are widely used as compressors in inverse cycles for heating, ventilation and air conditioning (HVAC) applications as well as in air compression system. Their use in the last decades has been increased based on a number of interesting features: limited parts in motion, simplicity, low air-borne noise, relatively low cost compared to other positive-displacement machines. The scroll working principle is presented with reference to Figure 1.1. The principle is based on the interaction of two nested spirals, often called scrolls, which move relatively and form some variable volume chambers, filled by the working fluid. The expander process includes three phases: charging, expansion and discharging. During the expansion process, the working fluid pushes the center of orbiting scroll to go around the center of the fixed scroll, and there is output work delivered through the eccentric shaft.

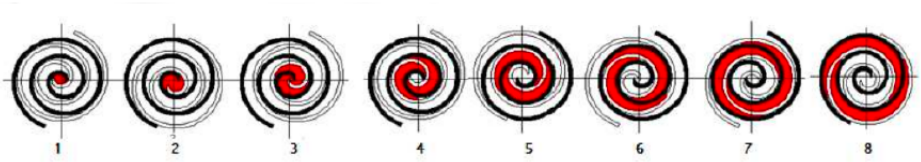

Figure 1.1: Scroll expander working principle

Several types of commercial scroll machines can be modified into expanders which can be integrated into ORC systems for low grade heat recovery. It includes hermetic refrigeration scroll compressor, automotive air-conditioning compressor and open-drive scroll air compressor, as shown in Figure 1.2.
The first pioneer in this field was Yanagisawa et al. [1] in 1988, who performed a scroll expander modified from an automotive air conditioning compressor. The expander adiabatic efficiency reached up to 60 and 75% for the rota-

tional speed in the range of 1000 e 4000 *rpm*. In this paper was carried out that the performances are greatly influenced by the geometrical details of the inner parts of the expander, e.g. during part of the suction process, the expander suction port is blocked by the tip of the orbiting scroll, reducing the effective suction port area, consequently depressing the maximum evolving pressure inside the chambers. Moreover leakages through axial and radial clearances increase the flow rate and decrease the torque heavily. With the development of the low temperature heat recovery technologies, especially for micro- and small-scale systems, numerous research studies have been focused on design and optimization of the scroll expanders applied in ORC systems. The experimental studies have been discussed under different sub-headings according to their types.

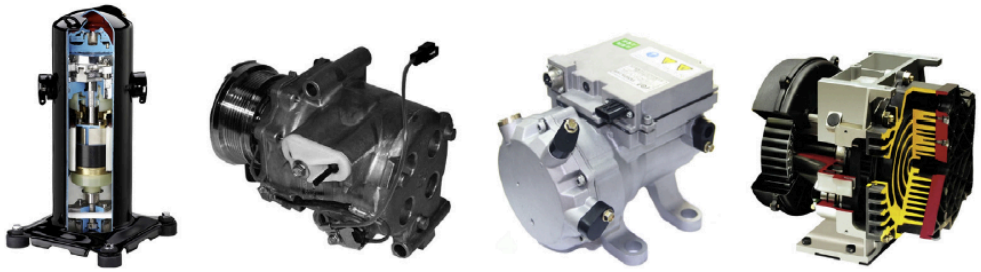

(a) (b) (c) (d)

Figure 1.2: Types of scroll compressors; (a) Hermetic refrigeration compressor. (b) Open-drive automotive air conditioning compressor. (c) Semi-hermetic automotive air conditioning compressor. (d) Air compressor

1.1 Hermetic Scroll expanders

The hermetic compressor components and the motor drive are assembled with a common shaft and welded into a steel container, which cannot be opened for repair. To operate a hermetic scroll compressor in reverse as expander, the compressor casing needs to be cut open to remove check valves that prevent high pressure fluid back flow. To develop an efficient and reliable expansion device, Zanelli and Favrat [2], integrated a scroll expander into a small scale ORC test rig for the performance investigation. The expander was modified from a hermetic scroll compressor with the suction check valve removed and tested with refrigerant R134a. Meanwhile, the internally installed three phase asynchronous motor worked as electric generator. The

main features of the original compressor unit are: a suction volume of 78.41 cm^3/rev, a built-in-volume ratio of 2.44, a nominal electric power of 3.75 kW. It was observed that the maximum isentropic efficiency of the expander reached to 65% at the nominal speed of 3000 rpm. However, the isentropic efficiency was relatively low and unstable at the high rotational speed of 4200 rpm, which is partly due to the poor lubrication.
Kane et al. [3] integrated two redesigned hermetic scroll expanders with different volumetric displacements (53 and 72 cm^3/rev) into a small hybrid solar power system composed of two superposed ORC systems. The topping ORC expander works with R123 while the bottoming with R134. It was found that the expander efficiency decreased at over- and under-expansion conditions. Additionally, the lubrication of the scroll expanders was achieved by circulating a mixture of oil and refrigerant instead of an independent lubricant system. They pointed out that the excess oil mixed with refrigerant leads heat transfer deterioration in the evaporator and decrease the evaporating pressure.
A refrigeration scroll compressor was operated as ORC expander by Mathias et al. [4]. They performed experiments on the original and two structurally modified types of expanders working with R123. One of the modified scroll expanders with appropriate inlet and outlet structures showed relatively enhanced performance characteristics. The maximum output power was 2.96 kW and the maximum isentropic efficiency reached to 83%. Meanwhile, the results also revealed that, to some extent, the expander efficiency was reduced with under-expansion.
In 2012, Lemort et al. [5] conducted an experimental study on the performance characteristics of a hermetic scroll expander modified from a compressor used in heat pump and characterized by a flow rate of 12 m^3/h and a built-in-volume ratio of 3.0. A special vapor cycle was designed to test the performance of the expander working with R245fa. The expander was installed inside a calorimeter to determine the heat transfer to the ambient. A constant air temperature is maintained inside the calorimeter by simultaneously controlling the fan coil water flow rate and the power supply of two light bulbs. Results show that, the ratio between ambient losses and the electrical power produced by the machine ranges from 15 to 40 per cent. Moreover, the electrical power developed by the machine increases monotonically with the system pressure ratio and, even when operate at higher than its internal one (around 3.0), the discharge process still produces useful work for the expander.
In the experiments on an ORC system working with R245fa performed by Bracco et al. [6], in 2013, a scroll expander modified from a hermetic scroll compressor delivered a maximum output power of about 1.5 kW. They cir-

culated a mixture of lubricating oil and working fluid in the ORC system for the lubrication and sealing of the scroll expander, which was similar to the one adopted in Kane's study [3]. The results revealed that, when the expander runs in under-expansion, the isentropic efficiency decreased from 0.75 to 0.6 with the expansion ratio varying from 5.0 to 6.5 and the rotational speed changing in reverse from 4500 to 3000 rpm.

1.2 Semi-hermetic scroll expanders

With the rapid development of the electric and hybrid vehicles in recent years, a small and lightweight semi-hermetic automotive scroll compressor earn the interest of ORC researchers. Compared with hermetic refrigeration scroll compressor, this type of scroll compressor has relatively compact structure and can be easily modified into expander by merely removing the reed valve. In 2011, Hoque [7] selected a semi-hermetic automotive scroll compressor characterized by a flow rate of 6.21 m^3/h and a nominal motor power of 1.5 kW from five scroll compressors and operated it as expander for an ORC system working with R134a. A three-phase permanent magnet motor was operated as a generator in reverse. The results revealed that the maximum isentropic efficiency of the expander reached up to 80%.
Liu et al. [8] designed an in-house scroll expander and tested its performance on a small scale ORC test rig. It is worth mentioning that two couples of scroll wraps were assembled symmetrically with the generator in a shell to broaden the power range. The isentropic efficiency increased initially and then decreased for the rotational speeds in the range of 1200 e 2100 rpm. The efficiency and power output of the scroll expander and the overall system had similar varying tendency. The maximum isentropic efficiency of the expander was only 36.4% for the rotational speed of 1540 rpm, which was mainly due to the machining and assembly errors. The expander volumetric efficiency, in the range of 40 and 63%, increased linearly with the increase of rotational speed.
In 2014, Jradi et al. [9] employed a compact semi-hermetic scroll compressor, which was used in hybrid vehicle air conditioning system, as expander for the experimental investigation of a micro solar and biomass ORC-based combined heat power (CHP) system. The built-in brushless permanent magnetic motor of the expander worked as generator and HFE700 was selected as the system working fluid. It is worth emphasizing that a sight glass is introduced in the superheater-expander line to monitor the quality of the working fluid introduced to the expander. For a system pressure ratio of 4.6 and the heat source of 9.6 kW, the expander delivered an output power of 0.5 kW with

an isentropic efficiency of 75%. It is also shown that the ORC efficiency, electrical efficiency and thermal efficiency are inversely proportional to the increase in the expander inlet temperature.

1.3 Open-drive automotive air conditioning scroll units

Open-drive scroll compressors have been widely applied in the field of automotive air-conditioning systems. Without the electric motor assembled inside the casing, the compressor is driven by automotive engine shaft through the external belt pulley. This type of scroll compressor generally consists of the compressor itself and an external clutch. The clutch engages and disengages the power transmission. When the scroll compressor turns in reverse as expander, this belt pulley and clutch assembly acts as a convenient connection control between the expander and electric generator, especially for the expander experimental investigations. The expander speed can be controlled by changing the diameter of the electric generator belt pulley. However, due to the friction loss of the belt pulley in the power generation process, the whole generating device has a low efficiency. In order to avoid loss of the belt transmission efficiency, the direct shaft connection was adopted in some studies.

In 2007, Saitoh et al. [10] conducted experimental investigations on a small scale solar organic Rankine cycle system. An automotive scroll compressor was employed as expander, and its output performance was determined. In laboratory test, the maximum output power of the expander reached to 0.45 kW at the rotational speed of 1800 rpm. In the same year, Manolakos et al. [11] performed an experimental evaluation on the performance of a solar ORC system for reverse osmosis (RO) desalination. The expander, which drove the high-pressure pump of the RO system, was also modified from an automotive scroll compressor. In the laboratory tests, the expander was connected with an electric brake instead of the pump of RO system. It was found that the expander efficiency remains stable around 60% for the rotational speed varying from 1000 to 3000 rpm with a constant inlet/outlet pressure difference of 1.3 MPa.

Due to low volumetric and isentropic efficiencies of the open-drive scroll expander tested in previous study, Wang et al. [15] modified a hermetic compliant scroll compressor as expander and tested its performance in a simplified R134a vapor power cycle. The inlet displacement for the current scroll expander was estimated to be 6.8 cm^3 per revolution and the inherent (and fixed) expansion ratio was 2.5. The approach used in this study was to

dissolve a compatible oil into the circulating working fluid to lubricate the wraps, while a pump was employed to deliver pressurized oil to the bearings. Two different sealing and lubrication methods were adopted for scroll wraps and bearings, respectively. In a certain range of sealing oil pressures, the isentropic efficiency increased gradually and reached to 77% at 712 kPa. Due to the scroll wraps contact through a thin layer of oil during operation, only a qualitatively small amount of lubricant oil was needed to run the scroll expander efficiently, and a consistent 95 % or higher volumetric efficiency was measured during this early screening test.
Wooland et al. [13] operated an automotive scroll compressor as expander and restricted the radial compliance function to reduce the leakage at low speeds. It is shown that peak of adiabatic efficiency occurs near a filling factor (equivalent of the volumetric efficiency in compressor mode) of unity and an expansion ratio near the built-in-volume ratio of the expander. The results also indicated that under and over-expansion reduces the expander efficiency, which is consistent with the conclusions of some previous researches, and the drop-off in expander efficiency is less severe for values above the built-in volume ratio. This suggests that over-expansion (resulting in recompression of the working fluid at the expander discharge port) is more detrimental than under-expansion. The authors noticed that, the filling factor is almost exclusively a function of the rotational speed of the expander, and higher expansion ratio corresponds to higher pressure difference and consequently, more leakage.
In order to determine parameters of the scroll expander semi-empirical model used for dynamic performance investigation of a small scale solar ORC system, Twomey [14] conducted the laboratory ORC experiments by employing an automotive scroll compressor as expander. The maximum efficiency of the expander was 59% and the maximum output power in experiments reached to 0.55 kW for the rotational speed varying from 479 to 1256 rpm.

1.4 Open-drive scroll air units

Another kind of open-drive scroll compressor is the oil-free or lubricated scroll air compressor. In some previous investigations, scroll air compressors were also modified as expanders for ORC applications. Peterson et al. [15] investigated the performance of a kinematically constrained scroll expander integrated into a small scale regenerative ORC system with a displacement of 12 cm^3/rev and a the built-in volume ratio of 4.57. The expander was modified from a scroll air compressor. An independent oil circulation was adopted for the expander lubrication and seals. Two different viscosity re-

frigerant oils (ISO 48 and ISO 460) were used in the experiments. Analysis of the test results revealed that the expander working with higher viscosity oil has a slight improvement in volumetric efficiency and isentropic efficiency. However, due to serious internal leakage, the maximum isentropic efficiency of the expander under the test conditions was only 49.9%, which was less than the designed value of 75%.
In the experimental investigation conducted by Lemort et al. [16], the performance characteristics of an open-drive and oil free scroll expander fed with R123 were determined. The maximum output power of the scroll expander was 1.8 kW and the maximum isentropic efficiency reached to 68%. The results indicated that over-expansion has a great effect on the isentropic efficiency of the expander at 2296 rpm. Due to the larger internal leakage and smaller supply pressure drop, the filling factor of 1771 rpm is higher than other two rotational speeds. It turned out that filling factor increase with the supply pressure due to the internal leakage flows, but this trend is balanced by the simultaneous effect of the supply pressure drop. It has been observed that the lower the rotational speed, the higher the filling factor, due to the larger relative impact of the internal leakage and due to smaller supply pressure drop. The experimental results also validated the semi-empirical scroll expander model developed by Lemort et al. [16], which has a good accuracy on the prediction of the mass flow rate, shaft power and exhaust temperature of the expander.
Due to the safety level and environmental impact of many organic working fluids, a series of sealing measures should be implemented to the expanders applied in ORC systems. Declaye et al. [17] converted a commercial oil-free scroll air compressor into expander with dismantling the external cooling fan and assembling the expander inside a hermetic cylindrical steel casing. He chose an air scroll compressor for three reasons: The absence of oil simplifies the system design and avoids the negative impact of circulating oil on the performance; The higher built-in-volume ratio allows the machine to work under higher pressure ratio without a significant reduction in efficiency, and the conversion of the compressor into an expander is very simple. From the results it can be noted that despite a fixed built-in-volume ratio, the value of the pressure ratio that maximizes the isentropic efficiency is not constant for all rotational speeds. It ranges from 3.42 at 2000 rpm to 4.33 at 3500 rpm. This shift of the maximum position is due to other additional influences such as leakages, friction losses, pressure drop in the inlet port and heat exchanges. The value of the maximum isentropic efficiency also depends on the rotational speed. For an inlet pressure of 12 bar, it ranges from 71.3% at 3500 rpm to 75.7% at 2500 rpm. This maximum confirms the numerical result obtained by Lemort et al. [16]: at low rotating speed and high pressure

ratio, the relative impact of leakages on the performance is predominant. On the contrary, at higher speed, the predominant sources of inefficiency are the mechanical losses and the inlet pressure drop.
Quoilin's et al. [18] employ a kinematically rigid scroll configuration without axial and radial compliance. Shaft power was transferred to the generator through permanent magnet coupling, which avoided the difficulty of shaft seal. The maximum isentropic efficiency and shaft power of the expander fed with R245fa were 75.5% and 2.1 kW, respectively.
Aoun and Clodic [19] investigated the performances of a scroll expander integrated into a micro cogeneration steam Rankine cycle. An oil-free scroll air compressor was adopted as expander working with steam. The polytetrafluorethylene seal for the scroll tip increased the volumetric efficiency by 20%. However, the maximum isentropic efficiency was only 48% due to external leakage flow, pressure losses and heat dissipation.
Zhou et al. [20] carried out an experimental investigation on an ORC system for flue gas waste heat recovery working with R123. A 5 kW oil-lubricated scroll air compressor was operated as expander with an additional lubricating circulation. The scroll expander drove a brushless synchronous generator by means of two belt pulley couplings. The maximum output power of the expander was 0.645 kW for the heat source temperature of 215°C and the working fluid evaporating pressure of 10 e 18 bar, which was lower than the design value due to the over-expansion losses. The results also show that superheat degree of working fluid would bring negative effects on system performance. All the previous works mentioned above are summarized in Table 1.1 and 1.2.

1.5 Development of novel scroll expanders

In recent years, several commercial scroll expanders have been designed and developed with advanced manufacturing techniques, which are based on the mature technology of scroll compressors. However, as mentioned in the Introduction, the development of scroll expanders is still in an early stage. So far, these commercially available scroll expanders are not mass-produced and designed for special and narrow power range. Air Squared, Inc. [21] has developed semi-hermetic scroll expanders with three different power levels (1 kW, 5 kW and 10 kW) for low-grade thermal energy utilization. The scroll expanders have the same volumetric expansion ratio of 3.5 with different displacements. The maximum rotational speed of the expanders is 3600 rpm. Images of these novel machines and technical details are shown in Figure 1.4. The performance tests of 1 kW scroll expander were conducted on the ORC

test rig designed by Woodland et al. [13].
Based on Kane's research, Eneftech Innovation [22] has developed novel hermetic scroll expanders for its products called ENEFCOGEN units which are small combined heat and power systems for producing electricity from industrial waste heat and engine exhaust gases. ENEFCOGEN is developing new generation scroll expanders with rotational speeds of 1500-6000 rpm and maximum power of 5 kW.
Kim et al. [23] developed and manufactured an in-house three-idler crank configuration based scroll expander for 15 kW steam power cycle. The scroll expander is showed in Figure 1.3 and has a double-sided scroll configuration. On account of the balanced axial gas forces acting on the orbiting scroll base plate, there is no need for thrust bearing assembly. The test results revealed that the expander volumetric efficiency was 42.3-52.1% and total expander efficiency was only 34% for the rotational speeds of 1000-1400 rpm.
Two types of open-drive scroll expanders based on two-phase steam were developed for a thermodynamic cycle named Liquid-Injected Cogeneration (LIC) designed by ECR International [24]. The maximum output power of single-shaft configuration based on scroll expander was 1.9 kW when the rotational speed increased to 2800 rpm. Meanwhile, the three-idler crank scroll expander exceeded 2.5 kW in the range of 3000-3600 rpm.

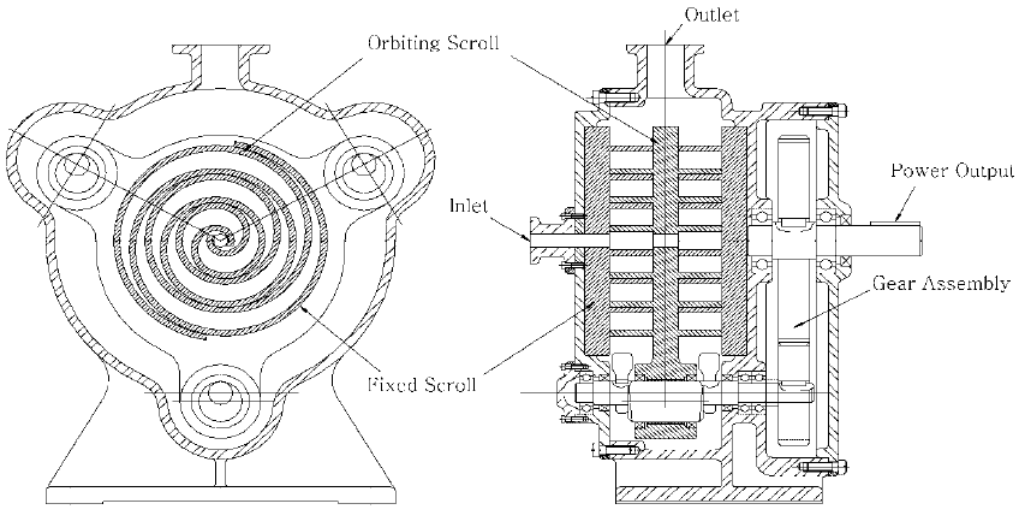

Figure 1.3: Layout of the double-sided scroll expander assembly [23]

Table 1.1: Summary table 1/2

Experiments of ORC systems integrated with hermetic expanders									
Authors	**Fluid**	**Displacement** $[cm^3/rev]$	**BVR**	**Flow rate** $[g/s]$	**Speed** $[rpm]$	**Power** $[kW]$	**Pressure Ratio**	**Temp** $[°C]$	η_{is} %
Zanelli et al. [2] (1994)	R134a	32.13	2.4	-	2400-3600	1-3.5	2.4-4	70	65
Kane et al. [3] (2003)	R134a-R123	53-72	2.3-2.3	-	-	3-10	1.6-4.8	160	68
Mathias et al. [4] (2009)	R123	-	-	-	3670	1-2.96	3.1-8.8	-	83
Lemort et al. [5] (2012)	R245fa	22.4	3.0	121-38	-	0-3	2-5.8	139	71.3
Bracco et al. [6] (2013)	R245fa	-	-	-	3000-4500	1-1.5	5-6.5	150	75
Experiments of ORC systems integrated with semi-hermetic expanders									
Authors	**Fluid**	**Displacement** $[cm^3/rev]$	**BVR**	**Flow rate** $[g/s]$	**Speed** $[rpm]$	**Power** $[kW]$	**Pressure Ratio**	**Temp** $[°C]$	η_{is} %
Hoque et al. [7] (2011)	R134a	-	-	-	2000	1.5	2.5-3	-	80
Liu et al. [8] (2013)	R123	-	-	-	1200-2066	0.4-0.7	4.4-4.8	-	36.4
Jradi et al. [9] (2014)	HFE-7100	-	-	200-47	-	0.5	1.4-4.2	150	80

Table 1.2: Summary table 2/2

Experiments of ORC systems integrated with open-drive expanders modified from automotive A/C scroll compressors									
Authors	**Fluid**	**Displacement** $[cm^3/rev]$	**BVR**	**Flow rate** $[g/s]$	**Speed** $[rpm]$	**Power** $[kW]$	**Pressure Ratio**	**Temp** $[°C]$	η_{is} %
Saitoh et al. [10] (2007)	R113	60	-	160	1500-5000	0.45	-	136	63
Manolakos et al.[11] (2009)	R134a	-	-	350-120	0-4000	0-2	-	-	65
Wang et al. [12] (2009)	R134a	6.8	2.5	29-14	2000-3700	1	2.65-4.8	134	70
Woodland et al. [13] (2012)	R134a	65.09	1.8	-	500-5000	-	1.2-4.3	-	72
Twomey et al. [14] (2012)	R134a	53.1	1.57	70-50	479-1256	0.1-0.5	1.3-1.7	120	59
Experiments of ORC systems integrated with open-drive expanders modified from scroll air compressors									
Authors	**Fluid**	**Displacement** $[cm^3/rev]$	**BVR**	**Flow rate** $[g/s]$	**Speed** $[rpm]$	**Power** $[kW]$	**Pressure Ratio**	**Temp** $[°C]$	η_{is} %
Peterson et al. [15] (2008)	R123	12	4.57	190-160	600-1400	0.2-0.4	3.3-3.9	175	50
Lemort et al. [16] (2009)	R123	36.54	4.05	86-45	1771–2660	0.4-1.8	2.7-5.5	165	68
Declaye et al. [17] (2013)	R245fa	30.88	3.95	150-45	2000-3500	0.3-2.1	2.5-8	-	76
Aoun et al. [19] (2008)	Water,Air	31.5	3.2-5	-	1200-3050	0.2-0.8	2.8-5	180	48
Zhou et al. [20] (2013)	R123	-	-	-	300-1300	0.1-0.6	-	220	-

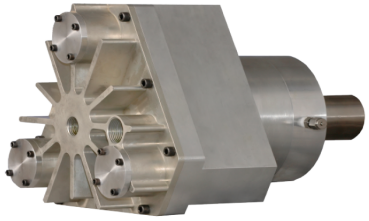

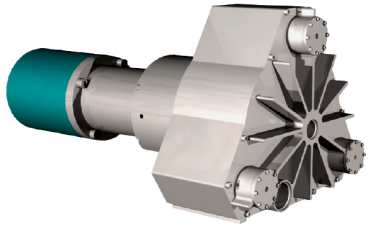

Output	1 kW (nom.)	5 kW (nom.)	10 kW (nom.)
BVR	3.5	3.5	3.5
Efficiency	75%	-	80% (Lubric.) 70% (Oil-free)
Inlet Pressure	13.8 bar	13.8 bar	10 bar
Displacement	12 cm^3/rev	73.6 cm^3/rev	155 cm^3/rev
Max. Speed	3600 rpm	3600 rpm	3600 rpm
Max. Temp.	175 $°C$	-	175 $°C$
Sound Level	55 $dB(A)$	55 $dB(A)$	55 $dB(A)$
Net Weight	9.07 kg	-	-
Working Fluid	R134a- R245fa	R134a- R245fa	R134a- R245fa

Figure 1.4: Catalog of Air Squared novel expanders [21]

Chapter 2

Test rig description and experimental campaign

2.1 The ORC system design and thermodynamics

The test and analysis of the Organic Rankine Cycle (ORC) operated with R123 as working fluid performed by Zheng Miao et al. [25] is presented in this chapter. For the purpose of this thesis, special attention is given to the 4 kW scroll compressor employed in reverse as expander of the ORC plant. The paper focus on steady-state operation characteristics and output performances of the ORC system. Effects of the R123 mass flow rate and expander shaft torque on key operating parameters, such as pressures and temperatures at expander inlet and outlet, rotating speed, shaft power and thermal efficiency, are analyzed. Operation characteristics under heat source temperatures of 140 $°C$ and 160 $°C$ are compared.
Figure 2.1 (a) shows the design chart of the ORC flow loops in this study. This system consists of five coupled subunits: the conductive oil circuit (red lines), R123 circuit (brown lines), cooling water circuit (blue lines), lubricant oil circuit (green lines) and AC dynamometer unit. The conductive oil is used to simulate the low grade heat source and a cooling tower is installed outdoor to cool down the warm water coming back from the condenser. The thermodynamics of the ORC system is the same as that of the traditional steam Rankine cycle. The high pressure liquid R123 from the pump is heated into vapor in the evaporator. The heating power received by R123 is:

$$\mathring{Q} = \mathring{m} \cdot (h_{eva,out} - h_{eva,in}) \tag{2.1}$$

where $\mathring{m}$ is the R123 mass flow rate $[kg/s]$, and $h_{eva,out}$ and $h_{eva,in}$ $[J/kgK]$ are R123 enthalpies at the evaporator outlet and inlet, respectively. These two enthalpies are determined by the pressures and temperatures at the evaporator outlet and inlet, respectively.
Then, the high pressure and high temperature R123 vapor expands in the expander to generate work. Figure 2.1 (b) shows the T-s diagram of the present ORC prototype. Points 1 and 2 can be determined by the tested temperatures and pressures at expander inlet and outlet. In addition the traditionally calculated shaft power of the expander in literature is given as:

$$\mathring{W}_{t,cal} = \mathring{m} \cdot (h_{t,in} - h_{t,out}) \tag{2.2}$$

where $h_{t,in}$ and $h_{t,out}$ are the enthalpies at the expander inlet (point 1) and outlet (point 2).
The expansion process is usually not an isentropic process. Despite in this circumstances the expansion process is not even adiabatic as it is customary to consider it in most cases, at first, commonly expander efficiency can be defined as:

$$\eta_{t,is} = \frac{h_{t,in} - h_{t,out}}{h_{t,in} - h_{t,is,out}} \tag{2.3}$$

where $h_{t,is,out}$ is the outlet enthalpy through the ideal isentropic expansion process (point 2 s), which could be deduced from the expander inlet entropy and expander outlet pressure.
Another more appropriate expander efficiency indicator that takes into account the heat transfer will be introduced in the next chapters.
Process 1r-2r in the T-s diagram (blue line) represents the real expansion process in the expander chamber. It is noted that, the expansion process is much complicate and, due to the limit of the testing technique, it is hard to capture the thermodynamic parameters in the expander chamber. The most common method is to locate temperature and pressure sensors at the inlet and outlet tubes of the expander. And this leads to the above mentioned derivation of the tested expansion process (1-2) from the real one (1r-2r), as the tested temperatures and pressures cannot truly reflect the losses, such as the pressure drop from the tube to the chamber, the over-expansion or under-expansion, the internal leakage and so on. Thus, in the present ORC prototype, the AC dynamometer was adopted to measure the real output power of the expander.
The low pressure R123 vapor exhausted from the expander is then cooled

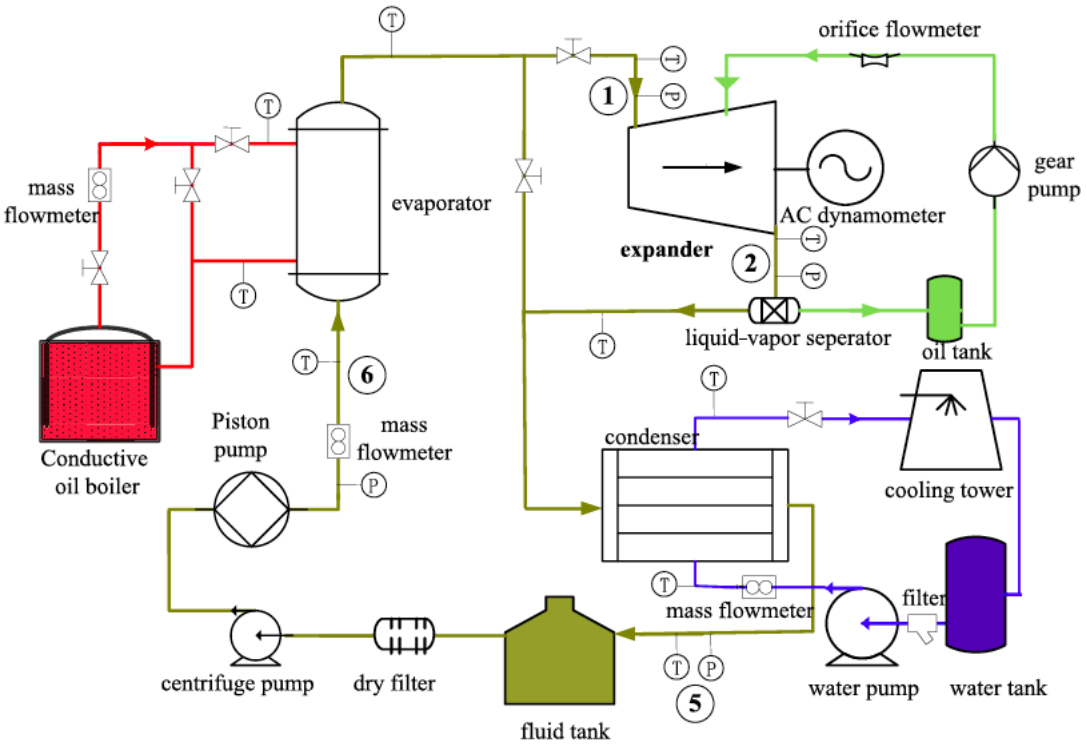

(a)

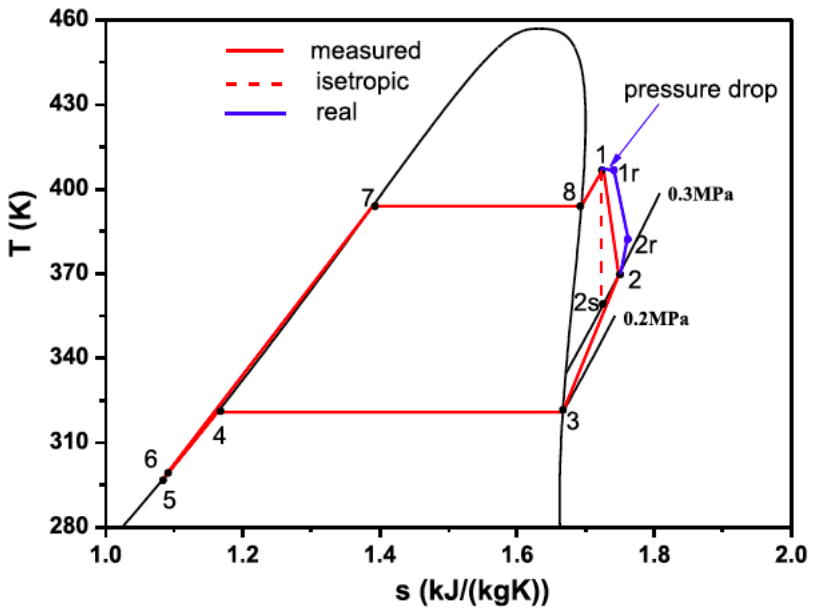

(b)

Figure 2.1: (a) Schematic representation of the test facility and, (b) T-s diagram of the present ORC system. [25]

down into liquid in the condenser, and cycled by the pump. The calculated power consumed by the pump is

$$\mathring{W}_{p,cal} = \mathring{m} \cdot (h_{p,out} - h_{p,in}) \tag{2.4}$$

where $h_{p,out}$ and $h_{p,in}$ are the fluid enthalpies at the pump outlet (point 6) and inlet (point 5), respectively. Thus, the calculated "net" output power and the thermal efficiency of the ORC system are as follows:

$$\mathring{W}_{cal} = \mathring{W}_{t,cal} - \mathring{W}_{p,cal} \tag{2.5}$$

$$\eta_{cal} = \frac{\mathring{W}_{cal}}{\mathring{Q}} = \frac{\mathring{W}_{t,cal} - \mathring{W}_{p,cal}}{\mathring{Q}} \tag{2.6}$$

The subscript 'cal' in Eqs. from (2.2) to (2.6) are saying that the variable is not directly measured but calculated based on the measured pressures and temperatures at various locations. In the work by Zheng et al. [25], the expander output work and the power consumed by the pump is also directly measured and compared with the calculated ones. Details will be introduced in the next section.

2.2 The test rig description and operating procedure

According to the design in Figure 2.1 (a), the ORC prototype was constructed, which is shown in Figure 2.2. The detailed information about this system is given as follows:
The conductive oil is heated by an electric heater with the capacity of 100 kW, which can automatically adjust the power to maintain the required outlet temperature with an uncertainty of 1 $°C$. The maximum oil temperature can reach 250 $°C$.
The cooling water loop is thermally coupled with the R123 circuit through the condenser. The closed spray cooling tower is installed outdoor to dissipate the extra heat of the ORC system to the air. The capacity of the cooling tower is about 73 kW at the water flow rate of 5000 kg/h and the temperature drop of 5 $°C$. The lubricant is needed to ensure the smooth operation of the expander. It is circulated by a gear pump and mixed with the R123 vapor at the expander inlet. After the expansion, it is separated

from the R123 vapor by an efficient vapor-oil separator. A tube-in-tube heat exchanger with the heat transfer area of 5.5 m^2 is used as the evaporator and a plate heat exchanger with 6.1 m^2 as the condenser. The R123 is circulated by the piston pump, which is controlled by a frequency converter. The frequency of 50 Hz corresponds to the volume flow rate of about 2000 l/h. A dry filter is located between the pump and the liquid tank to eliminate the negative effects coursed by the humidity and impurity. A centrifuge pump is installed after the dry filter to prevent the cavitation of the piston pump caused by the low boiling point and heat capacity of R123. This pump is also controlled by a frequency converter.
Figure 2.3 (a) and (b) gives the photos of fixed and rotating scrolls of the scroll expander used in the present ORC system. As already said, due to the lack of kW-scale expander in the market, this expander was modified from a scroll compressor originally used in the bus air conditioning system. Figure 2.3 (c) gives the detailed geometrical parameters of the scroll expander. And the maximum shaft power of the expander is estimated about 4 kW.
In order to identify the difference between the calculated parameters in Eqs. from (2.2) to (2.6) and the tested ones, an AC dynamometer unit was adopted in this work to dynamically measure the rotating speed and shaft torque of the expander. The unit consisted of a frequency converter, an AC motor, a rotating speed sensor, a monitor, a software and transmission facilities. During the test, the shaft torque of the AC motor was set by the software and the frequency converter to be a specific percentage of the maximum value (78.5 Nm herein). Assembly unit details can be seen in Figure 2.2. Based on the measured rotating speed and shaft torque, the output power of the expander is

$$\mathring{W}_{t,me} = N_t \cdot T_t / 9.55 \tag{2.7}$$

where N_t $[rpm]$ and T_t $[N \cdot m]$ represent the rotating speed and the shaft torque of the expander. The power consumed by the R123 pump and the centrifuge pump can be obtained from the frequency converter. In such a way, the measured output power and thermal efficiency are:

$$\mathring{W}_{me} = \mathring{W}_{t,me} - \mathring{W}_{p,me} \tag{2.8}$$

$$\eta_{me} = \frac{\mathring{W}_{me}}{\mathring{Q}} = \frac{\mathring{W}_{t,me} - \mathring{W}_{p,me}}{\mathring{Q}} \tag{2.9}$$

where the subscript "me" stands for the measured value.

In the present ORC system, the measured parameters include the temperature, pressure, mass flow rate of the conductive oil, cooling water and R123 in each corresponding subsystem as well as the rotating speed and shaft torque of the expander. The location of sensors in the ORC system can be found in Figure 2.1 (a). And the detailed information of sensors is given in Table 2.1. As several parameters in the equations mentioned above are calculated based on the measured temperatures and pressures, an error analysis was carried out based on the commonly used expression:

$$\triangle Y = \sqrt{\sum\nolimits_i (\frac{\partial Y}{\partial X_i})^2 \cdot \triangle X_i^2} \tag{2.10}$$

$$e_Y = \frac{\triangle Y}{Y} \tag{2.11}$$

where $\triangle Y$ and e_Y are the uncertainty and relative uncertainty of variable Y, while X_i represents the independent variable in equations. The error analysis of the key cycling parameters is given in Table 2.2. It is noted that the enthalpies of R123 at various state of the cycle were obtained from the software REFPROP of NIST. The state equation of R123 and the calculation process in the software are complicated.
For simplification, the uncertainty of enthalpy, $\triangle h$, is estimated through the expression $\triangle h = \sqrt{\triangle h_T^2 + \triangle h_P^2}$. And, $\triangle h_T$ and $\triangle h_P$ are directly calculated by REFPROP from $\triangle T$ and $\triangle P$.

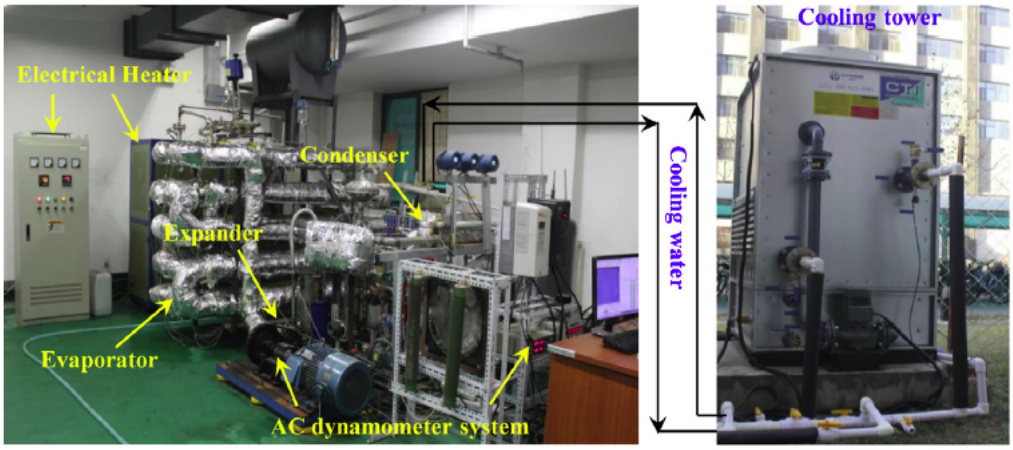

Figure 2.2: The photo of the experimental setup [25]

(a)

(b)

Geometry parameters	
Scroll turns	2.25
Height of the scroll profile	50 mm
Thickness of the scroll profile	4.8 mm
Pitch of the scroll profile	26.5 mm
Radius of the expander	170 mm
Length of the expander	281 mm

(c)

Figure 2.3: The photos of (a) the fixed scroll, (b) the rotating scroll, and (c) the geometrical parameters of the scroll expander. [25]

2.3 The testing procedure

In order to perform the tests, the closed R123 loop was initially vacuumized to remove the non-condensable gas. Then, it was charged by a certain amount of R123. From the thermodynamic point of view, the ORC system could be operated by specifying the R123 mass flow rate, temperatures and pressures. However, these parameters are not independent with each other in the closed loop during the operation. In contrast, from the control point of view, the operation of the ORC system could be specified by two accessible and independent parameters: the R123 mass flow rate and the external load of the expander, such as the shaft torque or the rotating speed. In the present ORC system, both the R123 mass flow rate and the shaft torque (or rotating speed) could be easily adjusted through the frequency converters.
In this work, two cases are carried out based on the temperature of conduc-

tive oil at the evaporator inlet, 140 $°C$ in case 1 and 160 $°C$ in case 2. Table 2.3 shows the main operating parameters. In each case, the conductive oil is controlled at a constant mass flow rate and temperature before entering the ORC evaporator. The mass flow rate of cooling water is also kept constant while the temperature at the condenser inlet varied in a narrow range due to the changed environment temperature and condenser load. Before the test, a pumping frequency of R123 pump was first set according to the temperature of conductive oil.
Then the shaft torque of the expander was increased from 10% of the maximum torque load to the value at which the degree of overheat at expander inlet was too small or the shaft power of the expander exhibited a significant decrease. After that, a bigger pumping frequency was set and repeat the process of adjusting the expander shaft torque. When the pumping frequency reached a certain value under which the degree of overheat was too small even at the low shaft torque, the case was finished.

Table 2.1: Parameter measurements and uncertainties [25]

Parameters	Sensors	Range	Accuracy
Temperature	K-type thermocouple	minus 200 - 1300 $°C$	$\pm$0.5 $°C$
Pressure	Rosemount 3051 CG	0-5 MPa	$\pm$0.1% F.S
Pressure difference	Rosemount 3051 CD	0-100 kPa	“
Mass flow rate	Coriolis mass flowmeter	800-8000 kg/h (Water)	$\pm$0.2% F.R.
		0-3000 kg/h (R123)	-
		300-3000 kg/h (oil)	-
Rotating speed	JN338 rotational sensor	0-6000 rpm	1.0 rpm
Shaft torque	JN338 rotational sensor	0-100 Nm	0.5% F.S

Table 2.2: Error analysis of the key cycling parameters [25]

Parameters	Related variables	Average relative uncertainty
Enthalpy, h	T,p	0.5% (vapor)
		0.3% (liquid)
Heat transfer rate, $\mathring{Q}$	m,h	1%
Calculated shaft powers, $\mathring{W}_{t,cal}$	m,h	2.3%
Calculated power consumed by pump, $\mathring{W}_{p,cal}$	m,h	3.9%
Calculated net power output, $\mathring{W}_{cal}$	$\mathring{W}_{t,cal}$, $\mathring{W}_{p,cal}$	3.3%
Calculated thermal efficiency, η_{cal}	$\mathring{W}_{cal}$, $\mathring{Q}$	3.5%
Measured shaft power, $\mathring{W}_{t,me}$	N_t, T_t	0.5%
Measured thermal efficiency, η_{me}	$\mathring{W}_{t,me}$, $\mathring{Q}$	1.1%

Table 2.3: Major operating parameters in this study [25]

Case 1: tested on Nov. 5. 2014	
Air temperature	10 $°C$
Temperature of the conductive oil	140 $°C$
Mass flow rate of the conductive oil	2000-2029 kg/h
Temperature of the cooling water	15.7-21.3 $°C$
Mass flow rate of the cooling water	2756-2763 kg/h
Shaft torque	10%-70%
R123 pumping frequency	5-8 Hz

Case 2: tested on Nov. 4. 2014	
Air temperature	10 $°C$
Temperature of the conductive oil	160 $°C$
Mass flow rate of the conductive oil	2015-2034 kg/h
Temperature of the cooling water	22.1-24.7 $°C$
Mass flow rate of the cooling water	2769-2780 kg/h
Shaft torque	10%-90%
R123 pumping frequency	10-13 Hz

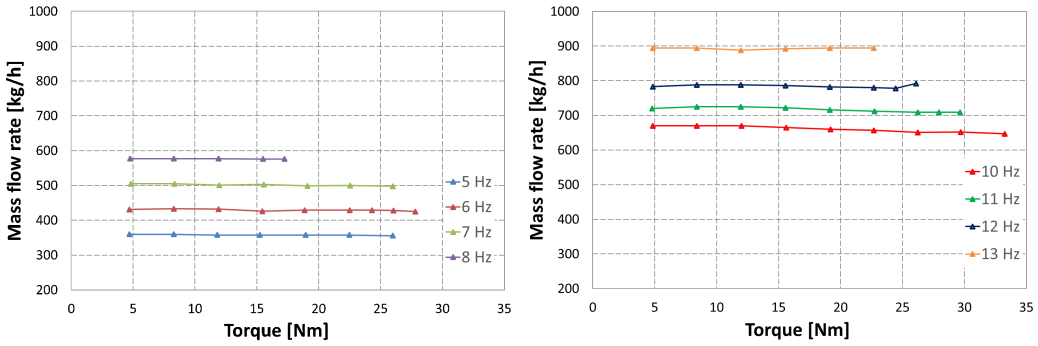

Figure 2.4: Variation of R123 mass flow rates with different shaft torques.

2.4 Effect of the pumping frequency and shaft torque on key operation parameters

Figure 2.4 shows the variation of R123 mass flow rate at different shaft torques of the expander. This variation is imposed by the volumetric pump at different pumping frequency (PF). In Figure 2.4, on the left, the 140 $°C$ conductive oil temperature case is shown, while the case of 160 $°C$ is shown on the right. Such representation will be repeated for all the operating parameters from here on. Due to the characteristic of the piston pump, R123 mass flow rate is quite stable at every pumping frequency. The change of the shaft torque has quite limited effect on it. And an increase in PF by 1 Hz led to the increase in R123 mass flow rate by about 70 kg/h. The stability of R123 mass flow rate is beneficial to the control and smooth operation of the ORC system. At the heat source temperature of 140 $°C$, the proper PF is 5-8 Hz, corresponding to the R123 mass flow rate of about 350-570 kg/h. When the heat source temperature increased to 160 $°C$, more heat could be provided. Thus, the available PF changes to 10-13 Hz, corresponding to the R123 mass flow rate of about 660-900 kg/h. Figure 2.5 shows the vapor pressure at the expander inlet. For every PF, the increase in shaft torque led to the increase in vapor pressure as the stable operation of the expander need a higher vapor pressure in the chamber to balance the increased resistance on the shaft. The increase of vapor pressure also means the decrease in the volume flow rate, so as to the decrease in the expander rotating speed. For every specified shaft torque, the vapor pressure increased with the PF (representing the R123 mass flow rate). As the PFs at the oil temperature of 160 $°C$ are higher than those at 140 $°C$, the inlet vapor pressures were also higher. The largest vapor pressure at oil temperature of 160 $°C$ is about 1.5 MPa while 1.2 MPa at 140 $°C$.

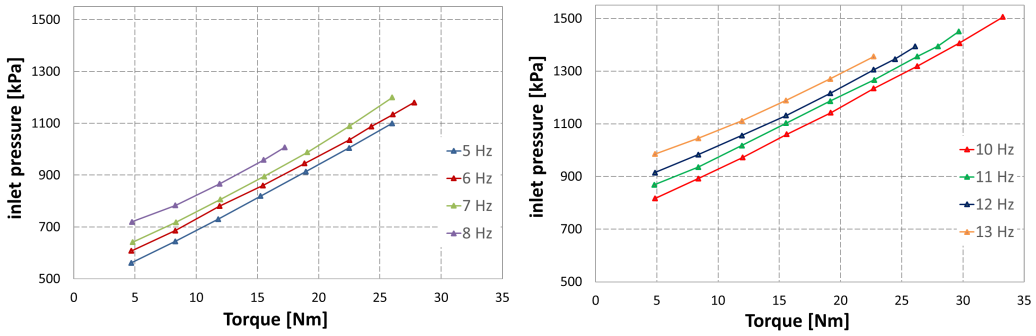

Figure 2.5: Variation of vapor pressure at the expander inlet with different shaft torques.

Figure 2.6 shows the variation of vapor temperature at different shaft torques and mass flow rate for both oil conductive temperatures. This parameter is very sensitive to the shaft torque. However, the profiles exhibit different trend for different PF. At the most PFs (6, 8 Hz and 10-11 Hz), the vapor temperature monotonically decrease with the shaft torque. This phenomenon agrees well with the heat transfer mechanism in the evaporator. The higher vapor pressure at higher shaft torque led to the higher saturated temperature. In the evaporator, it means the enlargement of the preheating area and the shrinkage of the evaporation area. As the two-phase heat transfer coefficient is much larger than the single-phase one, the total heat flux of the evaporator became smaller.
When the R123 temperature at the evaporator inlet is relatively stable, the decrease in heat flux result in the decrease of the vapor temperature at the expander inlet. And this process also make the vapor superheat decrease sharply, seen in Figure 2.7. The trends of temperature profiles at PF of 5, 7, 12 and 13 Hz in Figure 2.6 are different from those at other PFs. At 5 Hz, the R123 mass flow rate is too small, so the area of evaporator is sufficient. Under this condition, the vapor temperature is determined by the temperature difference at the outlet of the evaporator. Thus, at every shaft torque, the variation of the vapor temperature is very limited. At 7, 12 and 13 Hz, the "V" type temperature profiles are seen. Taking temperature profile at 13 Hz as an example, the reason why the vapor temperature decrease with shaft torque from 4.8 to 15.6 Nm is the same as the above mentioned heat transfer mechanism. And at shaft torque of 15.6 Nm, the vapor superheat approached 0, seen in Figure 2.7. Then, with the further increase in shaft torque, R123 at the expander inlet go into the two-phase state, which means the temperature herein is the saturated temperature. Thus, the higher vapor pressure at higher shaft torque led to the continue increase in R123 tempera-

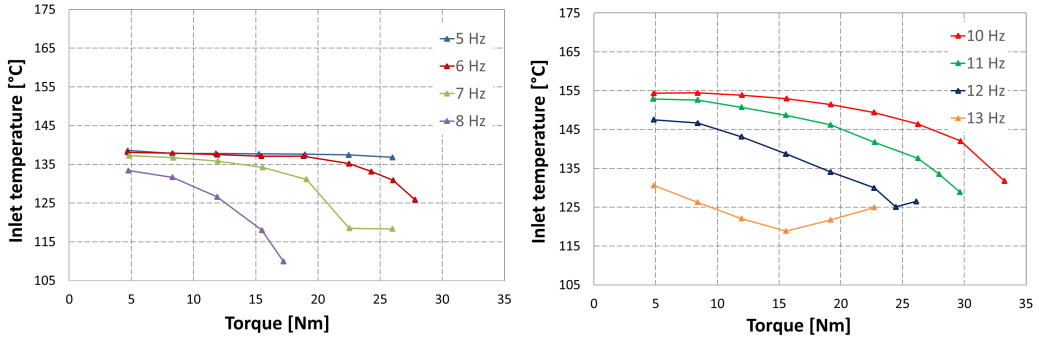

Figure 2.6: Variation of vapor temperatures at the expander inlet with different shaft torques.

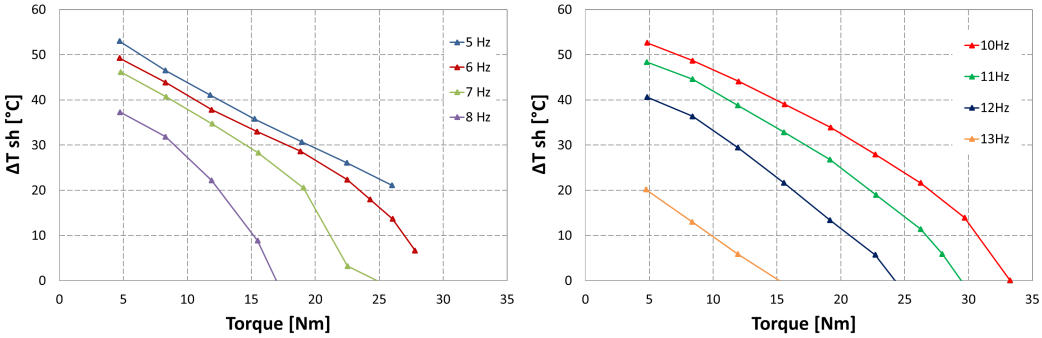

Figure 2.7: Variation of vapor superheats at the expander inlet with different shaft torques.

ture and a "V" type temperature profile appear. Variations of vapor pressure, temperature and degrees of superheat at the expander outlet are shown in Figure 2.8, 2.9 and 2.10. Generally speaking, all the three variables, including vapor pressure, temperature and superheats at expander outlet decrease with the shaft torque. In Figure 2.8, it can be seen that vapor pressure gradually decrease with the shaft torque. And the decent range is quite limited. This is because the lower heat flux in the evaporator at higher shaft torque also reduce the heat transfer load of the condenser. Thus, the vapor pressure in the condenser decrease with the shaft torque. Besides, for a specified shaft torque, it can be observed that the vapor pressure increase with the PF as the higher R123 mass flow rate led to higher heat transfer load of the condenser.

Due to the decrease of vapor temperature at the expander inlet seen in Figure 2.6, it can be seen in Figure 2.9 that the vapor temperature at the expander outlet became smaller with the increase in shaft torque. Additionally, the

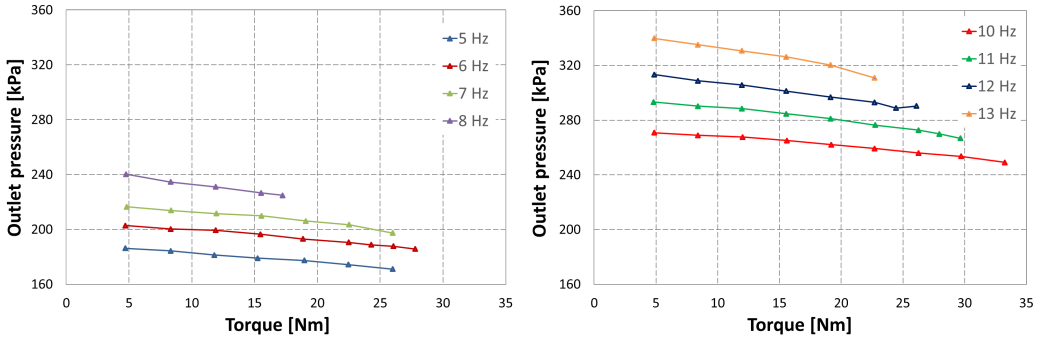

Figure 2.8: Variation of vapor pressure at the expander outlet with different shaft torques.

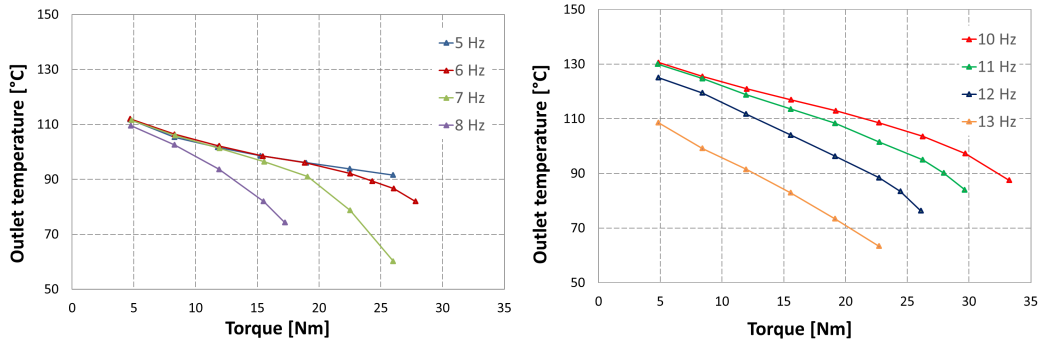

Figure 2.9: Variation of vapor temperatures at the expander outlet with different shaft torques.

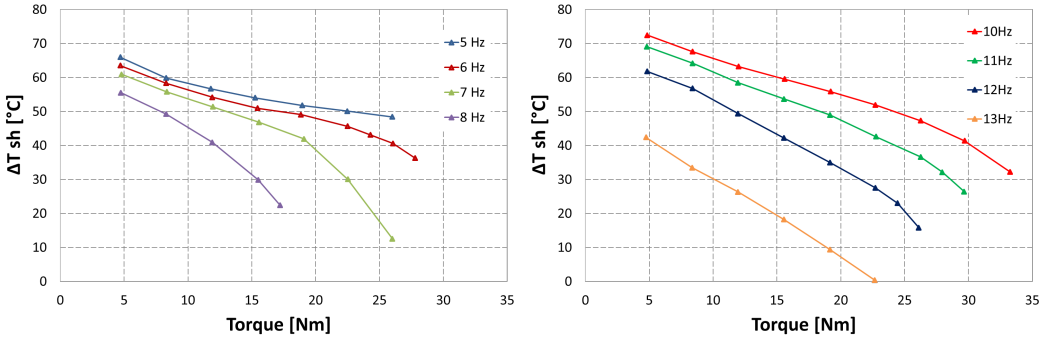

Figure 2.10: Variation of vapor superheats at the expander outlet with different shaft torques.

superheats of vapor at expander outlet also decreased with shaft torque, seen in Figure 2.10. At the same time, in Figure 2.9, it is obviously that the outlet vapor temperature is high, and it will be a good choice to recovery this part of heat by the regenerator, such as an internal heat exchanger (IHE). As regards the cooling process it worth underline that a certain degrees of sub cooling are required to avoid the cavitation of the pump. For the present ORC prototype, the current degrees of sub cooling were not enough for the suction of the pump, so a centrifuge pump was installed between the piston pump and the fluid tank to pressurize the working fluid at the inlet of the evaporator.

2.5 Effect of the pumping frequency and shaft torque on expander performance

The pressure ratio and temperature drop through the expander are calculated based on the tested results and summarized in Figure 2.11 and 2.12. As the pressure sensors were installed on the tubes connecting with expander inlet and outlet, the pressure ratio in Figure 2.11 is the so called "external pressure ratio". A bigger pressure ratio means a higher driving force to the expander. For a given PF, the pressure ratio became higher with the increase in the shaft torque because of the step increase in the vapor pressure at the expander inlet with the shaft torque (seen in Figure 2.5).
In contrast, for a given shaft torque, the pressure ratio became lower with the increase in the PF due to the higher outlet vapor pressure at the higher PF. When the shaft torque is low, the effect of PF on the pressure ratio is weak. Take shaft torque at 4.8 Nm and oil temperature of 160 $°C$ for example, the pressure ratios at all PFs are around 2.9-3.0. And, with the increase in the shaft torque, the influence of PF became significant. At the shaft torque of 19.15 Nm, the pressure ratio vary from 2.97 to 4.36. In the present test, the highest pressure ratio is about 6.5, shown in Figure 2.11. For the adopted scroll expander, it worked in the condition of under-expansion.
In Figure 2.12, generally speaking, the temperature drop between the inlet and outlet of the expander increase with shaft torque because the enlarged pressure drop optimize the operation of the expander. And it is also seen that temperature drop at PFs of 7, 12 and 13 Hz deviate significantly from the original trend and jump to a very high level when the shaft torque is large. This phenomenon can be explained by the results in Figure 2.7. The degrees of superheat at the expander inlet with large shaft torque for these three PFs is too small (around 0 $°C$). Thus, liquid entrainment at the expander inlet happened and led to the flash evaporation of R123 droplets in the expander

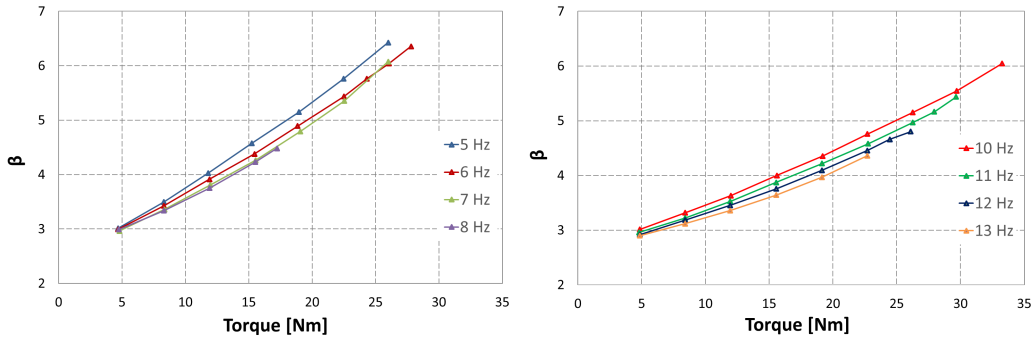

Figure 2.11: Variation of the pressure ratio of the expander with different shaft torques.

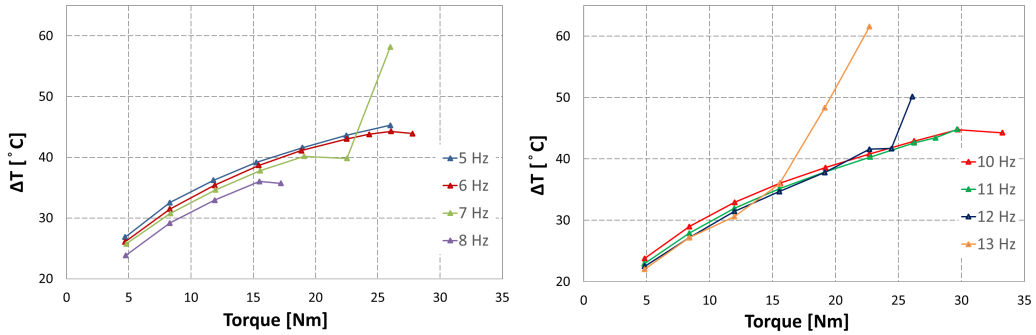

Figure 2.12: Variation of the temperature drop through the expander with different shaft torques.

chambers. The latent heat of the phase change make the vapor temperature decrease significantly. At the same time, the too small degrees of R123 superheat also means the increase of R123 temperature at the expander inlet with the increase in shaft torque, which had been mentioned above. As a result, the temperature drop became very large.

Figure 2.13 shows the variation of the rotating speed of the expander with different shaft torques. Clearly, the rotating speed decrease with the shaft torque. And for a specified shaft torque, the larger PF led to the higher rotating speed as long as R123 at the expander inlet is at vapor phase. When liquid entrainment occur, the rotating speed decrease rapidly and deviate from the original trend. Besides, when justifying the PF from 5 Hz to 6 Hz and then to 7 Hz, the rotating speed increase fast. However, when the PF was higher than 8 Hz, the increase of PF has very limited effect on rotating speed.

Based on the tested temperatures and pressures at expander inlet and out-

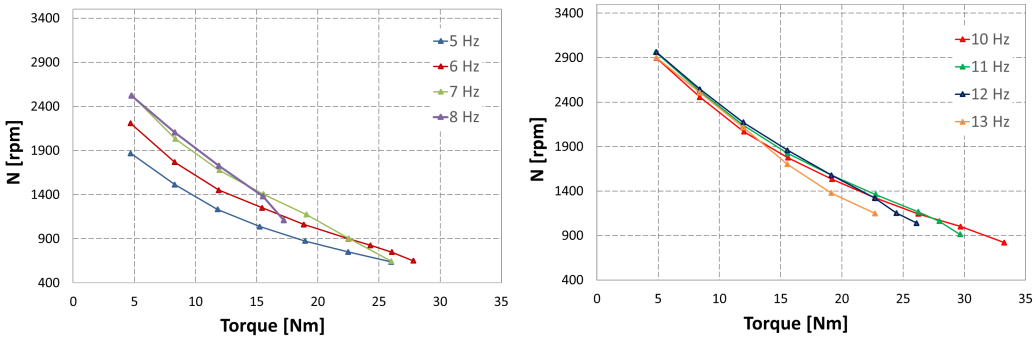

Figure 2.13: Variation of the rotating speed of the expander with different shaft torques.

let, the isentropic efficiencies are calculated and shown in Figure 2.14. It is noted that the enthalpy and entropy of R123 at expander inlet could not be determined by the tested temperature and pressure when liquid entrainment occurred as the mass fraction of liquid in vapor phase is unknown. Consequently, the isentropic efficiencies under those situations are not obtained and given in Figure 2.14. It can be seen that, for a given PF, the expander isentropic efficiency first increase with the shaft torque, reach the peak, and then decrease with the further increase in the shaft torque. The mechanism of how the sensitive factors, such as heat released to the environment, pressure loss in suction and exhaust, mechanical friction and internal leakage affect the isentropic efficiency is very complicated.
Zheng et al. [25] consider hard to explain the trends just based on the experimental results. Lemort et al. [16] modeled the scroll expander and obtained the trend of isentropic efficiency versus the pressure ratio. And these trends in Figure 2.14 agree well with their results. Besides, the increase in PF led the decrease in expander isentropic efficiency at a specified shaft torque, seen in Figure 2.14.

2.6 Deviation of the system performance from the calculated one

Comparison of the tested shaft powers with the calculated ones is shown in Figure 2.15 and 2.16. On one hand, the calculated shaft powers are much higher than the tested ones. At oil temperature of 140 $°C$, the highest calculated shaft power is 2940 W while the tested one was 2350 W, approximately 20% lower. And the data for oil temperature of 160 $°C$ are 3820 W, 3245 W and 15% lower. On the other hand, the profiles of calculated shaft power

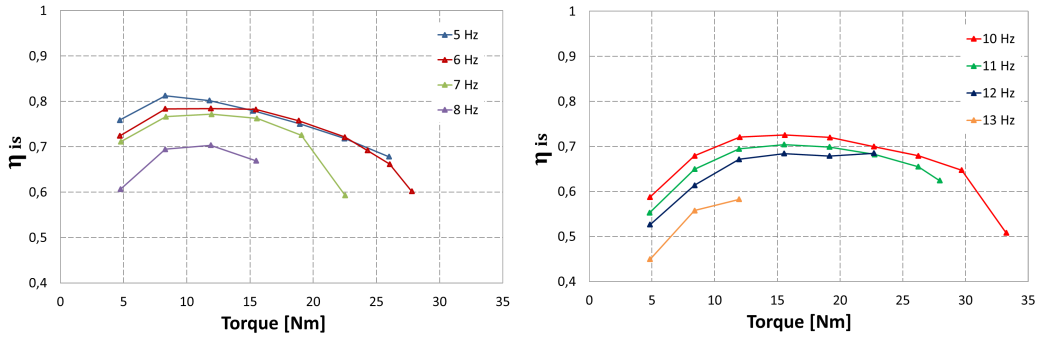

Figure 2.14: Variation of the isentropic efficiency of the expander with different shaft torques.

exhibits similar trends with tested ones. The shaft power was the product of the shaft torque and rotating speed. This gap between the powers is the the possible consequence of the ambient heat losses that afflict the expander.
At a specified PF in Figures 2.15 and 2.16, the shaft power first increase with shaft torque, reach the highest value and then move down. Besides, when the PF is low, the increase in the PF could improve the shaft power. However, when the PF is high, the further increase in the PF could make the expander encounter the (liquid entrainment prematurely), which would bring down the shaft power.

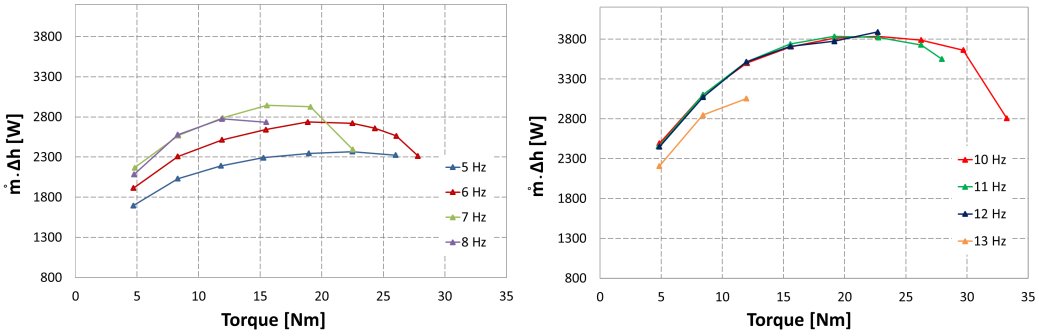

Figure 2.15: Calculated shaft powers of the expander at a temperature of heat source 140 $°C$ on the left and 160 $°C$ on the right.

In Figure 2.15 and 2.16, it is seen that, for the present ORC system, the proper PFs are 7 Hz for 140 $°C$ and 11 Hz for 160 $°C$. The calculated system thermal efficiencies are much higher than the tested ones. The big difference between the calculated and tested ORC expander efficiency, in the author's opinion, are once again probably due to ambient heat losses which

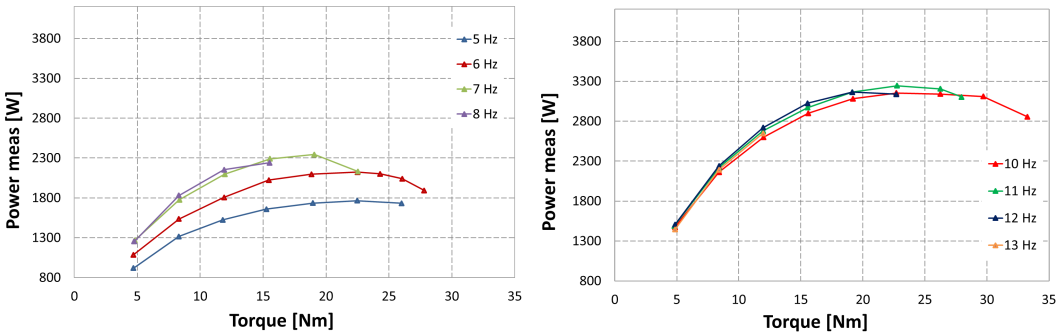

Figure 2.16: Tested shaft powers of the expander at a temperature of heat source 140 $°C$ on the left and 160 $°C$ on the right.

will be examined in the next chapters.

Chapter 3

Scroll expander model

Technical papers dealing with small-size ORC systems do not always consider a specific modelling for the expander. As a matter of fact, there are several literature works focusing on the feasibility study of the ORC system and the selection of the proper working fluid. In such theoretical works, the expander efficiency is taken constant in spite of variable operating conditions, such as fluid pressure and temperature at the inlet of the machine, expansion pressure ratio, type of working fluid, etc.
As a first example, the results of thermodynamic simulations of a 2 kW_{el} biomass-fired CHP system were presented by Liu et al. [26], assuming a constant isentropic expander efficiency equal to 85%, as suggested by Saleh et al. [27], despite in that work such a value was originally chosen for a power output of 1 MW. As a second example, twenty fluids for a solar ORC system generating 2 kW of power output were investigated by Tchanche et al. [28], with an isentropic expander efficiency fixed at 0.7. Although the last efficiency value is more realistic for a few kW-size expander, the machine is considered adiabatic and, consequently, the condenser heat duty is overestimated. As a last example, a thermodynamic criterion to select the most suitable working fluid for ORC combined heat and power units (CHP) in small households (for 3-4 kW) was proposed by Mikielewicz and Mikielewicz [29], based on an isentropic expansion. Besides, there is another issue, specifically regarding the working fluid, in addition to the one related to constant expansion efficiency.
As a matter of fact, researches oriented to investigate the proper fluid selection for ORC applications often propose solutions, e.g. HCFCs, that are to be phased out according to current regulations. As an example, both HCFC-123 and HCFC-141b are suggested in the relatively recent paper by Mikielewicz and Mikielewicz [29], because they allow for higher thermal efficiency. Likewise, these HCFCs are also included in the previously mentioned

study by Tchanche et al. [28], as well as in very recent studies by Wang et al. [30] and by Xi et al. [31], with the latter even recommending CFC-11 for its superior thermodynamic performance.

3.1 Presentation of the model

A novel performance simulation tool of a scroll expander is proposed in this chapter. The proposed procedure aims at revising the scroll expander model originally developed by Lemort et al. [16], in order to strengthen it from a physical point of view. The expander model is calibrated in the next chapter, and then validated according to the experimental data given by Zheng et al. [25]. Investigation and optimization of several operating points will be carried out, so the new expander model can be implemented in a whole ORC system software that can help in designing the entire ORC facility.
A description of the expansion process, along with the related equations, is included in this section. The conceptual scheme of the expander model is shown in Figure 3.1. In this model, the evolution of the fluid through the expander is decomposed into the following consecutive steps:

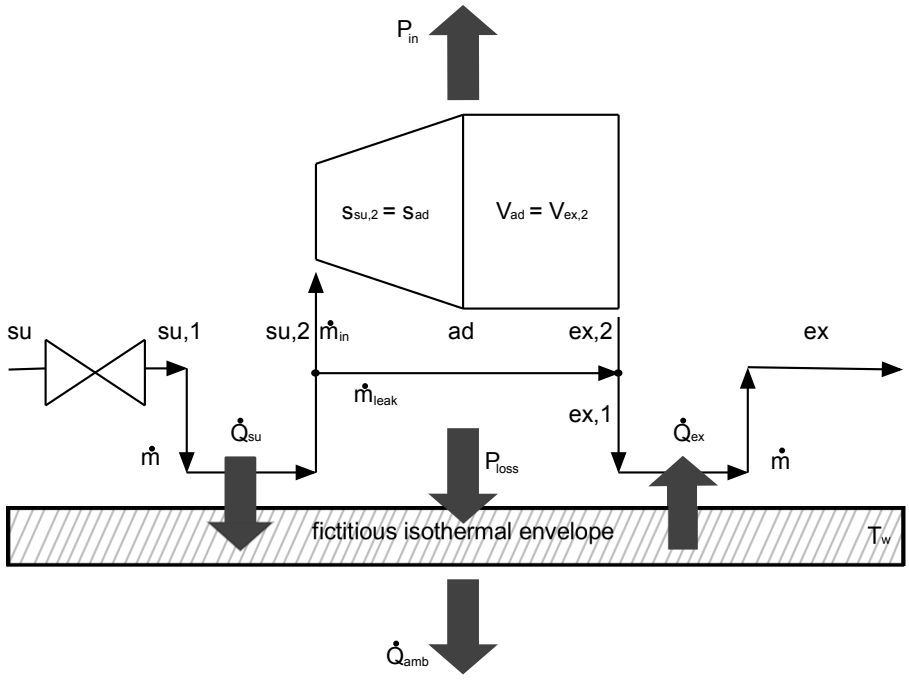

Figure 3.1: Conceptual scheme of the expander model proposed by Lemort et al. [16]

(a) Isoenthalpic supply pressure drop (su→su,1).

(b) Isobaric supply cooling-down (su,1→su,2).

(c) Internal leakage (su,2→ex,2).

(d) Isoentropic expansion to the adapted pressure (su,2→ad).

(e) Adiabatic expansion at constant machine volume (ad→ex,2).

(f) Isoenthalpic fluid mixing (ex,2→ex,1).

(g) Isobaric exhaust heating-up or cooling-down (ex,1→ex).

Looking at the expander scheme in Figure 3.1, it can be observed that the heat transfer rates, the supply pressure drop throttling and the internal leakage are fictitiously dissociated from the actual expansion process (su,2→ex,2). All the mentioned processes hereunder are better described and modelled in the following paragraphs.

3.1.1 Isoenthalpic supply pressure drop (su→su,1)

The supply pressure drop ($p_{su} \rightarrow p_{su,1}$) accounts for all pressure losses encountered by the fluid from the suction line to the suction chamber. Major pressure losses are associated to two phenomena [16]:

1. As shown in Figure 3.2, during part of the suction process, the expander suction port is blocked by the tip of the orbiting scroll, reducing the effective suction port area.

2. At the end of the suction process, the flow passage between the central portion of the suction chamber and the two adjacent crescent-shaped portions is progressively reduced to zero. However, the tip seal does not extend to the end of the scrolls, which increases the flow between the central and the adjacent chambers and attenuates the supply pressure drop.

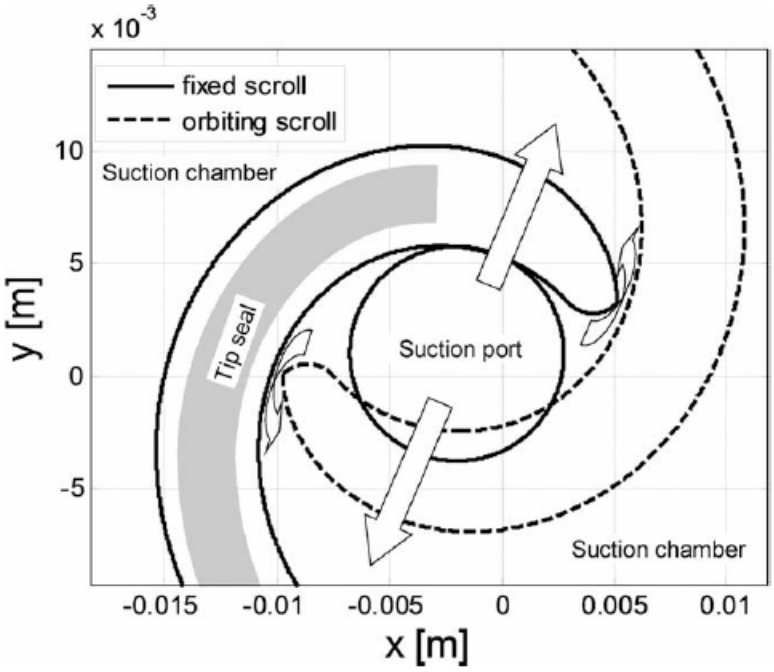

Figure 3.2: Representation of the suction chamber at the end of the suction process [16].

The lumped supply pressure drop throttling is simulated based on the isoentropic flow through a simple converging nozzle, whose cross-sectional area A_{su} is a parameter to identify. Because of the steady-state nature of the model, this cross-sectional area represents an average value of the suction port effective area over the entire suction process. By combination of the equations of mass and energy conservation through the nozzle, the mass flow rate entering the expander can be expressed as:

$$\mathring{m} = A_{su} \cdot \rho_{thr,su} \cdot \sqrt{2 \cdot (h_{su} - h_{thr,su})} \tag{3.1}$$

Both the specific enthalpy $h_{thr,su}$ $[J/kg]$ and density $\rho_{thr,su}$ $[kg/m^3]$ are functions of the pressure $p_{su,1}$ at the nozzle throat and of the supply specific entropy s_{su}. Knowing the mass flow rate $\mathring{m}$ entering the expander, Eq. (3.1) can be used to compute the pressure $p_{su,1}$ and vice versa. Considering the throttling through the nozzle, the fluid stream velocity at the throat is dissipated into internal energy. Thus the total enthalpies at the inlet h_{su} and outlet $h_{su,1}$ of the nozzle are the same.

$$h_{su,1} = h_{su} \tag{3.2}$$

This is a refinement that was not included by Lemort et al. [16] in their model. The throttling here simulated is more correct from an energy conservation point of view.

3.1.2 Isobaric and exhaust heat transfers

The main heat transfer mechanisms inside the scroll expander occur between:

1. the expander shell and the fluid in the supply and exhaust pipes;
2. the scrolls (fixed and orbiting) and the fluid in the suction, expansion and discharge chambers;
3. between the shell and the ambient.

Both supply and exhaust heat transfers are simulated by introducing a fictitious metal envelope with uniform temperature T_w. This fictitious envelope represents the metal mass associated to the expander shell, the fixed and the orbiting scrolls. The supply heat transfer rate in agreement with [33], is given by:

$$\mathring{Q}_{su} = \mathring{m} \cdot (h_{su,1} - h_{su,2}) = \left[1 - e^{\left(\frac{-AU_{su}}{\mathring{m} \cdot cp}\right)}\right] \cdot \mathring{m} \cdot cp \cdot (T_{su,1} - T_w) \tag{3.3}$$

The supply heat transfer coefficient AU_{su} is supposed to vary with the mass flow rate and takes into account only the convective heat transfer coefficient of the working fluid, (the conductive thermal resistance of the scroll wraps is negligible due to the high metal thermal conductivity and small thicknesses). The study of the heat transfer coefficients is based on the Reynolds' analogy for a fully-developed turbulent flow. The Dittus-Boelter correlation valid for turbulent flow in pipes [33] can be used:

$$U = \frac{Nu \cdot \lambda}{L} \tag{3.4}$$

$$Nu = 0,023 \cdot Re^{0,8} \cdot Pr^{m} \tag{3.5}$$

$$Re = \frac{\rho \cdot w \cdot D}{\mu} = \frac{\mathring{m}}{\mu \cdot D \cdot \frac{\pi}{4}} \tag{3.6}$$

$$Pr = \frac{cp \cdot \mu}{\lambda} \tag{3.7}$$

where the adimensional Nusselt number, the thermal conductivity λ $[W \cdot m^{-1} \cdot K^{-1}]$, the density ρ $[kg \cdot m^{-3}]$, kinematics viscosity μ $[N \cdot s \cdot m^{-2}]$ and isobaric heat capacity cp $[J \cdot kg^{-1} \cdot K^{-1}]$ depend on the thermo-physical condition of the specific working fluid. The exponent m in the adimensional Prantl number (Pr) is equal to 0.4 if the fluid is heated by the wall, otherwise it is equal to 0.3 (the fluid is cooled by the wall).
Expressing the ratio between the actual heat transmittance and its value at nominal flow rate conditions, a number of terms in the previous equations can be simplified. The result is a flow rate dependent heat transmittance as:

$$AU_{su} = AU_{su,nom} \cdot \left(\frac{\mathring{m}}{\mathring{m}_{nom}} \right)^{0,8} \tag{3.8}$$

where $AU_{su,nom}$ is a parameter to identify, and $\mathring{m}_{nom}$ is fixed a priori.
It is noteworthy that this heat transfer analysis has a certain degree of simplification due to the lack of information on both the heat transfer coefficient resulting from physical-phenomena and the areas where heat flux takes place inside the resulting chambers.

3.1.3 Internal leakage (su,2→ex,2)

As schematized in Figure 3.1, the mass flow rate entering the expander, according to Eq. (3.9), is split into two parts: the first $\mathring{m}_{in}$, necessary to cause the shaft to rotate at a specified rotational speed N, is related to the displacement volume of the scroll expander $V_{exp,sw}$ and the second is the leakage mass flow rate $\mathring{m}_{leak}$:

$$\mathring{m} = \rho_{su,2} \cdot V_{exp,sw} \cdot N + \mathring{m}_{leak} = \mathring{m}_{in} + \mathring{m}_{leak} \tag{3.9}$$

No useful expansion is related to fluid leakage through the machine, resulting in a significant loss.
There are two leakage paths in a scroll machine: the radial leakage due to a gap between the bottom or the top plate and the scrolls and the flank leakage resulting from a gap between the flanks of the scrolls [34]. In this modelling, as it is shown in Figure 3.1, all the leakage paths are lumped into one unique fictitious leakage clearance, whose cross-sectional area A_{leak} is a parameter to identify. The leakage flow rate can be simulated by reference to the isoentropic flow through a simply convergent nozzle, whose throat area is A_{leak}. The pressure at the inlet of the nozzle is $p_{su,2}$ and the throat pressure is the maximum between exhaust and critical pressures:

$$p_{thr,leak} = MAX(p_{ex,2}; p_{crit,leak}) \tag{3.10}$$

The critical pressure $p_{crit,leak}$ is simulated by considering the working fluid as a perfect gas, in agreement with Lemort et al. [16] work:

$$p_{crit,leak} = p_{su,2} \cdot \left[\left(\frac{2}{\gamma + 1} \right)^{\left(\frac{\gamma}{\gamma - 1}\right)} \right] \tag{3.11}$$

where γ indicates the ratio between the specific heats at constant pressure cp and at constant volume cv, calculated in conditions $su, 2$.
As for the supply pressure drop, the mass and energy conservation equations through the nozzle are combined to express the leakage mass flow rate:

$$\mathring{m}_{leak} = A_{leak} \cdot \rho_{thr,leak} \cdot \sqrt{2(h_{su,2} - h_{thr,leak})} \tag{3.12}$$

where A_{leak} is a parameter to identify and both $\rho_{thr,leak}$ and $h_{thr,leak}$ in Eq. (3.12) are calculated after the highest pressure between $p_{ex,2}$ and $p_{crit,leak}$ is determined, along with the condition:

$$s_{leak} = s_{su,2} \tag{3.13}$$

where both s_{leak} and $s_{su,2}$ are specific entropies $[J \cdot (kgK)^{-1}]$.

3.1.4 Isoentropic expansion to the adapted pressure (su,2→ad)

After initial cooling, the working fluid goes through an adiabatic and reversible expansion to the adapted pressure ($p_{su,2} \rightarrow p_{ad}$). This process reduces the pressure of the working fluid from the value $p_{su,2}$, to a pressure of adaptation p_{ad} imposed by the BVR (Built-In Volume ratio). The BVR is an intrinsic geometric parameter of the volumetric machine. In order to characterize this process, reference is made to the expression that relates pressures and specific volumes, assuming that the vapor phase of the working fluid can be simulated as a perfect gas:

$$p_{su,2} \cdot v_{su,2}^{\gamma} = p_{ad} \cdot v_{ad}^{\gamma} \tag{3.14}$$

where $v_{su,2}$ and v_{ad} indicate the specific volume $[m^3 \cdot kg^{-1}]$, respectively evaluated in $su, 2$ and ad, while γ is always the ratio of specific heats at constant pressure cp and at constant volume cv, calculated in conditions $su, 2$. Eq. (3.14) can be suitably reformulated to clarify the dependence of the pressures on the densities (rather than from specific volumes) and the volume ratio BVR, as follows:

$$\frac{p_{ad}}{p_{su,2}} = \left(\frac{v_{su,2}}{v_{ad}}\right)^{\gamma} = \left(\frac{\rho_{ad}}{\rho_{su,2}}\right)^{\gamma} = \left(\frac{1}{BVR}\right)^{\gamma} \tag{3.15}$$

Based on the Eq. (3.15), the "adapted" thermodynamic state in ad is known when the thermodynamic state in su_2 is defined.

3.1.5 Adiabatic expansion at constant machine volume (ad→ex,2)

The transformation $ad \rightarrow ex, 2$ is modeled based on constant volume of the machine. The volumetric expanders can be operated into two distinct modes when the final pressure is not the adapted one, i.e. under- or over- expansion (see Figure 3.3); Under-expansion occurs when the internal pressure ratio imposed by the expander geometry ($p_{su,2}/p_{ad}$) is lower than the system pressure ratio ($p_{su,2}/p_{ex,2}$). In this case, the pressure in the expansion chamber at the end of the expansion process (p_{ad}) is higher than the pressure in the discharge line. This is represented in Figure 3.3 (a). The modelling assumes that there is no pressure drop through the discharge port. In order to equalize the pressures in the discharge chambers (the former expansion chambers) and in the discharge line, some fluid ($\triangle \mathring{m}_{in}$ in in Eq. (3.16)) has to flow out of the discharge chambers. The modelling assumes it is achieved instantaneously as soon as the expansion chambers open onto the discharge line. The energy balance over the discharge chamber can be expressed as follows:

$$(\mathring{m}_{in} - \triangle \mathring{m}_{in}) \cdot u_{ex,2} - \mathring{m}_{in} \cdot u_{ad} = -\triangle \mathring{m}_{in} \cdot h_{ex,2} \tag{3.16}$$

Over-expansion occurs when the internal pressure ratio imposed by the expander geometry is higher than the system pressure ratio (Figure 3.3 (b)). The energy balance over the discharge chamber is then similar to the one already established for the under-expansion process:

$$(\mathring{m}_{in} + \triangle \mathring{m}_{in}) \cdot u_{ex,2} - \mathring{m}_{in} \cdot u_{ad} = \triangle \mathring{m}_{in} \cdot h_{ex,2} \tag{3.17}$$

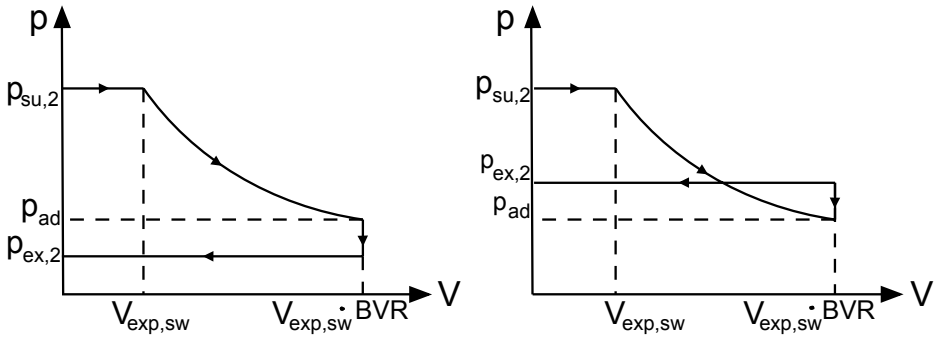

Figure 3.3: Schematic of: a) under- and, b) over-expansion processes in the $p-V$ diagram.

3.1.6 Isoenthalpic fluid mixing (ex,2→ex,1)

The transformation $ex,2 \rightarrow ex,1$ is simulated according to an isobaric and adiabatic mixing between the mass flow rate $\mathring{m}_{in}$ actually processed by the expander, in the thermodynamic conditions $ex,2$, and the leakage flow rate $\mathring{m}_{leak}$, in the conditions of enthalpy characteristic of status $su,2$ since it is an isoenthalpic throttling.
Thus the equation representative of isobaric and adiabatic mixing between these two streams can be written as:

$$\mathring{m}_{leak} \cdot h_{su,2} + \mathring{m}_{in} \cdot h_{ex,2} = (\mathring{m}_{leak} + \mathring{m}_{in}) \cdot h_{ex,1} \tag{3.18}$$

from which it is possible to obtain the enthalpy $h_{ex,1}$ $[J \cdot kg^{-1}]$ downstream of the mixing.

3.1.7 Isobaric exhaust heating-up or cooling-down (ex,1→ex)

As previously mentioned , the final transformation $ex,1 \rightarrow ex$ can be related to an isobaric heating-up or cooling-down for the working fluid, depending on the temperature $T_{ex,1}$ downstream of the isoenthalpic mixing. In order to know the direction of the thermal flux, $T_{ex,1}$ is compared to T_w, the temperature associated with the fictitious wall. The discussion of this process is similar to the one already developed for the heat transfer at the inlet of the expander, so it is omitted, for the sake of brevity.

3.2 Power output

One working cycle of the scroll expander includes three processes: suction, expansion and discharge [34]. During the suction process, the suction chamber is in communication with the supply line and the fluid flows into the chamber. The expansion process starts when the suction chamber ceases to be in communication with the supply line. The discharge process begins when the discharge chambers enter in communication with the discharge line. The internal power $\mathring{W}_{in}$ produced by the machine is a combination of the suction $\mathring{W}_{suc}$, the expansion $\mathring{W}_{exp}$ and discharge $\mathring{W}_{dis}$ powers. Moreover, since the internal expansion process (su,2→ex,2) is assumed to be adiabatic, the internal power can be expressed as function of initial and final enthalpy states:

$$\mathring{W}_{in} = \mathring{W}_{suc} + \mathring{W}_{exp} + \mathring{W}_{dis} \tag{3.19}$$

3.2.1 Suction power

The energy balance across the suction chamber, between the beginning and the end of the suction process yields:

$$\mathring{W}_{suc} = \mathring{m}_{in} \cdot (h_{su,2} - u_{su,2}) = \mathring{m}_{in} \cdot p_{su,2} \cdot v_{su,2} = p_{su,2} \cdot \mathring{V}_{s,exp} \tag{3.20}$$

where $\mathring{V}_{s,exp}$ $[m^3 \cdot s^{-1}]$ is the volumetric flow rate defined as $V_{exp,sw} \cdot N$.

3.2.2 Expansion power

The expansion process is assumed to be adiabatic and isoentropic, consequently reversible. Writing the energy balance between the beginning and the end of this process yields:

$$\mathring{W}_{exp} = \mathring{m}_{in} \cdot (h_{su,2} - p_{su,2} \cdot v_{su,2} - h_{ad} + p_{ad} \cdot v_{ad}) = \mathring{m} \cdot (u_{su,2} - u_{ad}) \tag{3.21}$$

3.2.3 Discharge power

As for the suction process, the equation of energy conservation is applied on the discharge chamber between the beginning and the end of the discharge process, yielding:

$$\mathring{W}_{dis} = -(\mathring{m}_{in} \pm \triangle\mathring{m}_{in}) \cdot p_{ex,2} \cdot v_{ex,2} = -BVR \cdot p_{ex,2} \cdot \mathring{V}_{s,exp} \tag{3.22}$$

3.2.4 Internal power

By revisiting the Eqs. (3.16) and (3.17), the mass flow discrepancy resulting from over- and under-expansion could be exploited as:

$$\triangle\mathring{m} = \pm\mathring{m} \cdot \frac{(u_{ex,2} - u_{ad})}{(u_{ex,2} - h_{ex,2})} = \pm\mathring{m} \cdot \frac{(u_{ex,2} - u_{ad})}{p_{ex,2} \cdot v_{ex,2}} \tag{3.23}$$

respectively. So this $\triangle\mathring{m}$ can be replaced in Eqs. (3.20), (3.21) and (3.22). The internal power of the expander derives from the combination of these three equations as indicated in Eq. (3.19):

$$\mathring{W}_{in} = \mathring{m}_{in} \cdot (h_{su,2} - u_{su,2}) + \mathring{m}_{in} \cdot (u_{su,2} - u_{ad}) - (\mathring{m} \pm \triangle\mathring{m}) \cdot p_{ex,2} \cdot v_{ex,2} \tag{3.24}$$

$$\mathring{W}_{in} = \mathring{m}_{in} \cdot (h_{su,2} - \cancel{u_{su,2}} + \cancel{u_{su,2}} - \cancel{u_{ad}}) - [\mathring{m}_{in} \cdot (p_{ex,2} \cdot v_{ex,2} + u_{ex,2} - \cancel{u_{ad}})] \tag{3.25}$$

$$\mathring{W}_{in} = \mathring{m}_{in} \cdot (h_{su,2} - u_{ex,2} - p_{ex,2} \cdot v_{ex,2}) = \mathring{m}_{in} \cdot (h_{su,2} - h_{ex,2}) \tag{3.26}$$

It is now clear that the internal power of the expander is dependent on thermodynamic states su,2 and ex,2 only.

3.2.5 Shaft power

Mechanical losses are mainly due to friction between the scrolls and in the bearings, bringing about a reduction of the internal power. In the present modelling, this power loss $\mathring{P}_{loss}$ is simulated as a function of three parameters as follows:

$$\mathring{P}_{loss} = \mathring{P}_{loss}(\varphi, f_{frict}, N) \tag{3.27}$$

where φ is the load of the machine imposed by the working conditions, f_{frict} $[N \cdot m]$ is the friction factor, and N is the shaft speed.
The adapted expansion is investigated for the sake of simplicity. The "work per cycle" is shown in Figure 3.4 and it can be defined as:

$$\oint p \cdot dV = L_c = p_{me} \cdot V_{exp,sw} \cdot BVR \tag{3.28}$$

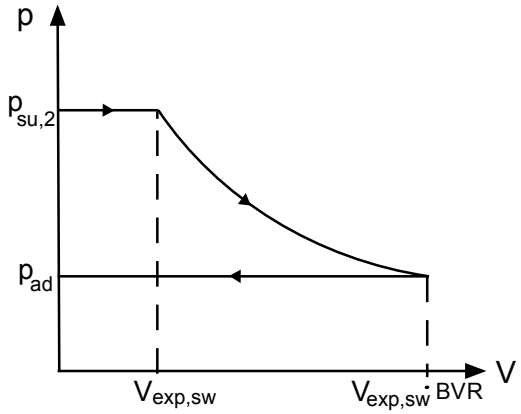

Figure 3.4: $p - V$ diagram of the expander under "adapted" conditions

where $V_{exp,sw}$ is the displacement volume $[cm^3/rev]$ of the expander. In analogy with the internal combustion engine (ICE) an internal mean effective pressure p_{me} $[Pa]$ is defined. Thus L_c is a work per cycle and is measured in Joule. The p_{me} is the force per unit of area that presses the orbiting scroll against the fixed scroll as can be seen in Figure 3.5. The sliding speed $\overrightarrow{u}$ of the orbiting scroll is:

$$\overrightarrow{u} = \vec{\omega} \cdot R \tag{3.29}$$

where $\overrightarrow{\omega}$ is the angular velocity $[rad \cdot sec^{-1}]$ and R is the radial distance of the contact point between the scrolls. In order to obtain the internal power of the expander the work per cycle has to be multiplied by the shaft speed N $[rpm]$:

$$L_c \cdot {}^{N}/_{60} = \mathring{W}_{in} = p_{me} \cdot V_{exp,sw} \cdot BVR \cdot {}^{N}/_{60} \tag{3.30}$$

So turning the Eq. (3.30) a definition of p_{me} can be extrapolated:

$$p_{me} = \frac{\mathring{W}_{in}}{BVR \cdot V_{exp,sw} \cdot N} = \frac{1}{BVR \cdot \cancel{V_{exp,sw}} \cdot \cancel{N}} \cdot \rho_{su,2} \cdot \cancel{V_{exp,sw}} \cdot \cancel{N} \cdot (h_{su,2} - h_{ex,2}) \tag{3.31}$$

Considering that:

$$\rho_{ad} = \frac{\rho_{su,2}}{BVR} \tag{3.32}$$

The Eq. (3.31) becomes:

$$p_{me} = \rho_{ad} \cdot (h_{su,2} - h_{ex,2}) \tag{3.33}$$

This is an easy way to take into account the dependence of power loss on the load of the machine.

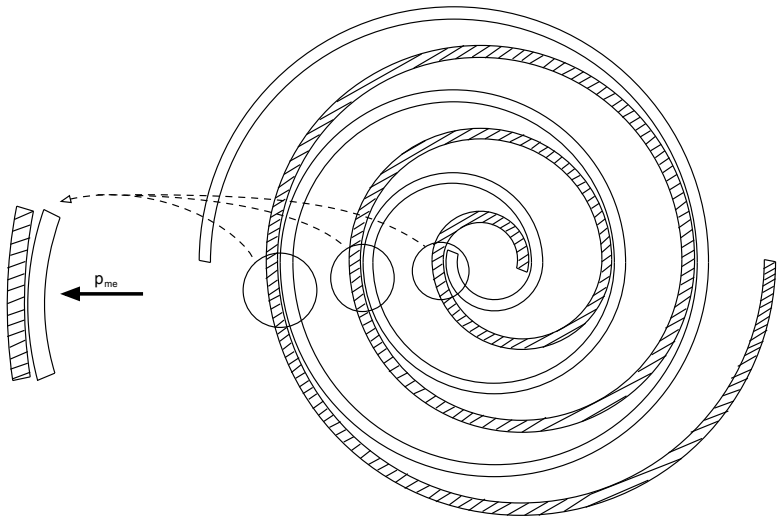

Figure 3.5: Detail of the scroll expander that explains how the p_{me} press the spirals against each other.

Once p_{me} has been calculated, a friction force can be simulated as:

$$F_{fric} \propto f_{fric} \cdot p_{me} \tag{3.34}$$

As a matter of fact, another important factor that weights gravely on the power losses is the the friction factor $f_{fric.}$. The accurate prediction of frictional loss is one of the most important tasks for the scroll machine design, and it is necessary for the improvement of the whole ORC system performance. In particular, a certain amount of lubricant is sent through the chamber of the scroll expander tested in this work by means of a pump, and it is removed at the outlet by means of an efficient liquid-vapor separator, because oil particles can lead to system internal cycle problems (they reduce the heat transfer in the evaporator). The friction factor is velocity dependent, as can be shown in Figure 3.6, where the Stribeck curve is represented.
The figure underlines three different schemes of friction as a function of the shaft speed, in presence of lubricant:

1. boundary lubrication
2. mixed-film lubrication
3. full hydrodynamic lubrication

In this work the shaft expander runs beyond the limit of 600 rpm that ensures the full hydrodynamic lubrication, so the friction factor continuously increases with the shaft speed.
Power losses do depend on the velocity since the friction force in Eq. (3.34) has to be multiplied by the sliding velocity of the orbiting scroll, as in Eq. (3.35):

$$\mathring{P}_{loss} = F_{fric} \cdot \overrightarrow{u} \propto f_{frict} \cdot p_{me} \cdot \omega \tag{3.35}$$

Finally, the equation that simulates power losses in a scroll expander and takes into account all the previously introduced contribution parameters is expressed as:

$$\mathring{P}_{loss} = p_{me} \cdot (a + b \cdot \omega^n) \cdot \omega = p_{me} \cdot (a \cdot \omega + b \cdot \omega^{n+1}) \tag{3.36}$$

where a, b and n are parameters to identify.
Thus, the shaft power results from the internal power $\mathring{W}_{in}$ reduced by the power losses $\mathring{P}_{loss}$:

$$\mathring{W}_{shaft} = \mathring{W}_{in} - \mathring{P}_{loss} \tag{3.37}$$

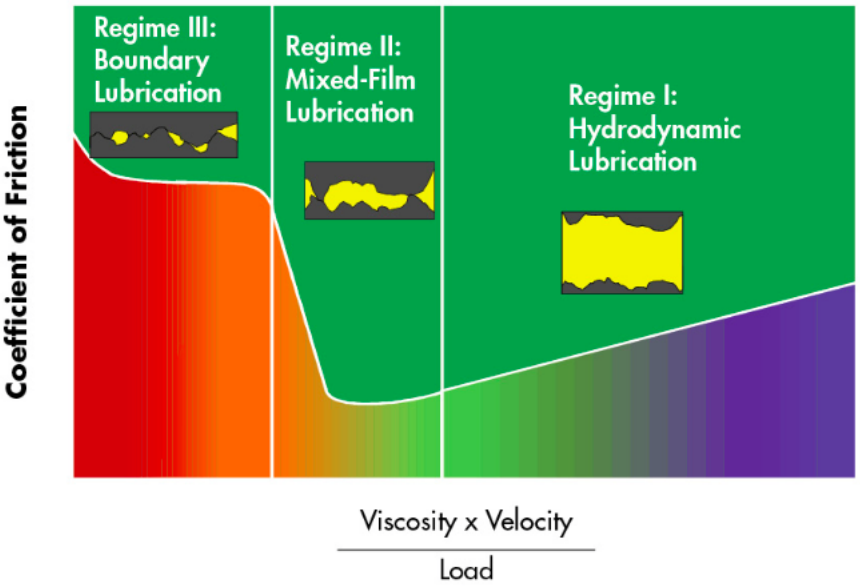

Figure 3.6: Stribeck curve showing three lubrication regimes.

3.3 Heat ambient losses

As previously mentioned the scroll machine is affected by heat losses through the external ambient and this leads to a deterioration in the whole cycle performance. And for this reason the expander should be properly insulated. An isoentropic efficiency figure is not suited for this type of expander and a new definition is required. Assuming the expander placed in an environment with still air is reasonable to think that the phenomenon of heat transfer is due to natural convection. And since the expander has a cylindrical shape and is placed in a horizontal position, it is comparable to natural convection of external horizontal cylinders.
The flow regime depends on the maximum temperature reached by the wall at a constant temperature T_w. The higher the T_w, the higher the driving force governing the phenomenon, the higher the relative density difference between air near the envelope and the air far from it. Thus the air flow that runs into the external shell gains speed and the regime could become turbulent and unstable, and so the heat transfer increases. In this case the ambient losses between the envelope and the ambient are modeled by introducing the correlation proposed by Mc Adams [35] that is suited for laminar flow onto horizontal cylinder:

$$Nu = C_{wall} \cdot (Ra)^{1/4} \tag{3.38}$$

where C_{wall} is a model parameter to identify and Ra is the Rayleigh adimensional number that is the product between the Prandtl adimensional number Pr defined in Eq. (3.7) and the Grashof adimensional number defined as:

$$Gr = \frac{g \cdot \beta \cdot L^3 \cdot (T_w - T_\infty)}{\nu^2} \tag{3.39}$$

which represents the ratio among the buoyant and the viscous forces on the fluid. It is a fundamental parameter for the natural convection. the parameter $\beta = \frac{1}{V}\frac{\partial V}{\partial T}$ in the Eq. (3.39), is the isobaric compressibility coefficient. V is the volume $[m^3]$ and T is temperature $[K]$. And for a perfect gas $\beta = \frac{1}{T_{film}}$ where T_{film} is the arithmetic average temperature between ambient and envelope wall. In addition, g is the acceleration of gravity $[m \cdot s^{-2}]$, L is a characteristic length of the body [m], ν is the kinematic viscosity $[m^2 \cdot s]$ and T_w and T_∞ are the envelope wall and the ambient temperatures respectively. Then the heat transfer coefficient for the external air is extrapolated:

$$U = \frac{Nu \cdot \lambda}{L} \tag{3.40}$$

And the heat ambient losses are:

$$\mathring{Q}_{amb} = \frac{C_{wall} \cdot (Ra)^{1/4} \cdot \lambda}{L} \cdot A_{ext} \cdot (T_w - T_{amb}) \tag{3.41}$$

Where L is the diameter and A_{ext} is the outside area of the scroll expander that is treated as a cylinder having an external surface of $A_{ext} = D \cdot L_{exp}$, which are two known values.
The whole process of expansion is shown in Figure 3.7 where the black continuos line represents the path of the working fluid in accordance with this model, while the dashed blue line is the polytropic irreversible transformation that connects the start and end points.
In Figure 3.7 (a) the expander is working in under-expansion mode, so the pressure at the end of the isoentropic expansion has to drop in the isovolumic expansion to match the exit pressure that coincides with the condensation pressure. In Figure 3.7 (b) it can be seen that the expander is working in over-expansion and the Built-in-volume ratio of the machine is redundant for the condition examined. Thus the pressure at the end of the isoentropic

pressure is lower than the condensation one and a certain amount of fluid fall again into the expander to re-establish the same pressure level. (Thanks to the fact that R123-Joule-Thomson coefficient is lower than unity, because of the non-perfect-law behavior in the gas phase, it can be also seen in Figure 3.7 that the isoenthalpic outlet fluid temperature is lower than the incoming one).

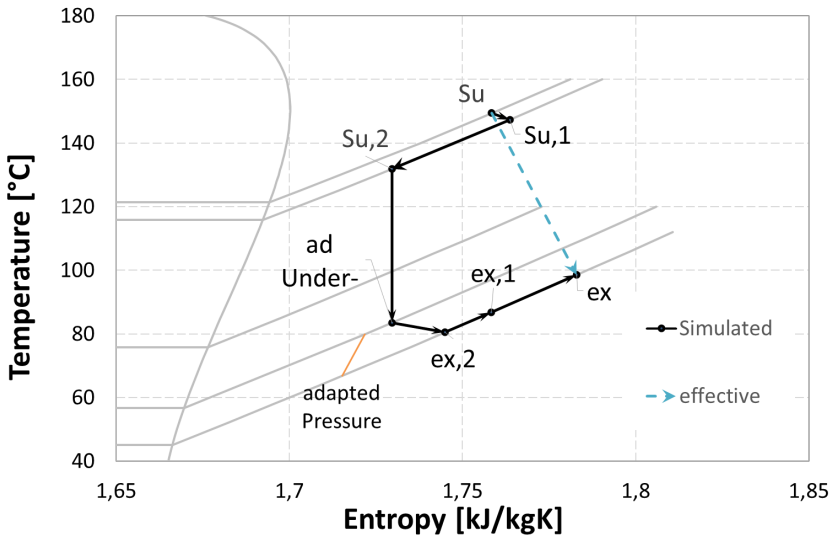

(a)

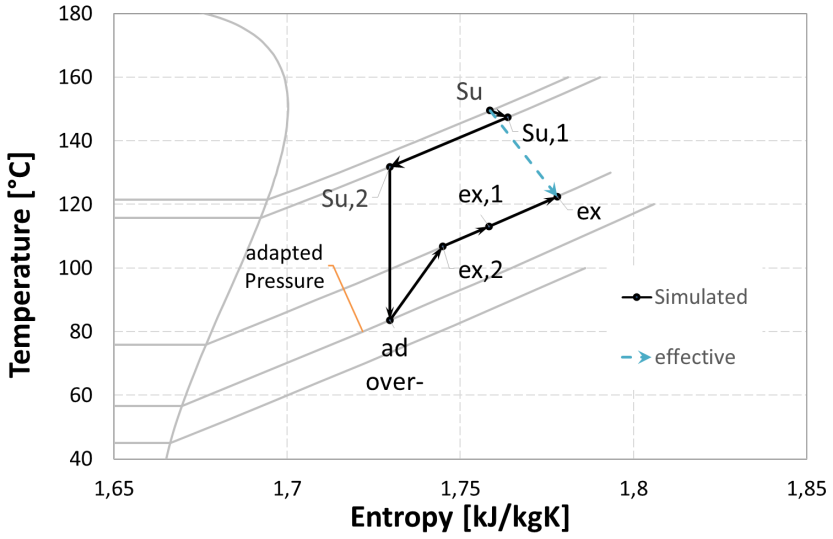

(b)

Figure 3.7: T-s diagram of: (a) under-expansion and, (b) over-expansion

3.4 Performance indicators

After the explanation of all the expansion process steps it is necessary to define an appropriate expander efficiency indicator, since a heat exchange with the surroundings has been included in the energy control volume balances. For this reason the expander efficiency given in Eq. (2.3) is suitable for adiabatic machines only. In order to close the lumped parameter energy balance on the control volume of the expander, the equation of the first law of thermodynamics is reported:

$$\mathring{m} \cdot (h_{in} - h_{out}) - \mathring{Q}_{amb} - \mathring{W}_{shaft} = 0 \tag{3.42}$$

from which the useful power of the expander in the real process can be obtained :

$$\mathring{W}_{shaft} = \mathring{m} \cdot (h_{in} - h_{out}) - \mathring{Q}_{amb} \tag{3.43}$$

This useful power can be compared with the isoentropic drop that ideally can be transformed in shaft power. The ratio of these two items provides the expander efficiency:

$$\eta_{exp} = \frac{\mathring{W}_{shaft}}{\mathring{m} \cdot (h_{in} - h_{out,is})} = \frac{\mathring{m} \cdot (h_{in} - h_{out}) - \mathring{Q}_{amb}}{\mathring{m} \cdot (h_{in} - h_{out,is})} \tag{3.44}$$

where $h_{out,is}$ $[^{J}/_{kg}]$ is the enthaply calculated at p_{out} and $s_{in} = s_{out}$.
In order to gain sensitivity to the behavior of the scroll expander performance, it is useful to recall the theory of positive displacement machines under the following simplifying assumptions:

- the scroll expander is not affected by heat losses.
- the entire mass flow is processed by the spirals of the scroll to give useful work. Leakage losses are not present.
- there are no pressure losses at the intake.
- the fluid is considered as perfect, so that the ratio between specific heat at constant pressure and volume is constant.
- the transformation that carries the fluid from the high pressure zone to low pressure zone is a reversible process: $p \cdot V^{\gamma} = cost$.

Under these assumptions the work recoverable from the volumetric machine in the process of expansion it is observable in the Figure 3.8 and it can be calculated as:

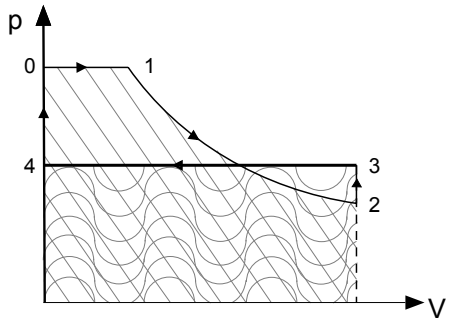

Figure 3.8: $p-V$diagram

$$L_c = \oint p\cdot dV = \int_0^1 p\cdot dV + \int_1^2 p\cdot dV + \int_3^4 p\cdot dV \tag{3.45}$$

The integrals from point 2 to 3 and from 4 to 0 are zero because they are integrals at constant volume. The others are:

$$\int_0^1 p\cdot dV = p_{su}\cdot V_{exp,sw} \tag{3.46}$$

$$\int_1^2 p\cdot dV = \frac{1}{\gamma-1}\cdot p_{su}\cdot V_{exp,sw}\cdot\left(1-\frac{V_{exp,sw}\cdot BVR\cdot p_{ad}}{V_{exp,sw}\cdot p_{su}}\right) \tag{3.47}$$

$$\int_3^4 p\cdot dV = -V_{exp,sw}\cdot p_{out} \tag{3.48}$$

Adding these three equations together the work per cycle is obtained:

$$\begin{aligned} L_c = {} & \tfrac{1}{\gamma-1}\cdot p_{su}\cdot V_{exp,sw}\cdot\left(1-\tfrac{V_{exp,sw}\cdot BVR\cdot p_{ad}}{V_{exp,sw}\cdot p_{su}}\right)+ \\ & +p_{su}\cdot V_{exp,sw}-p_{out}\cdot V_{exp,sw}\cdot BVR \end{aligned} \tag{3.49}$$

From the latest equation, simplifying and expressing everything through the BVR and the actual pressure ratio β, the following function can be extracted:

$$L_c = \frac{1}{\gamma - 1} \cdot p_{su} \cdot V_{exp,sw} \cdot \left(1 - BVR^{(1-\gamma)}\right) + p_{su} \cdot V_{exp,sw} \cdot \left(1 - \frac{BVR}{\beta}\right) \quad (3.50)$$

Compared to the isoentropic work under adapted conditions:

$$L_{c,is} = \frac{\gamma}{\gamma - 1} \cdot p_{su} \cdot V_{exp,sw} \cdot (1 - \beta^{\frac{(1-\gamma)}{\gamma}}) \quad (3.51)$$

the isoentropic efficiency can be defined:

$$\eta_{c,is} = \frac{L_c}{L_{c,is}} = \frac{\left(1 - BVR^{(1-\gamma)}\right) + (\gamma - 1) \cdot \left(1 - \frac{BVR}{\beta}\right)}{\gamma \cdot (1 - BVR^{(1-\gamma/\gamma)})} \quad (3.52)$$

The trend is shown in Figure 3.9. The example refers to an expansion of R123 that starts from 15 *bar* with a pressure ratio β up to 10. The scroll expander has a volume displacement of 80 cm^3/rev and an isoentropic exponent of 1.26 fixed for all the expansions. In Figure 3.9 there is also shown how the expansion changes with the variation of built in volume ratio (BVR) of the machine.
As it can be seen, the point where isoentropic efficiency is equal to one moves to the right as the BVR increases and this allows the scroll expander designer to exploit increasingly high expansion ratios. The trend of the graph indicates that under and over-expansion reduce the expander efficiency, and the decay in expander efficiency is less severe for values above the built-in volume ratio. This suggests that, the most interesting values are those at elevated β (the BVR parameter is fixed by the geometry of the machine), because over-expansion (resulting in recompression of the working fluid at the expander discharge port) is more detrimental than under-expansion, as noticed by several researchers as reported in the literature overviewed in Chapter one.
Since every thermodynamic processes that occur during expansion are known, it may be interesting to analyze which of these is responsible for the higher irreversibility, causing the deterioration in the machine performance.
In order to match this goal an exergy balance is conducted for each transformation. The exergy is a thermodynamic function that returns the maximum amount of energy that a system can provide when brought at thermodynamic equilibrium with the environment. Thus, the exergy depends on both the system and the environment. For this reason it is not a state variable, such

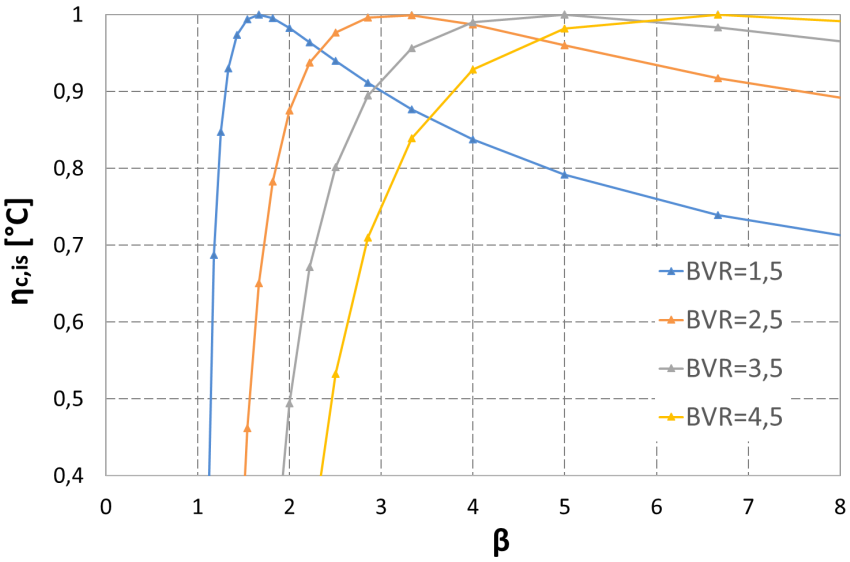

Figure 3.9: Expander efficiency of the ideal scroll machine under several BVR values.

as the enthalpy or the entropy. The introduction of the exergy is useful in complex energy systems to calculate the power lost by irreversibility without introducing the calculation of the generated entropy, which can sometimes be inconvenient and does not give an immediate response of the system/-component performance. For each transformation included in the expansion, the simplified exergy balance is defined as follows:

$$\mathring{m} \cdot (ex_{in} - ex_{out}) + \mathring{Q} \cdot \left(1 - \frac{T_{amb}}{T_k}\right) = \mathring{W}_{shaft} + \mathring{W}_{diss} \tag{3.53}$$

where the exergy fluxes refer to the thermodynamic states assumed by R123 at the inlet and the outlet of the transformation, the second term takes the heat transfers into account, if present, and evaluates the potential of the heat source to convert heat into work by means of the Carnot efficiency. T_k is the heat source temperature, considered to be constant.
The first term on the right of the equal sign is the power extracted from the process and the term $\mathring{W}_{diss}$ is the power lost due to the irreversibility of the process. Furthermore, the exergy efficiency of the component or of the whole scroll expander can be exploited:

$$\eta_{ex} = \frac{\mathring{W}_{shaft}}{\mathring{m} \cdot (ex_{in} - ex_{out}) + \mathring{Q} \cdot \left(1 - \frac{T_{amb}}{T_k}\right)} \tag{3.54}$$

where the denominator is the maximum power obtainable from the system while the numerator is the power actually extracted.
By comparison between the last efficiency indicator, (neglecting the heat sources), and the isoentropic efficiency, where the denominator involves a theoretical point with the same entropy at the inlet, the outlet point for the exergy efficiency is actually the expander outlet point from the real transformation, and then the irreversibility in the real expansion processes can be identified.
In a next chapter dealing with the performance analysis, some significant cases for which it is useful to analyze the power lost due to irreversible dissipation will be presented. This is made in order to see if these are mainly caused by the operating conditions or by the poor design of the scroll machine.

Chapter 4

Model implementation

In order to detect the sequence of the thermodynamic points of the expansion process, linked with all the equations presented before, the "*Exp_solver*" function was built up in Matlab environment.
This function needs a few inputs to operate and hereunder a description of all these input parameters is provided with further specifications:

1. p_{cond} $[kPa]$, the condensation pressure, which is equal to the expander outlet pressure p_{ex}, since no outlet pressure drop is included in this model;

2. $\mathring{m}_{ref,nom}$ $[^{kg}/_{s}]$, the nominal flow rate to discriminate the heat transfer at on-design and off-design conditions;

3. p_{su} $[kPa]$ and T_{su} $[°C]$, the pressure and temperature at the expander inlet respectively;

4. T_{amb} $[°C]$, the ambient temperature in order to correctly take into account the heat losses through the surroundings;

5. N $[rpm]$, the shaft speed of the expander;

6. $Exp - Par$, the vector containing all the expander characteristic parameters that must be identified by means of the calibration realized according to experimental data. They are:

    * A_{su} $[m^2]$, the cross-sectional area of the fictitious nozzle at the inlet;
    * $AU_{su,nom}$ and $AU_{ex,nom}$ $[^{W}/_{K}]$, the nominal overall heat transfer coefficients at suction and discharge respectively;

* C_{wall} [$W/K^{5/4}$], the constant considered in the heat exchange calculation between the external envelope and the surroundings;
* $V_{exp,sw}$ [m^3/rev], the displacement volume of the expander;
* BVR, the Built-in-volume ratio of the expander;
* A_{leak} [m^2], the cross-sectional area of the fictitious nozzle introduced for the simulation of leakage flow rate;
* a, the term in the function $(a + b \cdot \omega^n)$ which expresses the dependence of the friction loss by the speed;
* b, the term in the function $(a + b \cdot \omega^n)$ which expresses the dependence of the friction loss by the speed;
* n, the exponent in the function $(a + b \cdot \omega^n)$ which expresses the dependence of the friction loss by the speed;

7. $fluid$, the working fluid, i.e. R123, even though the Matlab function could run with any other fluid.

The "*Exp_solver*" is integrated with the NIST Fluid-prop implemented for the thermodynamic properties of the fluid. As an example, the density of the R123 can be obtained by introducing the pressure and temperature of a specified point in the Fluid-prop Matlab function:

$$\rho_x = refpropm('D','P', pvalue,'T', Tvalue, R123)$$

where the first variable inside the parenthesis is dedicated to the target function (D, stands for Density). Then in the second and fourth place there should be added the two properties for which the density is calculated, (p and T in this case). In the third and fifth space there are the values of the previous properties, and in the last space the working fluid has to be specified.
In Table 4.1 all the equations written in the modelling procedure are grouped to have a clear overview of the whole process of expansion. It can be noted in Table 4.1 that the resulting pressure downstream the fictitious nozzle at the inlet ($p_{su,1}$) is involved in the calculus of the entire mass flow rate $\mathring{m}$ entering the expander and it is not known a-priori. So the problem is iterative in $p_{su,1}$ and a first guess value has to be provided. In the same way even the temperature T_w is not known. It depends on many factors and acts as a closing variable for the energy balances on the control volume. At this point two more independent equations are required to derive these two unknown variables.

Table 4.1: Overall vision of the main equations adopted in the scroll expander model

equations	**unknowns**	**calculated**	**transformation**
$\mathring{m} = A_{su} \cdot \rho_{thr,su} \cdot \sqrt{2(h_{su} - h_{thr,su})}$ $h_{su,1} = h_{su}$	ρ,$h_{thr,su} = f(p_{su,1}, h_{su})$	$\mathring{m}$	$(su \rightarrow su, 1)$
$\mathring{Q}_{su} = \mathring{m} \cdot (h_{su,1} - h_{su,2}) = \left[1 - e^{(\frac{-AU_{su}}{\mathring{m} \cdot cp})}\right] \cdot \mathring{m} \cdot cp \cdot (T_{su,1} - T_w)$	$AU_{su,nom}; Tw$	$\rho_{su,2}, h_{su,2} = f(p_{su,1}, T_{su,2})$	$(su, 1 \rightarrow su, 2)$
$AU_{su} = AU_{su,nom} \cdot \left(\frac{\mathring{m}}{\mathring{m}_{nom}}\right)^{0,8}$	-	-	-
$\mathring{m}_{leak} = A_{leak} \cdot \rho_{thr,su} \cdot \sqrt{2(h_{su,2} - h_{thr,leak})}$	$h_{thr,leak} = f(p_{thr,leak})$	$\mathring{m}_{leak}$	$(su, 2 \rightarrow ex, 2)$
$p_{thr,leak} = MAX(p_{ex,2}; p_{crit,leak})$	-	-	-
$p_{crit,leak} = p_{su,2} \cdot \left[\left(\frac{2}{\gamma+1}\right)^{\left(\frac{\gamma}{\gamma-1}\right)}\right]$	-	-	-
$\frac{\rho_{ad}}{\rho_{su,2}} = \frac{1}{BVR}$	-	$h_{ad} = f(\rho_{ad}, s_{su,2})$	$(su, 2 \rightarrow ad)$
$h_{ex,2} = h_{ad} - \frac{(p_{ad} - p_{cond})}{\rho_{ad}}$	-	$h_{ex,2}$	-
$\mathring{m}_{leak} \cdot h_{su,2} + \mathring{m}_{in} \cdot h_{ex,2} = (\mathring{m}_{leak} + \mathring{m}_{in}) \cdot h_{ex,1}$	-	$T_{ex,1} = f(p_{cond}, h_{ex,1})$	$(ex, 2 \rightarrow ex, 1)$
$\mathring{Q}_{ex} = \mathring{m} \cdot (h_{ex,1} - h_{ex}) = \left[1 - e^{(\frac{-AU_{ex}}{\mathring{m} \cdot cp})}\right] \cdot \mathring{m} \cdot cp \cdot (T_{ex,1} - T_w)$	$AU_{ex,nom}; Tw$	h_{ex}	$(ex, 1 \rightarrow ex)$
$p_{me} = \rho_{ad} \cdot (h_{su,2} - h_{ex,2})$	-	-	-
$\omega_{loss} = (a + b \cdot N^n)$	-	.	-
$\mathring{P}_{loss} = p_{me} \cdot \omega_{loss} \cdot N$	-	-	-

The first of these is the continuity equation at the entrance of the scroll chamber, where the effective expansion occurs. Here the total mass flow rate splits into two paths as shown in Figure 3.1 where the su,2 thermodynamic point is reached. The effective mass flow rate goes through the positive scroll chambers where the shaft power can be extrapolated. This portion is proportional to the shaft speed N, the inlet density $\rho_{su,2}$ and the positive machine displacement $V_{exp,sw}$. The other leakage mass flow rate is bounded to the critical pressure at the throat of the convergent nozzle and is not useful for the production of work.
The second equation refers to the energy balance at the wall expander. In this model the temperature at the wall is supposed to be uniform and four energy fluxes are responsible for the maintenance of steady-state conditions. As it can be seen in Figure 3.1, they are, from the inlet to the outlet, the heat transfer at the suction, the power losses caused by friction, the heat transfer at the exit and finally the heat loss through the surroundings.
It is worthy of attention the fact that all the power fluxes have a well-defined direction, except the exit heat transfer which is dependent on the expansion ratio. In fact, if the pressure at the exit of constant volume process is very low, the temperature related to this pressure is low as well, so the heat exchange is inverted when this temperature is lower than T_w. Then, in order to assess the two unknown variables $p_{su,1}$ and T_w the following system must be solved in the model:

$$\begin{cases} \mathring{m} = \rho_{su,2} \cdot V_{exp,sw} \cdot N + \mathring{m}_{leak} = \mathring{m}_{in} + \mathring{m}_{leak} \\ \\ \mathring{Q}_{su} + \mathring{P}_{loss} - \mathring{Q}_{ex} - \mathring{Q}_{amb} = 0 \end{cases} \tag{4.1}$$

4.1 Calibration procedure

The calibration procedure provides for the identification of the model parameters mentioned above by minimizing a global error function accounting for the errors on the prediction of the mass flow rate, shaft power and exhaust temperature compared with the real values coming from the available experimental data. The error function is defined as:

$$
\begin{aligned}
error = \quad & \frac{1}{3}\cdot\left(\sqrt{\sum_{i}^{Ntest}\left(\frac{\mathring{m}_{sim}-\mathring{m}_{data}}{\mathring{m}_{data}}\right)^{2}}\right) \\
& +\frac{1}{3}\cdot\left(\sqrt{\sum_{i}^{Ntest}\left(\frac{\mathring{W}_{sh,sim}-\mathring{W}_{sh,data}}{\mathring{W}_{sh,data}}\right)^{2}}\right) \\
& +\frac{1}{3}\cdot\left(\sqrt{\sum_{i}^{Ntest}\left(\frac{T_{ex,sim}-T_{ex,data}}{T_{ex,data}}\right)^{2}}\right)
\end{aligned}
\tag{4.2}
$$

It was considered useful to give the same weight (1/3) to all the three variables calculated, since in an optical design of the whole ORC plant, all the quantities play a considerable role and the designer should be able to count on the accuracy of the calculated variables from the "*Exp_solver*" function. It should be noted that further quantities available from experimental data could be included in the error function in order to control the process of expansion, but these would be directly dependent from the three controlled quantities implemented in Eq. (4.2), and therefore would be useless.
In order to calibrate the expansion model the "*Optim_scroll*" function in Matlab environment was implemented. This function requires the insertion of a file that serves as real data input, in which there are both the quantities that are used to perform comparisons in the error function, and the quantities that actually serve as input for the "*Exp_solver*" function, such as T_{su},T_{evap}, T_{cond} and the rotating speed N.
Besides, the "*Optim_scroll*" uses the proper Matlab Optimization Toolbox function *"fmincon"* to find the model parameters that provide the minor system error, which results in attempts to find a constrained minimum of a scalar function of several variables starting at an initial guess value and return the final vector containing the optimal parameters. This is generally referred to as constrained nonlinear optimization or nonlinear programming. The syntax of the function is:

```
[yyy]=fmincon(@(xxx) errscroll(xxx,CATALOGO, fluido),
x0,[],[],[],[],LB,UB);
```

where the "*errscroll*" handle function deals with the calculation of the error provided in Eq. (4.2). The square brackets are options useless in this case and x0, LB and UB are the first guess vector, the lower and upper bound vectors that contain the initial, minimum and maximum values of the parameters respectively.
Some parameters of the first guess value were derived from preliminary observation of the experimental data. For Sure this analysis will not provide the final values of model parameters because as shown in section 2.1 regarding the test rig, the measuring sensors are positioned only at the entrance and at exit of the expander, while there is no information of the thermodynamic states inside the machine. Thus, it is assumed that the expansion is consumed in a single step, from input to output without taking into account all the transformations implemented in the model. Despite that, from this analysis it is expected to identify the order of magnitude of the final values, and these values fall in a neighborhood of the first guess ones. In particular, analysis can be conducted on:

- $V_{exp,sw}$, the volume displacement
- BVR, the built in volume ratio
- $AU_{su,nom}$, the nominal overall heat transfer suction coefficient
- $AU_{ex,nom}$, the nominal overall heat transfer discharge coefficient
- n, the coefficient as exponent in the power losses function

$V_{exp,sw}$, The volume displacement is a key parameter in the calibration of the model and its first guess value comes from the expression of the volumetric flow rate at the inlet of the expander, that is known by means of the thermodynamic quantities measured there. Beside the rotational speed is known as well, setting in order of increasing volumetric flow rate all the experimental points, the following equation can be formulated:

$$\mathring{V}_{in} = V_{exp,sw} \cdot N \tag{4.3}$$

Eq. (4.3) is valid for any point in the real data input file and the angular coefficient is the volume displacement $V_{exp,sw}$ that is in common with all of them. Employing a linear regression, the first guess value for this parameter can be derived (87 cm^3/rev).
BVR, The Built-In-Volume ratio is another important parameter to identify. Since this expander was modified from a scroll compressor originally used in a bus air conditioning system, some open-drive automotive air conditioning

scroll compressors catalog were reviewed to get an idea of which BVR could be appropriate for this case and a value of 3 was selected.
$AU_{su,nom}$ and $AU_{ex,nom}$, the nominal overall heat transfer coefficients of the suction and discharge, are very complicated parameters to define because neither the effective area of heat exchange nor the coefficient of convective heat exchange are known in the inner walls of the scroll machine. For this purpose, a in-depth experimental analysis and/or a computational thermo-fluid-dynamics (CFD) simulation on heat transfer phenomena inside the expander would be useful. Unfortunately, since the scroll expander technology for micro-scale ORC system is still in its preliminary stage, neither the experimental nor the CFD analysis are available.
Then, in order to assign a first guess value for the two parameters, a research on CFD scroll compressor simulation literature was conducted to investigate whether any physical energy transport phenomena could affect the amount of heat exchange and to have at least an order of magnitude of the convective heat exchange coefficient. Such a research led to discovery a study concerning the development of a CFD two dimensional model on the fluid flow and heat transfer in the working chamber of a scroll compressor with R134a as working fluid. In detail, K.T. Ooi et al. [36], with the aid of a CFD code, calculated the convective heat transfer using a standard k–ε turbulence model with a log-law wall function. The investigated compressor has a volume displacement of 64 cm^3/rev and a BVR of 2.7. The typical operating conditions include the intake gas temperature of 300 K at the peripheral port and the suction pressure from 0.1 to 0.35 MPa. In the study the wall temperature was taken as 330 K at a rotating speed from 1000 to 3000 rpm.
Results show that the momentum induced by the orbiting scroll forces the gas to bend towards the wall, so both the squish and the impingement cause a recirculating flow, whose strength increases with the rotation angle. Consequently, in the narrow flow domain, turbulence characteristics would have significant effect on the heat transfer. This led the authors to conclude that available empirical correlations with a lumped parameter approach are inadequate in predicting heat transfer within the scroll compressor chamber, due to the re-circulating flow, in particular, during the later period of the compression process.
The total spatial average heat transfer coefficients and surface average heat flux versus rotation angle at various operating conditions are presented in Figure 4.1. As it can be seen the spatial average heat transfer coefficients can reach peak values of 5000 $[W \cdot m^{-2} \cdot K^{-1}]$ towards the end of the compression process, when the fluid has gained the squish flow component. These numbers justify a surface average heat flux equally high, compared to a relatively small area of heat exchange that can be calculated from the geometric scroll

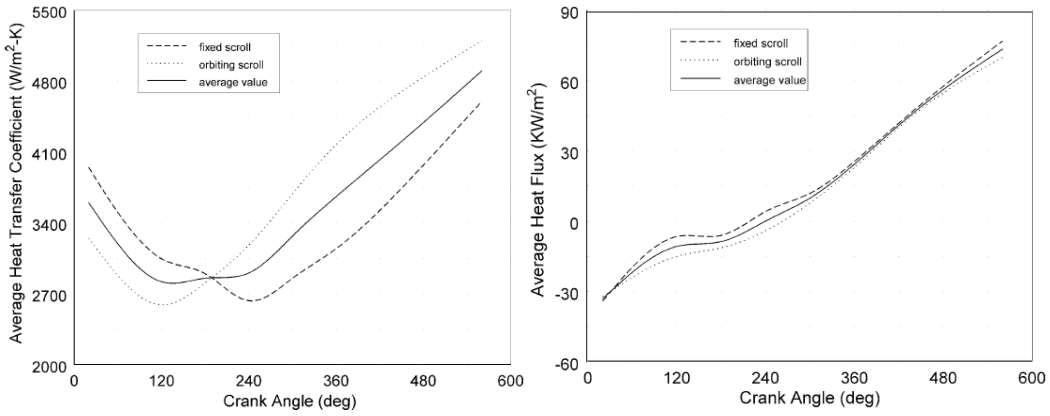

(a) (b)

Figure 4.1: Graphs of: (a)Average heat transfer coefficient variation and (b) Surface averaged heat flux variation vs crank angle; N= 3000 rpm, p_s = 0.35 MPa. [36]

compressor data available in the paper (about $3 \cdot 10^{-2} m^2$). So the nominal overall heat transfer coefficients can be calculated as well and the maximum value under these conditions is about 130 $[W \cdot K^{-1}]$.

In order to take advantage of the conclusions drawn from the paper by K.T. Ooi et al. [36] in favor of the expander analyzed in this thesis, an analogy was found and supported by means of two motivations. The first was the calculating of a ratio between thermophysical values under the same operating conditions of the Ooi's compressor for R134a and R123, to realize if, at least in terms of thermo-physical point of view, the analogy between the two working fluids in the compressor could hold. From the result of this relationship it arises that at least the minimum value of ratio does not fall below 0.9 in favor of the R123. Therefore slightly more elevated values of the convective heat transfer coefficient can be expected.

The second motivation comes from the fact that it is reasonable to think that even in the scroll expander, the significant motion due to squish is developed towards the end of the process, and this happens when the fluid has already crashed against the moving spiral walls many times. Thus a gradually increasing convective heat transfer coefficient is expected with the increasing of the rotation angle, even if at the same time the fluid density is decreasing. As for the ratio between the suction convective heat transfer coefficient and the discharge, further support comes from the work of Lemort et al. [16], which fixes high values for the two final nominal overall heat transfer coefficients as well. Finally, since the analyzed scroll expander is obtained from an air conditioning system of a bus, its size is more generous than for the

expanders studied in the literature, and therefore also slightly higher values of these two parameters can be expected. In this case, they were evaluated as 40 W/K for $AU_{su,nom}$ and 60 W/K for $AU_{ex,nom}$ as first guess values.
With regard to the exponent coefficient present in the mechanical power losses function n, a guess value equal to 1 is assumed because, by referring to the Stribeck theory, when the shaft expander runs beyond a certain limit, the lubrication becomes fully hydrodynamic, so the friction factor continuously increases, at least with a linear trend with the shaft speed.
All the other parameters that have not been mentioned were not initialized under particular hypotheses. They have only been identified as regards the order of magnitude that could lead to values known from very few works in the literature.

4.2 Results of the calibration and parameter sensitivity

In order to have an idea of how the minimization process works, reference to the flowchart in Figure 4.2 is made. As it can be observed, the model uses inputs and the initial parameters to calculate $\mathring{m}_{sim}$, $\mathring{W}_{sh,sim}$ and $T_{ex,sim}$ by means of the "*Exp_ solver*", which are the figures to understand if the parameters are good and the calibration is successful, by a comparison with the same output that come from experimental data, read from the data file with the real performance.
The function "*fmincon*" that was mentioned above tries to vary the calibration parameters to meet a threshold minimum error, which is formed by the three errors defined above and identified as epsilon in Figure 4.2. At the end of the calibration process, if the criterion is met, a function always written in Matlab environment saves the final parameters and other results of the simulation to be analyzed in post processing. After the calibration process has ended, the final parameters can be saved and analyzed.
As it can be noted in Table 4.2 for the parameters obtained from calibration, those for which guess values were justified, are placed in a neighborhood. Therefore it can be attested that these assumptions were valid for the present case. Compared to the 46 points available from the experimental campaign conducted by Zhang et al. [25], only 16 points were selected for calibration, (unlike some works that use all the points for the calibration, and so the validation is practically nonexistent), and these points come from those cases with greater mass flow rate values, to justify the employment of a scroll expander which has a generous displacement, and therefore able to process such a flow rates whose led higher shaft power. The other points were used

Table 4.2: Model final parameters

A_{su} $[mm^2]$	$AU_{su,nom}$ $[W/K]$	$AU_{ex,nom}$ $[W/K]$	C_{wall} $[W/K^{5/4}]$	$V_{exp,sw}$ $[cm^3/rev]$
97.4	50	110	2.2	94.1

BVR [-]	A_{leak} $[mm^2]$	a $[N\cdot m]$	b $[N\cdot m/s^{1.83}]$	n [-]
2.83	8.5	$3.4\cdot 10^{-3}$	$1\cdot 10^{-3}$	1.83

in the validation process.

It is worthy of attention at this point the sensitivity analysis of these parameters on the behavior of the model, to see how the error increases when varying the parameters one by one, with respect to the calibration value. In Figure 4.3 the trend of this error is shown by varying the parameters of $\pm$ 5% compared to their nominal value. It can be seen that not all the parameters but only those that provide a significant discrepancy

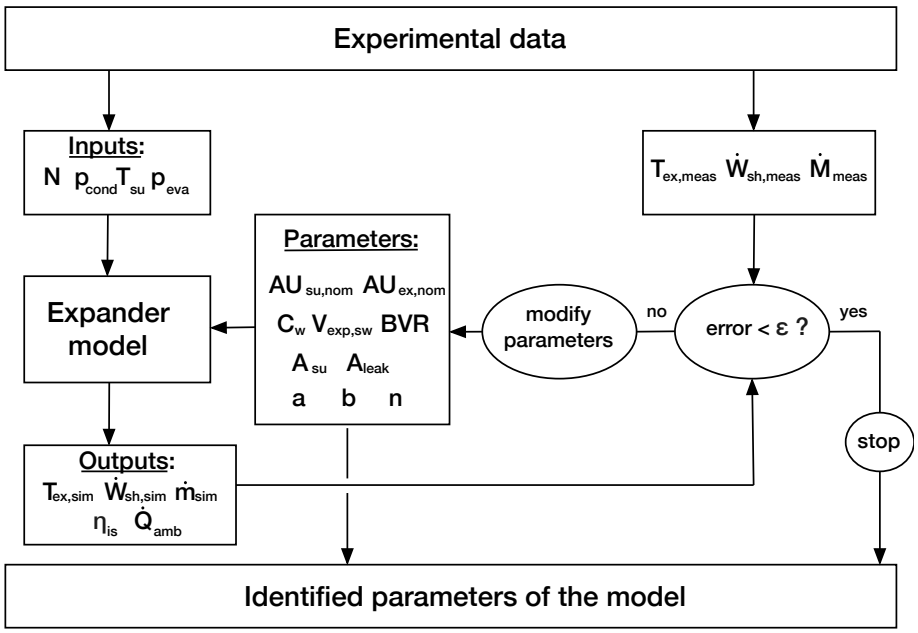

Figure 4.2: Flow chart of the parameter identification process.

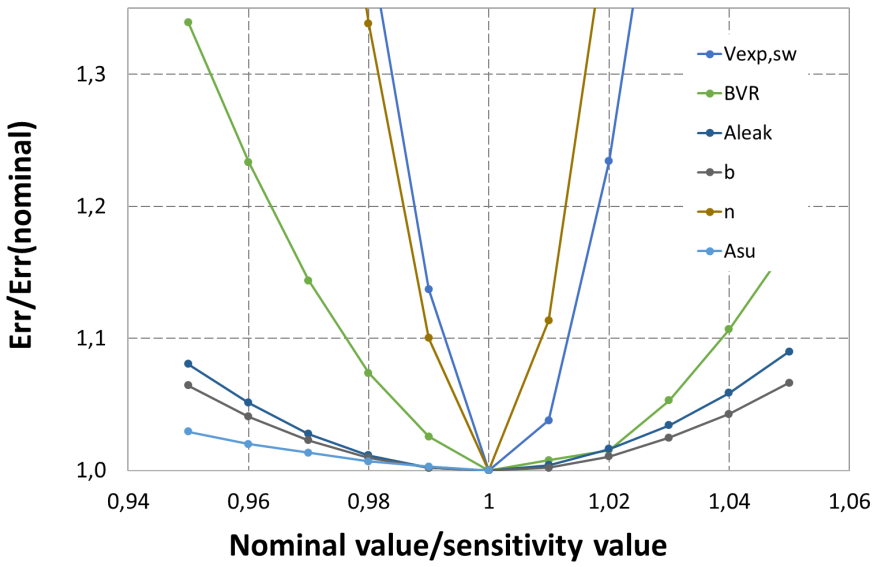

Figure 4.3: Sensitivity of the "*Exp_solver*" parameters

from the optimal solution are reported. In fact, the parameters $AU_{su,nom}$, $AU_{su,ex}$ and C_{wall} are not present, because even with a change of $\pm$ 5% from their nominal value, they do not appreciably affect the response of the model of more than 1%. The parameter A_{su} is represented only in the left side of the graph as it represents the throttling through the simply convergent nozzle. And it is clear that if this is reduced, the supply pressure drop increases and consequently reduces the mass flow rate, which is one of the three results that the "*Exp_solver*" Matlab function returns and it is directly involved in the calculation of the error.
On the other hand, the increase of the parameter A_{su} is equivalent to strongly reduce the pressure drop and then an enlargement of the throat of the convergent nozzle does not lead to substantial modification of the solution. As for the other parameters, they greatly affect both the thermophysical properties and the performance of the expansion process, therefore they affect the solution of the model both in the left and in the right side of the graph in Figure 4.3.
As it can be seen, the three parameters that most significantly influence the error are the BVR, the volume displacement and the exponent coefficient which is directly connected to the calculation of the mechanical power loss. This conclusion is fully consistent with the analysis carried out by Cuevas et al. [37] where high sensitivity was found with reference to the displacement volume and to the BVR value.

Chapter 5

Model validation

The validation procedure allows to verify the capability of the expander model to predict the machine behavior, in particular in those experimental points that were not used for calibration. By reviewing the works on scroll expanders in the literature, almost all the machines have a modest displacement volume, which results in a limited mass flow rate. This feature reflects on the corresponding power transferred to the shaft: despite the expansion ratios are quite high, power rarely exceeds a thousand watts. However, the behavior of the scroll expander by Zheng et al.[25], is quite different. In fact, since the machine is derived from a compressor used in the air conditioning system of a bus, the dimensions are more generous, and the displacement is increased, with higher mass flow rate processed. From this point of view, the expander of Zheng et al.[25] is most similar to the new generation scroll machines suitably designed to work as expanders, as seen in Chapter 1, built by Air Squared company, since they have designed machines with displacements larger than those present in the literature as well.
Based on the possibility to operate the machine at high flow rates, it was decided to choose the experimental points of the case with the heat source at 160 $°C$ as calibration points, i.e. those at higher mass flow rates.
The reason that led to choose these points is justifiable from both an economic point of view and the overall dimensions. In fact, as can be seen from Figure 2.2, the assembled plant is quite voluminous, and the maximum obtainable power is required, in order to justify the economic effort for the whole plant. Not all the points with the higher mass flow rates were chosen for calibration. Some points have been excluded: the first points set from 10 to 13 Hz series, because they show the lower shaft torque and the torque transducer has an accuracy of 0.5% of full scale, i.e. is 0.5 Nm. This uncertainty accounts for about 10% for these points.
Accordingly, these points have been eliminated from the calibration process,

to obtain a calibration as clean as possible by measurement uncertainties. As previously mentioned, after calibration, the validation was performed on all the other points available from the experimental campaign less than those that showed presence of the liquid phase at the entrance of the expander, for which thermodynamic properties cannot be clearly defined, for the lack of quality informations. The results of the model validation are presented in the following sections.

5.1 Validation process

Figure 5.2 shows the deviation of the quantities simulated from those derived from the experimental analysis. These quantities are the outputs of the *"Exp_solver"*, i.e. the mass flow rate, the shaft power and the outlet temperature. The points used for calibration are marked with a blue square, while those used for validation with a red dot.
As it can be seen in Figure 5.2 the points used for calibration are simulated obviously more accurately than the others. Hereunder the maximum outputs deviation can be observed for both calibration and validation points:

Outputs	Calibration	Validation
$\mathring{m}$ $[g/s]$	± 2 %	$\pm 5\%$
$\mathring{W}_{sh}$ $[W]$	± 3.5 %	$\pm 7\%$
T $[K]$	± 1.5	± 2.5

Should be pointed out with reference to Figure 5.2 that only one point breaks the barrier of 7% (standing at 11% for the shaft power), while all other points fall inside. It is necessary to remark that these points where the simulation error is higher belong to the the second points of each series, where the measurement uncertainty about the torque is still high, and then this uncertainty is transferred to the shaft power. Thus, it would not be correct to assign the entirely error of prediction on the model.
As a basis of comparison on the obtained results a work regarding the characterization of a scroll expander operating with air and ammonia performed by Mendoza et al. [38] is reported. Even in this case a semi-empirical model is proposed to determine the scroll expander performance. In Figure 5.1 can be seen the symmetric interval of the deviations between the simulated quantities and experimental data which are $\pm 5\%$, $\pm 9\%$ and ± 4 K for the mass flow rate, the shaft power and the outlet temperature respectively. Despite

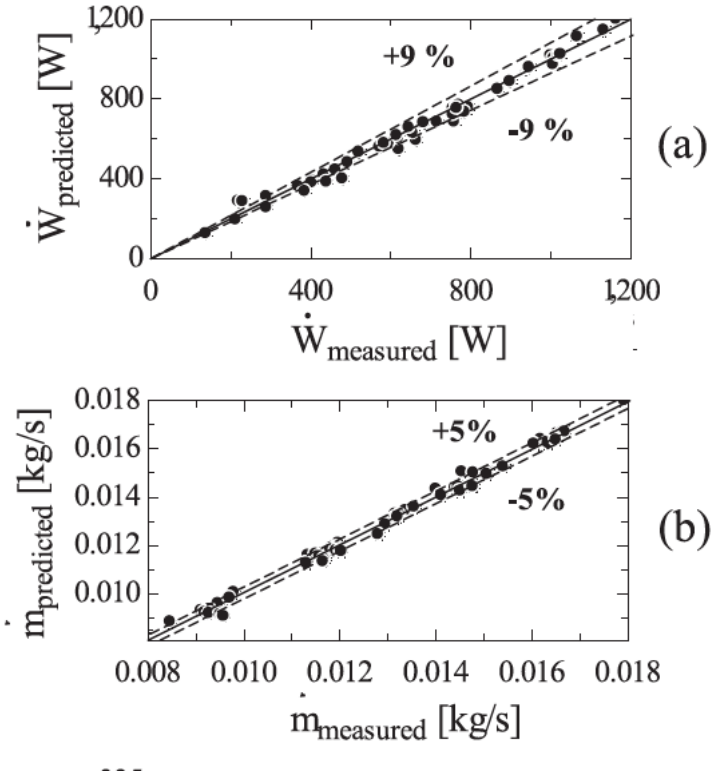

Figure 5.1: Comparison results on the model accuracy about: a) mass flow rate and b) shaft power proposed by Mendoza et al. [38]

many simulated points belong to these intervals, it is possible to observe that many others points fall off the borders without the possibility to identify their deviation accurately. From the comparison between the results obtained in this thesis work and those of Mendoza, and in the light of the considerations drawn, it is believed that these results can be considered satisfactory and the numerical investigation of the scroll expander performance can take place.

5.2 Analysis of the simulated performance

After validating the expander model, the parameters of the model can be considered fixed, and it is therefore possible to carry out any investigation on the whole expander operation range, especially for those conditions that are most interesting for the mechanical power production.
First of all it is useful to see the degree of relevance of the terms that appear in the equation of the energy conservation on the control volume of the expander. As expected, the heat lost to the environment caused by the

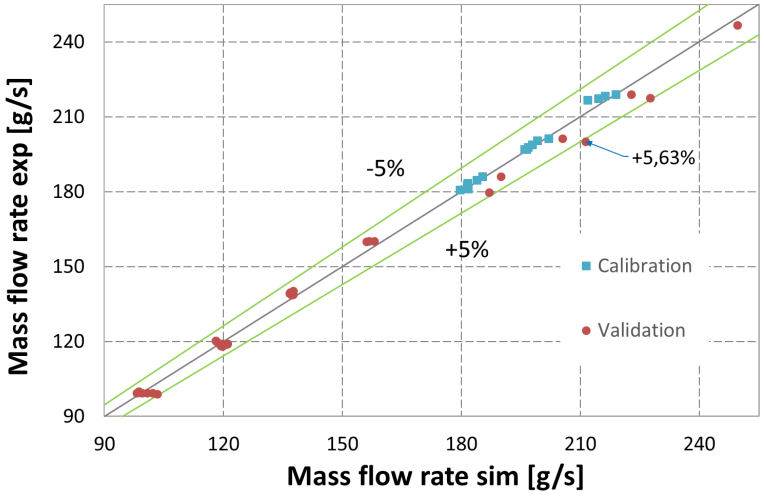

(a)

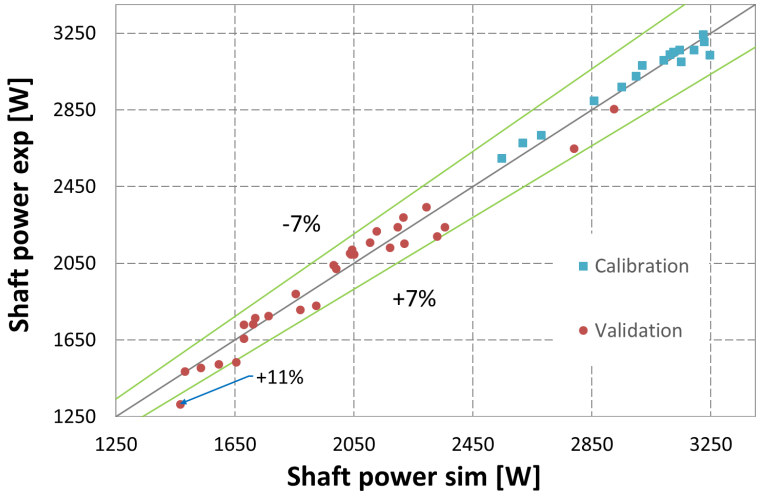

(b)

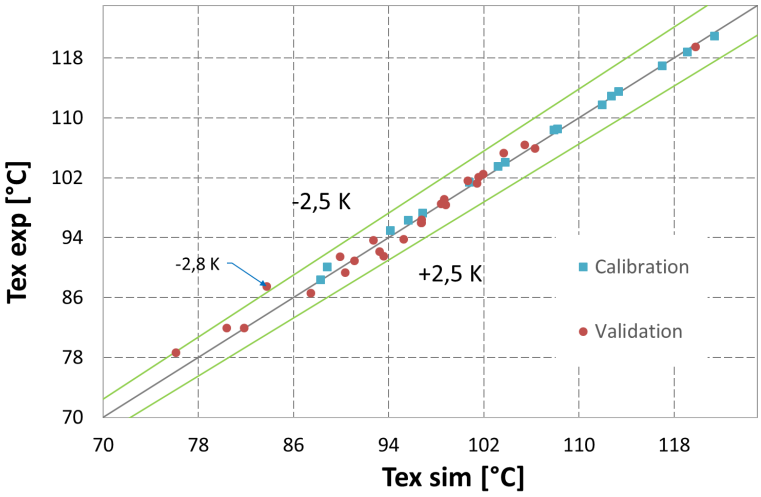

(c)

Figure 5.2: Simulated vs experimental quantities of (a) mass flow rate, (b) shaft power and (c) discharge temperature.

high temperature of the metal is not negligible, and is direct responsible for the difference that Zhang et al. [25] did not justify, based on the power calculated accounting to the enthalpy drop from inlet to outlet, and the shaft power obtained by means of the AC dynamometer unit. In the light of this fact, the scroll expander can not be considered an adiabatic machine, and measures to limit the thermal dispersion must be taken.
In order to get an idea of the extension of this phenomenon on the powers involved, Figure 5.3 shows model outputs with regard to the power calculated as $\mathring{m} \cdot \Delta h$ and the measured one. Both the case with reduced mass flow rates and 140 $°C$ as heat source, and the case with high flow rates and 160 $°C$ as heat source are presented. These graphs are practically identical to the same graphics deducted from the experimental campaign analyzed in Chapter 2, so it can be sure that the physics of the problem has been caught.

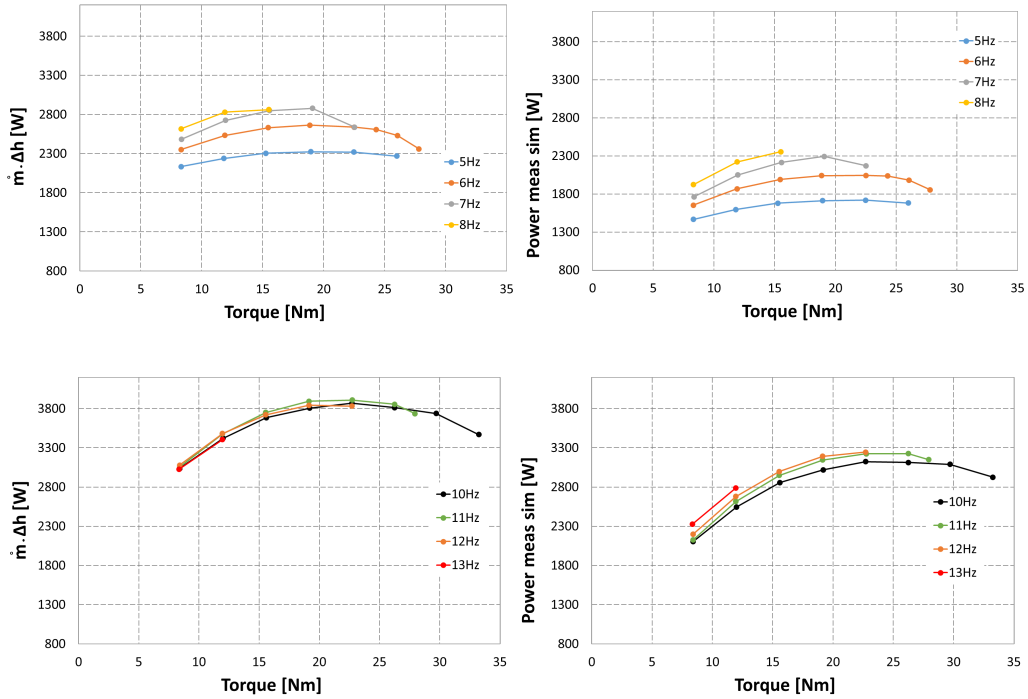

Figure 5.3: $\mathring{m} \cdot \triangle h$ and shaft power measured as results of the simulations.

Figure 5.4 shows the heat loss for all the points of the experimental campaign as an absolute value and divided by the $\mathring{m} \cdot \Delta h$. As can be seen, the thermal power lost to the environment can be comparable with the nominal power of the machine. In fact for higher flow rates this power touches peaks of 32% of the $\mathring{m} \cdot \Delta h$, and does not fall below 18% in any operative condition. Thus, a thorough investigation on the operating conditions of the scroll expander

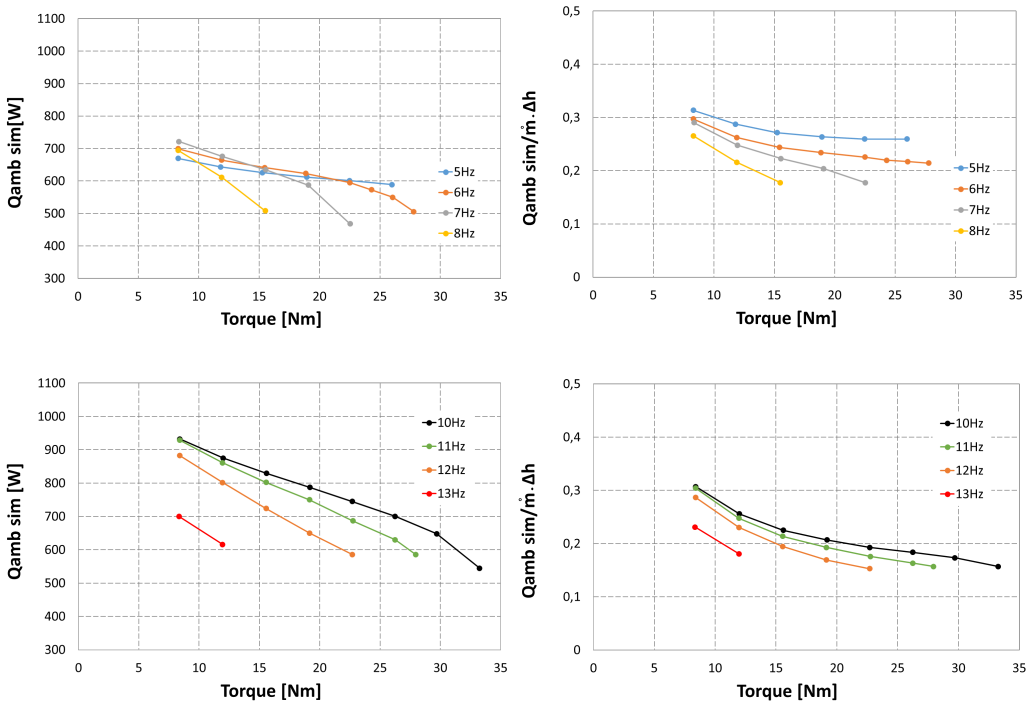

Figure 5.4: Ambient heat loss and ratio between the latter and $\mathring{m} \cdot \Delta h$ as results of the simulations.

should be conducted, especially focusing on the thermodynamics of the state entering the expander, which could fix the thermal level from which the expander starts losing heat to the surroundings.

Chapter 6

Performance analysis

This chapter deals with the core of the thesis work, as the performance of the scroll expander will be investigated referring to those operating conditions worthy of note, by varying the operation parameters. As already mentioned in the Introduction, this machine is able to convert a low temperature heat source into work, which originates for example from an internal combustion engine flue gas, or from the heat transfer fluid passing through a concentration solar field. The difference between these two sources has some relevance for the performance of the expander.
Generally speaking, it can be said, that if the source is a waste process, it will be cheaper to convert the maximum possible work from the source, shifting the emphasis from the efficiency of the process. Otherwise if a dedicated source is employed to extract electric energy by means of the scroll expander, as in the case of the solar field, converting the heat source with a higher efficiency at the expense of power may mean the installation of a smaller number of panels and therefore a lower cost of the entire plant.
In the latter case, the designer needs to look for a trade-off situation between the electric power obtainable from the generator, and the conversion efficiency of the machine. So maximizing a single output would not be correct as starting point. In any case, with the model developed here, the designer has the full overview of the problem, and then he can pursue its project goal.

6.1 Sensitive parameters

The presentation of the performance is designed to study a single parameter by varying it in a significant range, and keeping all the others fixed. Furthermore, with the goal of having continuously a visual comparison between the various machine operating conditions, up to four cases are shown in the same graph simultaneously, in which two other characteristic parameters are

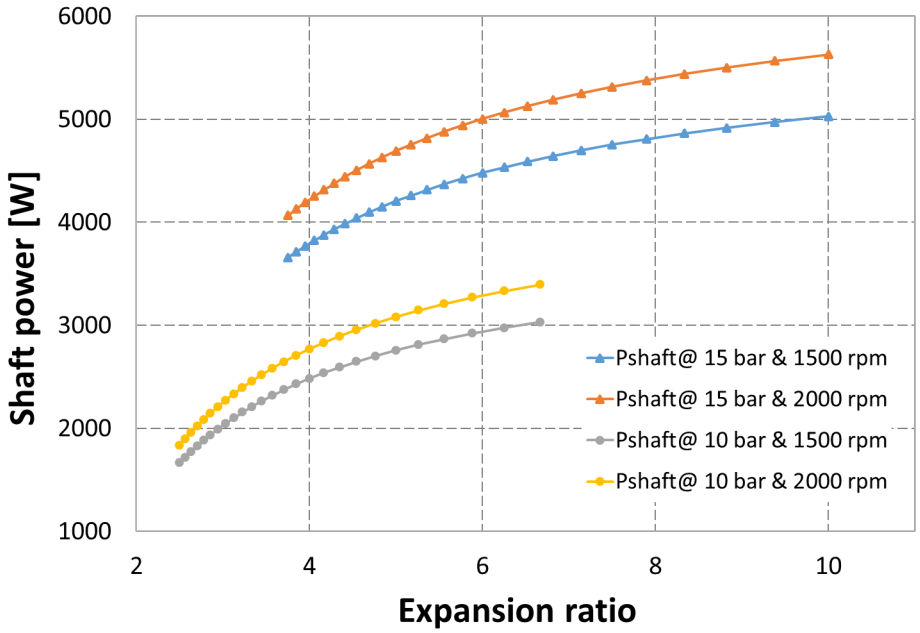

Figure 6.1: Shaft power vs expansion rate for four cases

varied by steps, while the one under investigation is varied continuously. The monitored parameters are the barometric expansion ratio (β), defined by the ratio between the evaporation and condensation pressure of the micro-ORC facility in which the scroll expander would be employed, the shaft speed and the superheating temperature. The control outputs to identify the sensitivity of the parameters are mainly the mass flow rate, the shaft power, the machine efficiency and the heat lost through the surroundings.

6.1.1 Influence of the expansion ratio

With reference to Figure 6.1, the shaft power is simulated by varying the expansion ratio. Considering two inlet pressures of 10 and 15 *bar* , a fixed inlet temperature of 160 $°C$, (which means a ΔT of superheating of 48.9 and 28.5 $°C$ respectively), at 1500 and 2000 *rpm* of shaft speed and the condensing pressure varies from a maximum of 4 to a minimum of 1.5 *bar*, for which it has a saturation temperature of about 40 $°C$, representing the lower limit of the discharge pressure for which condensing the two-phase fluid is possible, without oversizing the condenser.
It can be appreciated that the power always increases with the drop of condensation pressure, i.e. it increases with β. As we have seen from the Figure 3.3, the area subtended by the cycle in the $p - V$ diagram always increases

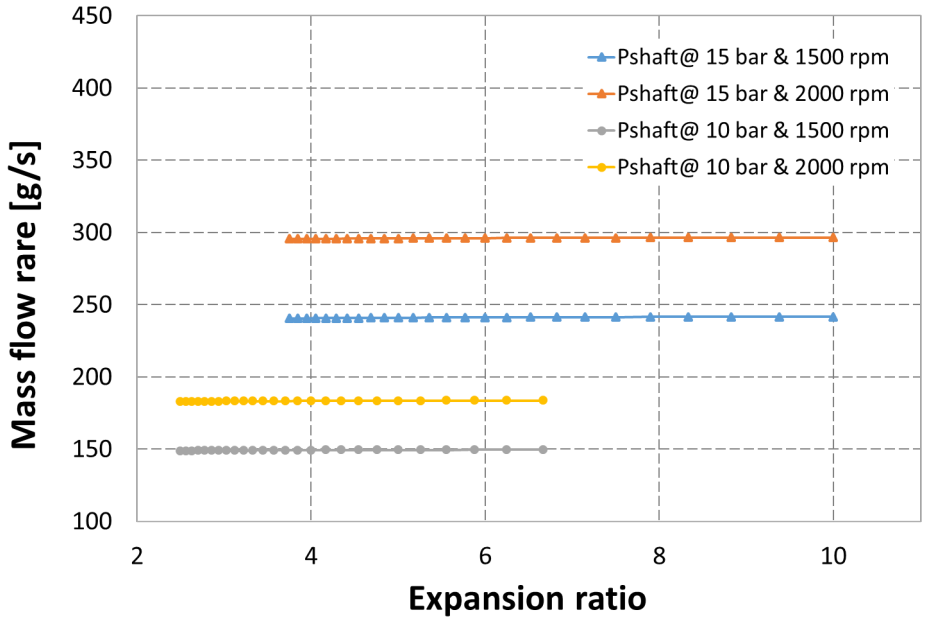

Figure 6.2: Mass flow rate vs expansion rate for four cases

even if the discharge pressure does not correspond to that of adapted conditions. From Figure 6.1 it can be seen that reducing the shaft speed, the power curve is shifted downwards, since the mass flow rate is reduced with all other conditions fixed, as can be seen in Figure 6.2, where the mass flow rate is plotted for the four cases.
Instead, when the pressure at the entrance is reduced up to 10 bar, the power curve is also translated towards the left in addition to being shifted down, corresponding to the cases with increased expansion ratio. This is caused by the fact that the extraction of work occurs at lower pressure and, at the same temperature, with lower enthalpy. In addition, being fixed the condensing pressures, even the β falls in a lower range of values compared to the case with the pressure inlet equal to 15 bar.

Also for this case the same trend of the power curve resulting from a step change in the shaft speed is noted. Besides it can be seen in Figure 6.2 as a reduction in the inlet pressure causes a decrement of the mass flow rate processed by the scroll expander. Indeed, in addition to the decrease of the flow rate caused by the reduction of the shaft speed, the two cases with 10 bar as inlet pressure have flow rate values lower than the cases with inlet pressure at 15 bar, because, in the latter case, higher pressure means higher density.
For a full discussion Figure 6.3 shows the trend of the machine efficiency as

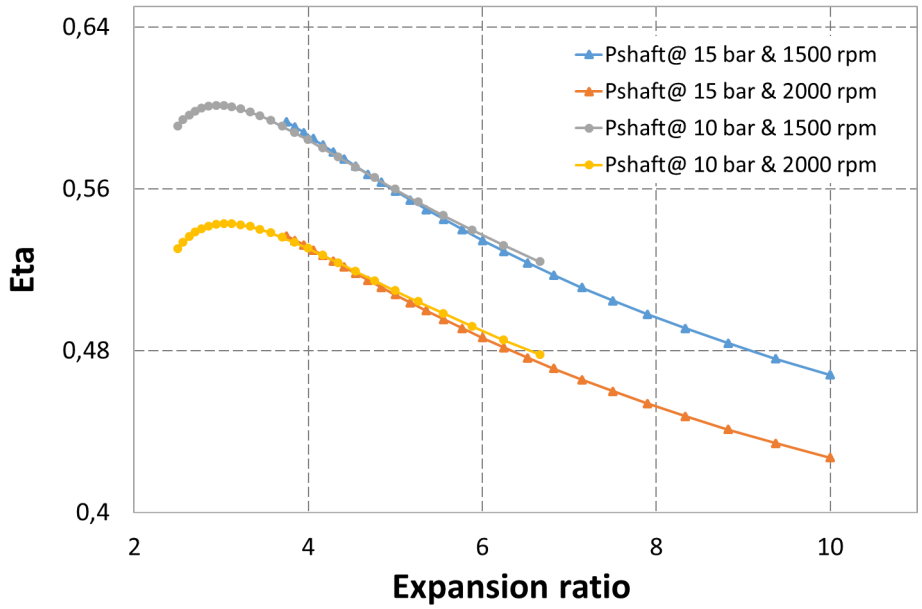

Figure 6.3: Machine efficiency vs expansion rate for four cases

defined in Eq. (3.44). Not surprisingly, it can be noted, as in the case at inlet pressure of 10 *bar* and for the condensing pressures considered, the efficiency curve presents a maximum, as the condensing pressure passes clearly through the adapted condition of the machine, which as seen in Chapter 3, (at least in the ideal case) provides the highest efficiency.
In the case of inlet pressure equal to 15 *bar*, it is noted that the expansion ratio is high even with the maximum condensing pressure, equal to 4, and then all the lower pressures lead the machine to work in conditions of under-expansion. Due to this fact, Figure 6.3 shows the decreasing efficient phase only, which assigns the extraction of work at the isovolumic transformation at the exit chamber of the scroll expander, which, as discussed above, is not the most efficient process to match that goal, and then performance coefficient expires. Contrary to what seen for the power curve, the increase in the shaft speed determines an important deterioration in expansion efficiency, which is caused by the heavy power lost in friction, which increases almost quadratically with the shaft speed.

6.1.2 Influence of the shaft speed

In Figure 6.4 four cases are presented to analyze the sensitivity of the shaft speed on the net power of the scroll expander. All the fixed parameters are

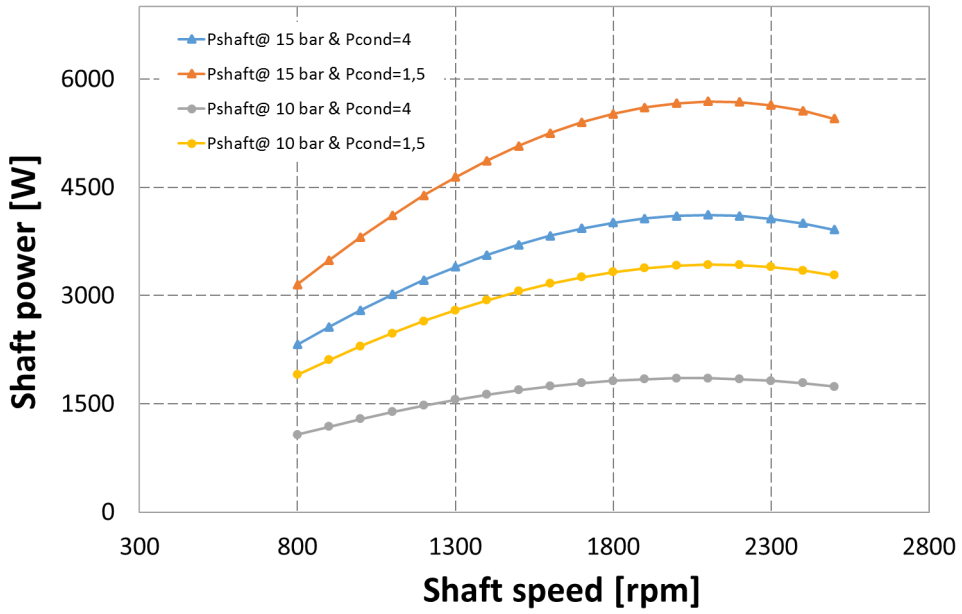

Figure 6.4: Shaft power vs shaft speed for four cases

the inlet pressure, at 10 and 15 *bar*, the condensation pressure, at 4 and 1.5 *bar*, while the temperature at the inlet is set for both input pressures at the evaporation temperature plus 8 K. In this way there is the certainty that none of the thermodynamic points falls into the saturation bell-shaped curve.
The tendency to avoid at all costs the entrance in the saturation curve is not linked with possible damages that the expander may suffer. In fact, in volumetric machines such as scroll expanders the speeds of the crossing flow are at least an order of magnitude smaller than the velocities characteristic in turbomachine. Then the droplets of liquid that would be transported by the flow do not damage the internal walls of the machine, and a certain amount of liquid will behave as a lubricant between the spirals in contact, and consequently reduces the leakage flow, improving the filling factor of the machine. The reason why two-phase states have not been considered in the expansion model is that experimental campaign of Zhang et al. [25] stopped in those points that showed clear signs of entrance into the saturation curve, so physically there was not a database of points with these characteristics on which a calibration could be carried out. Consequently, the attention is focused only in the superheated region only.

Returning to Figure 6.4, it can be noted that the power always presents a maximum value by varying the shaft speed. In fact, beyond a certain point,

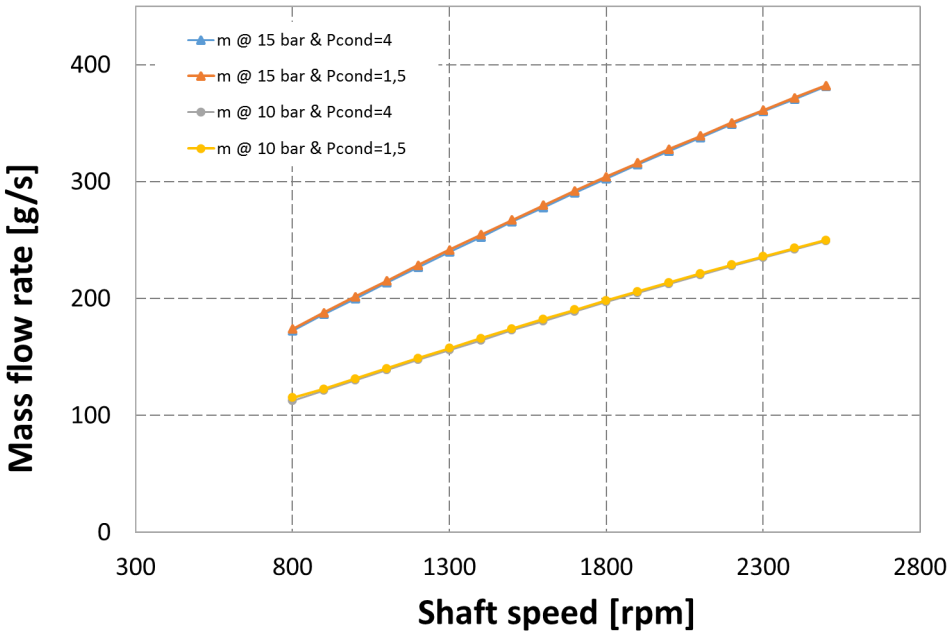

Figure 6.5: Mass flow rate vs shaft speed for four cases

the increase in mass flow rate given by increasing the revolution speed is no longer sufficient to counteract the power losses due to friction between the metal strips. The range beyond this maximum is no more interesting because it would mean reducing the power extracted from the machine by increasing losses rather than reduce them, bringing down the efficiency of the expansion process. Besides it turns out what previously observed, that the power increases when the expansion ratio raises, and is shifted down when the work extraction begins at a lower inlet pressure value. The variation in mass flow rate is reported in Figure 6.5.
As said before, its trend is ever increasing with the shaft speed, in an almost linear manner. As can be seen, the curves are superimposed for the respective inlet pressures at 10 and 15 *bar*. Although one could think that a higher expansion ratio results in an increase of leakage flow rate, this is not happening here. In fact, the reason why in the curves at different expansion ratio of Figure 6.5 have no deviation is given by the fact that also the smallest expansion ratio of this range, which occurs at the input pressure equal to 10 *bar* and with the output pressure equal to 4 *bar*, the vapor is already in the so-called chocking conditions. It is clear, therefore, that for each subsequent increase in the expansion ratio, this leakage flow is proportional to the inlet pressure and the curves are superimposed.
It is interesting to see now the trend of power losses caused by friction that

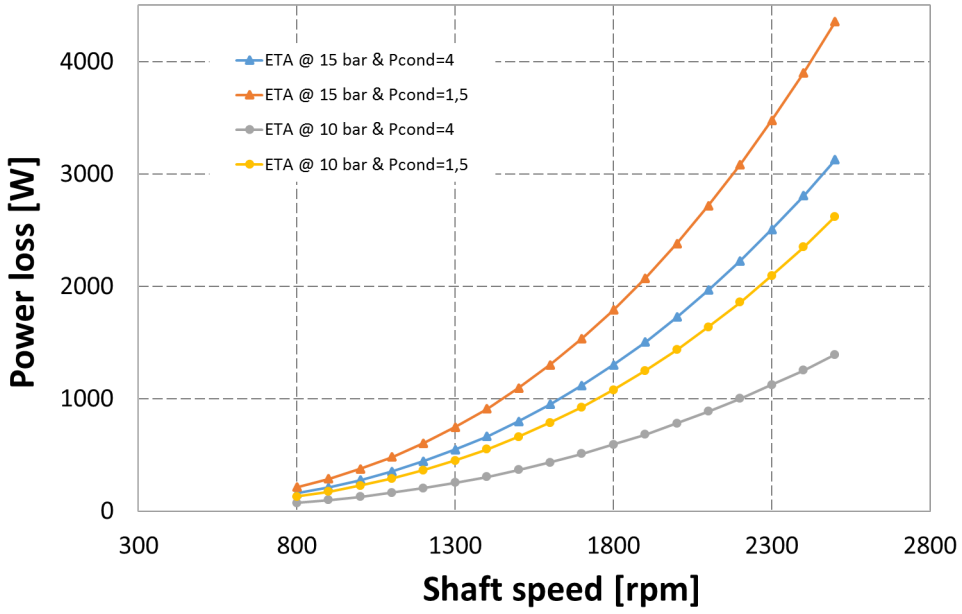

Figure 6.6: Power loss vs shaft speed for the four cases

afflict the output of the scroll expander so much.
As explained in Chapter 3, the friction factor increases a little more than linearly when the flow regime of the lubricating oil is "fully lubricated", from the Stribek's theory. In Figure 6.6 the curves of power loss are shown at different shaft speed, based on the product between the friction factor and the angular velocity of the machine. It can be seen how the curves grow up sharply with increasing revolution speed and this effect is amplified for the cases with higher expansion ratios. This trend is justified by the fact that the model of the power losses contemplates the introduction of the so-called mean effective pressure, in analogy with internal combustion engines (ICE). In fact it is noted that the higher the pressure difference, the stronger the two spirals of the expander are crushed against each other. This increases the friction factor, which is then important for both high shaft speed and high expansion ratios.

As can be noted from the energy balance on the metal wall of the scroll expander (which is the second equation of the system in 4.1), the power lost by the friction is not simply removed from the gross power, but it is re-injected as a power flow to this energy balance, with the idea that it can provide a kind of recovery work, for the working fluid in the expansion chambers. On the other hand, this same power flux always entering with a positive sign into the wall, and is one of the main players affecting the determination of

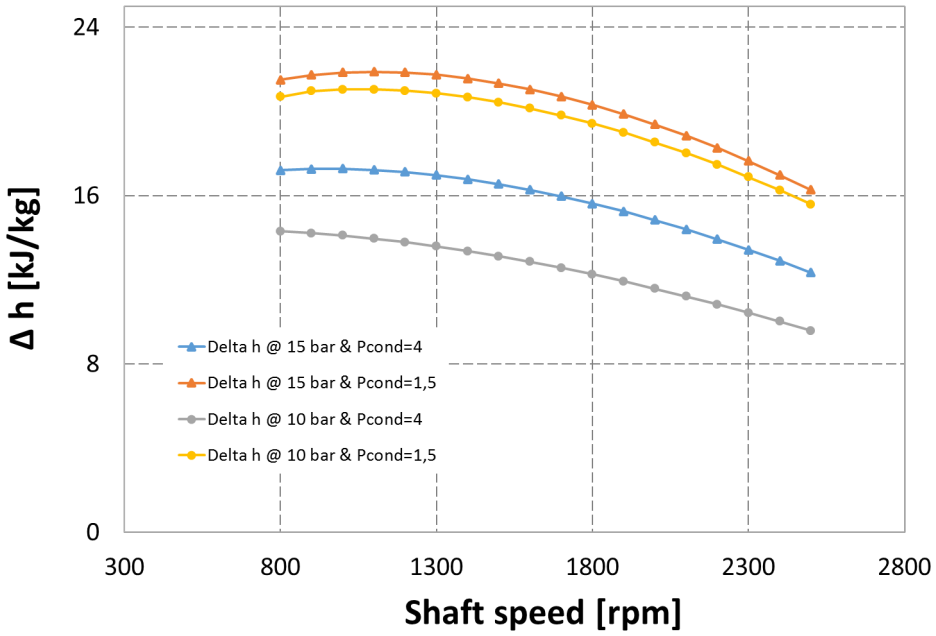

Figure 6.7: $\triangle h$ vs shaft speed for four cases

the isothermal wall temperature, which guide the heat exchange with the surroundings. That term takes on a more significant weight when the power losses are relevant.
To have an idea of where this power loss is discharged once introduced in the energy balance, main input/output that appear in the equations are monitored. They are the temperature of the point after inlet cooling $T_{su,2}$, the wall temperature T_w, the mass flow rate $\mathring{m}$ and the outlet temperature after the outlet heat transfer T_{ex}. The result was that the wall temperature has risen by about 18 K in the case at maximum rotation speed, which means that the temperature of the fluid at the exit of the cooling process was higher, and so was the enthalpy at the point from which starts the extraction of useful work. In this case the gain is well exploited by the fact that the flow rate also increases with the shaft speed and thus the recovery work is effective.
On the other hand, the increasing of the wall temperature means the growth of the heat losses towards the environment and the temperature at the outlet of the expander, which assigns to the condenser a heavier heat duty, which weights in terms of overall cycle efficiency. Figure 6.7 shows that the enthalpy drop through the machine is reduced with the increasing of the shaft speed, leading to an increase in power lost by friction, which is discharged to the fluid at the output.
To have an idea of how the phenomena related to the increase in the shaft

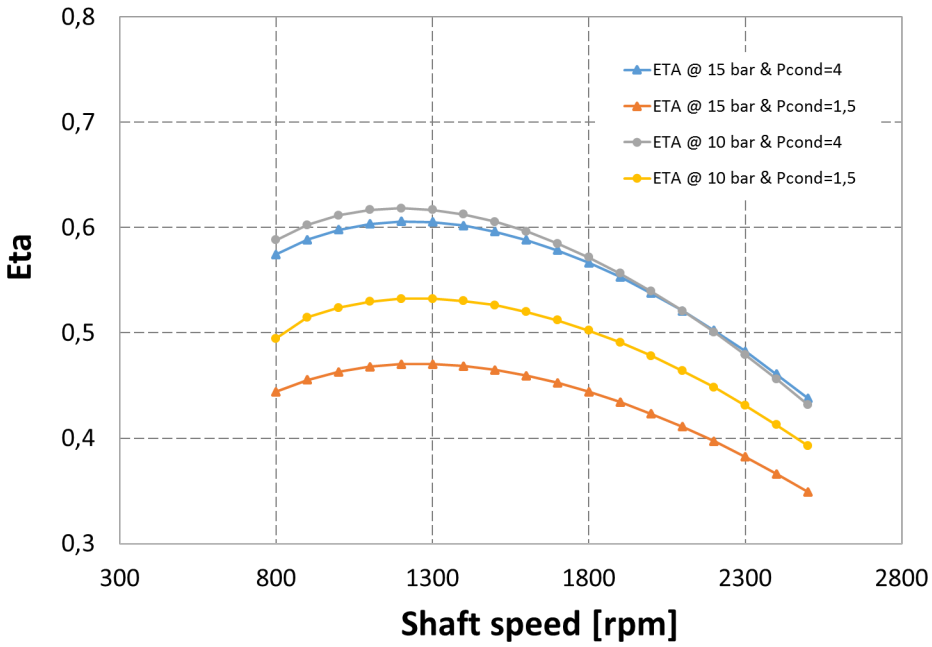

Figure 6.8: Machine efficiency vs shaft speed for four cases

speed affect the expansion process, Figure 6.8 shows the behavior of the machine efficiency as defined in Eq. (3.44), by varying the shaft speed, as pointed out for the expansion ratio in section 6.1.1. As it can be seen, the curves show a maximum at a certain shaft speed that does not match with the one that maximizes the mechanical power.
Once again it is stressed out how the chase of the peak of a function may lead to adverse results compared to another function, and then actions taken to set the operational points must be previously examined according to the targets. Figure 6.8 also shows that the highest performance curves are those at lowest expansion ratio, according to the theory of ideal transformation included in chapter 3, as β is close to the adapted expansion ratio. For other cases, with higher β values, it can be seen how the increase of the friction factor led to a greater mean sliding pressure of the spirals that is very disadvantageous, since it drags down the efficiency curve.

6.1.3 Influence of the superheating

The behavior of the expander at different inlet temperatures will be analyzed in this subsection. This temperature reflects the degree of superheat supplied to the fluid. The fixed conditions of the analysis are the usual, i.e. the input pressure of 10 and 15 *bar*, outlet pressure no less than 1.5 *bar*, and shaft speed

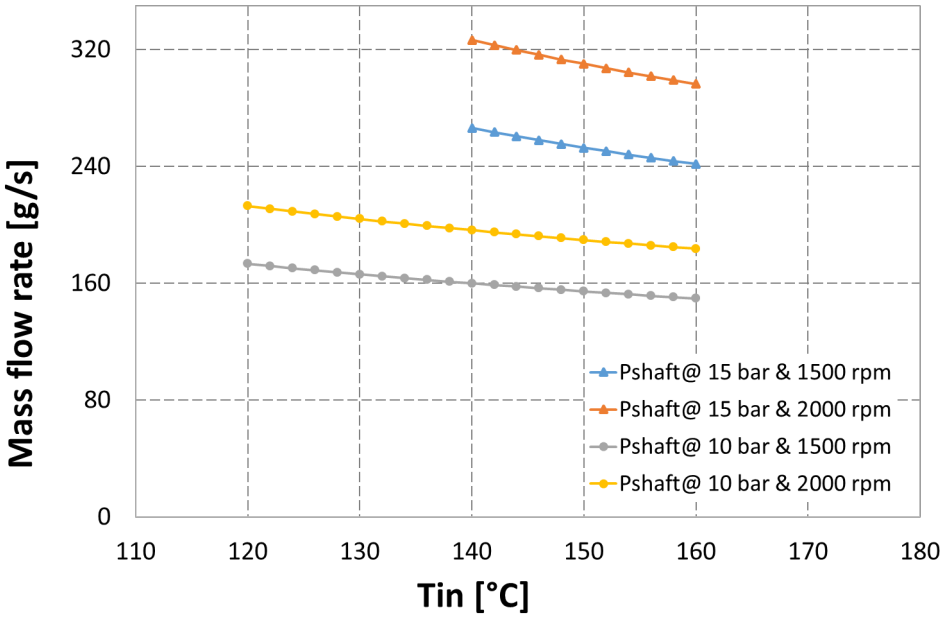

Figure 6.9: Mass flow rate vs inlet temperature for four cases

of 1500 and 2000 rpm. The inlet temperature is varied for all cases from 160 $°C$ down to the evaporation temperature corresponding to its pressure plus 8 K, due to the fact that in this way no thermodynamic point of expansion is placed in two-phase state. It is therefore clear that cases with evaporation pressure of 10 bar, which has a saturation temperature of 111.15 $°C$, cover a higher temperature range compared to the case with evaporation pressure of 15 bar, with has a saturation temperature of 131.5 $°C$. With reference to Figure 6.9, one can observe the trend of the mass flow rate when the superheating temperature increases.

It is seen that the mass flow rate decreases slightly, since the density decreases despite of a constant pressure heating of the fluid. As it is reasonable, the mass flow rate is high for both higher shaft speed and higher expansion ratio.

If Figure 6.10 is observed, one can realize that the power of the machine remains practically unchanged despite of a raising of the inlet temperature. So it can be concluded that, the result from this model shows that the growth of enthalpy drop is almost perfectly balanced by the reduction in mass flow rate, and therefore, for the purposes of power extraction, increasing the temperature of superheating is useless.

On the other hand, the degree of superheat of the inlet fluid is responsible for setting the temperature level from which the fluid begins to exchange thermal power with the metal wall in the cooling process modeled at the inlet

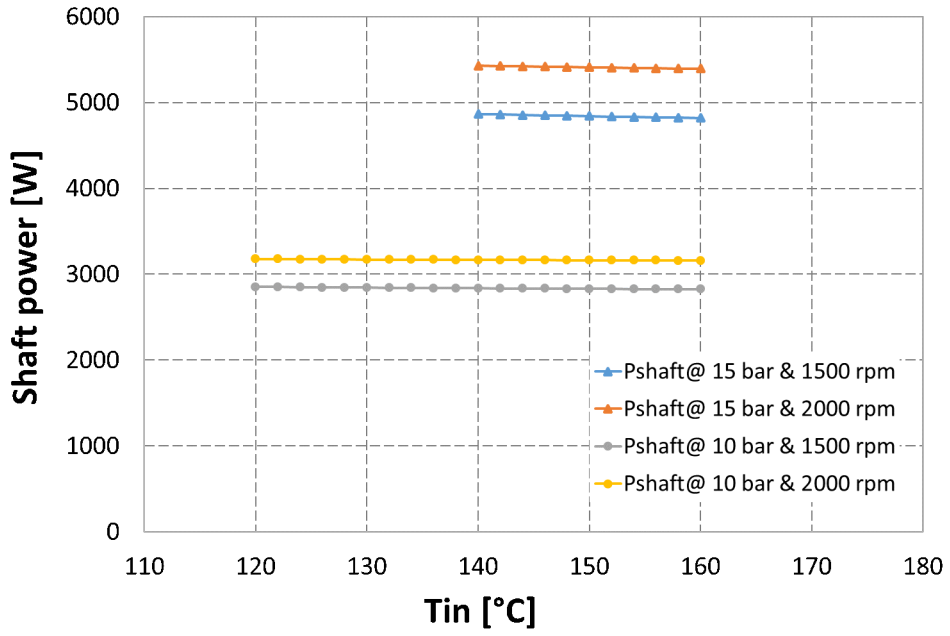

Figure 6.10: Shaft power vs inlet temperature for four cases

of the machine. In fact this thermal power is an important input fraction of the energy balance to the metal wall of the volumetric machine, like the power lost by friction, as mentioned above, and then it is guilty to raise the wall temperature, which leads inevitably to thermal dispersions towards the environment.

As shown in Figure 6.11, the thermal power dissipated inevitably increases with input temperature for all curves, leading a deterioration of the thermodynamic first principle efficiency. So from this point of view, it is necessary to keep the inlet fluid temperature as close as possible to the saturation temperature, with an indispensable delta T of superheating for not breaking into the bell-shaped curve, otherwise the deterioration in the performance of the global thermodynamic cycle.

As shown in Figure 6.11, the curves that are in the highest section of the chart dissipate more heat. These present the characteristics of having a higher shaft speed and a lower expansion ratio. The first is responsible for contributing in raising the temperature of the metal wall, as high rotational speeds mean higher power lost by friction in the energy balance to the wall, as explained in the section above.

The second characteristic is involved in heat transfer because at lower inlet pressures, discharge temperatures are higher, at the same condensation pressure, and therefore the contribution of the heat transfer with the wall, at the

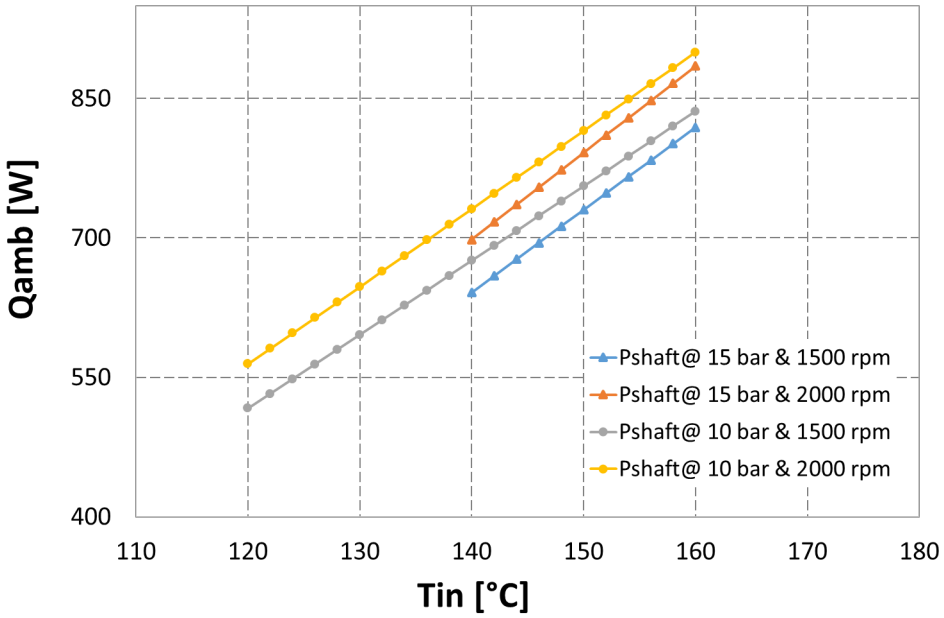

Figure 6.11: Heat loss vs inlet temperature for four cases

exhaust of the machine, can be significant, going to increase the losses to the surroundings.

6.1.4 Scroll expander insulation

After having presented the non-adiabatic behavior of the scroll expander under study, a question could be raised to understand how the machine would behave in the case of ideal insulation (no heat loss to the surroundings). The idea was to see if heat losses detected by the model could be converted completely, or at least in part, into fruitful work, and so if it was worth an effort to find a solution to insulate the machine as much as possible. With reference to Figure 6.12, the wall temperatures are shown for the case with the ambient heat transfer coefficient obtained from the calibration and the case in which this coefficient is set to zero. All the curves are plotted with reference to constant shaft speed (of 1500 rpm) to explain the dynamics that occurs in this situation. Since in the case of the perfectly insulated expander the major flux in the wall energy balance disappears, consequently it spreads on the remaining heat fluxes. In order to match this goal, the solution of the energy balance provides an increased wall temperature which only influences the heat transfers of the internal fluid, being unchanged the contribution of power given by metal sliding. This means that both the outlet

temperature from isobaric cooling and the one of the outlet heating at the discharge pressure are higher in the case of insulated expander. As regards the increase of the outlet temperature from the cooling process, it has the same effect noted for the superheated temperature, i.e higher temperatures bring about higher enthalpies, but the same produces a contrasting expansion of the fluid at constant pressure that causes mass flow rate reduction. In other words, a substantial gain in power extracted from the expander is negligible. Regarding the higher temperature at the machine output, it can be observed that this additional heat duty is no longer useful for the purposes of the conversion of heat into work, being at the exhaust of the machine. To give it a useful role, it is worthy of consideration for cogeneration, thanks to outlet temperature levels of around 100 $°C$. As a matter of fact finding publications in literature relating to cogeneration by means of micro-CHP-ORC system is not rare.

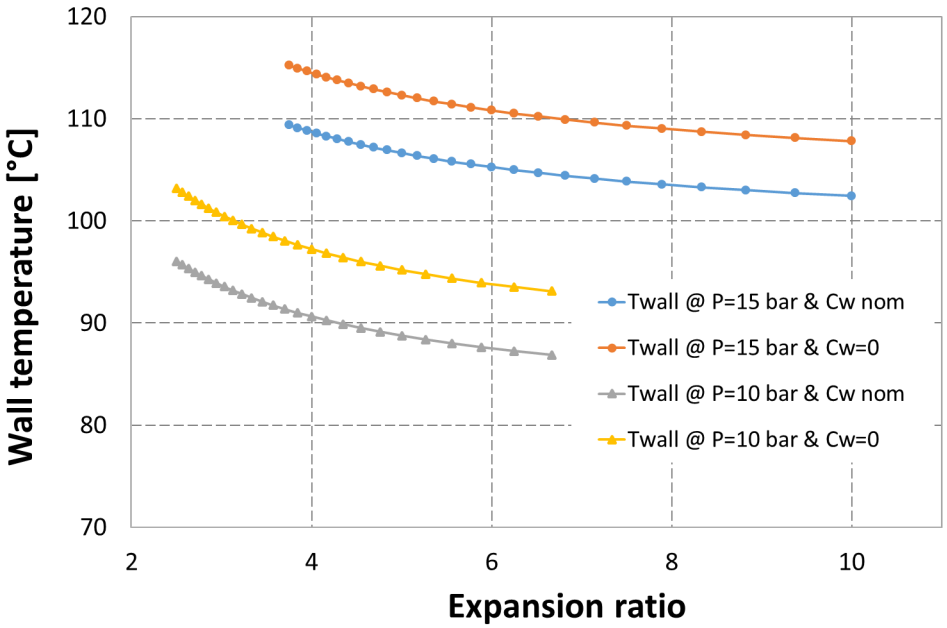

Figure 6.12: Twall vs inlet temperature for four cases

6.2 Simulation of the operating maps

In order to strengthen the numerical investigation regarding the scroll expander performance, operation maps are simulated to have a broad view of its behavior, by varying the main system parameters, i.e. shaft speed and expansion ratio. Since it has been found that the inlet temperature of the

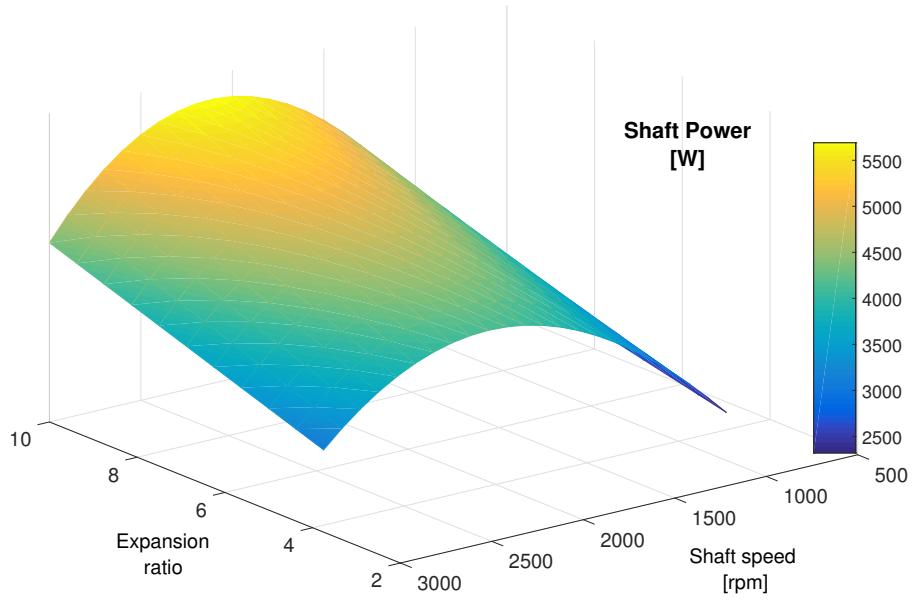

Figure 6.13: Shaft power in 3-D representations

machine must be set as much as possible close to that of saturation at the corresponding pressure, avoiding at the same time to enter the two-phase region, it does not constitute an important parameter to be included the next analysis.

The next graphs are especially useful to the ORC-facility designer in the initial phase of the project, because they enable him to obtain the performance values and thus decide the convenience of economic investment by the knowledge of few informations coming from the boundary conditions concerning the installation site. In Figure 6.13 and 6.14, the three-dimensional graphs of the shaft power and expansion efficiency can be observed. The trends of these surfaces have been widely explained in the previous sections. In fact, the power always increases with the expansion ratio, despite the efficiency decreases smoothly. Both surfaces have a maximum for a given shaft speed and are strongly penalized by the increases in power lost by metal friction when the revolution speeds increase a lot.

A convenient representation to obtain a complete view of the expander operation range and its performance is to create 2D charts with points that have the same value of a given property. Being 2D-graphs, curves containing different informations may be superposed in order to complete the knowledge of the operating point. Figure 6.15 and 6.16 represent two working map with

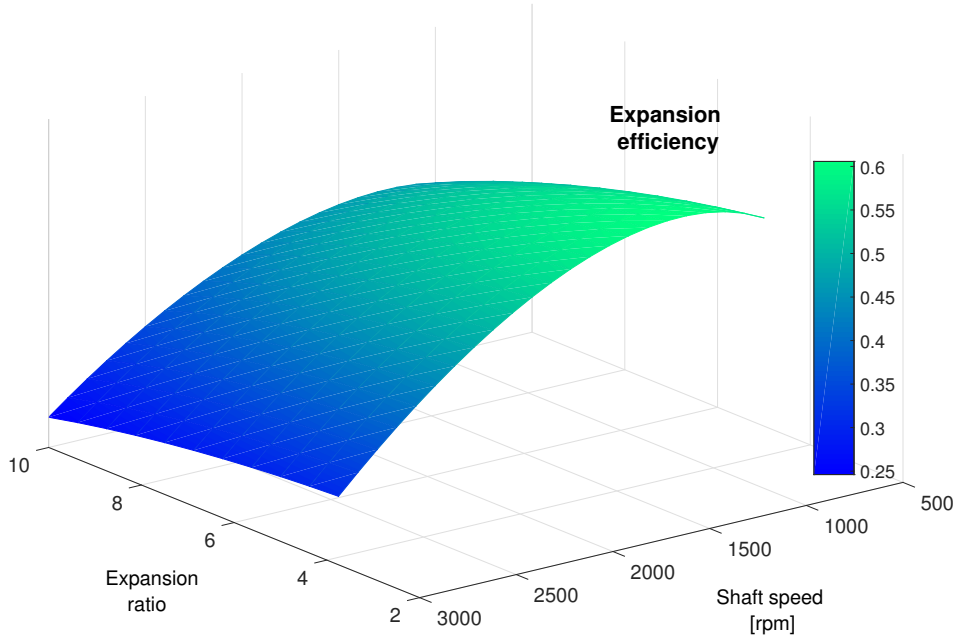

Figure 6.14: Expander efficiency in 3-D representations

curves of iso-power and expansion efficiency by changing the shaft speed and the expansion ratio.

The idea comes from the analogy with internal combustion engines (ICEs), already treated in Chapter 3 for the modelling of friction losses, and also adopted in this case for the sake of convenience. In fact, even in the case of ICEs, the same graph is obtained, where instead of the expansion ratio there is the mean indicated pressure in the cylinder, which is commonly referred to as "engine load". In this case, the expansion ratio is very close to that parameter but it is more useful for the integration of the scroll expander in a power plant.

With reference to Figure 6.15, the curve of iso-power 4.5 kW can be observed as an example. It lies almost entirely between the two iso-efficiency lines between 45 and 55%. This means that the designer could run the machine in a wide range of operating points despite the mechanical power and the performance efficiency remain unchanged. In any case it is possible to predict the behavior of the system for any expansion ratio-shaft speed couple.

If one refers now to the operating map illustrated in Figure 6.16, the same informations of the previous map can be obtained, except that the expansion ratio depends on a condensing pressure set at 1.5 bar, and by varying the

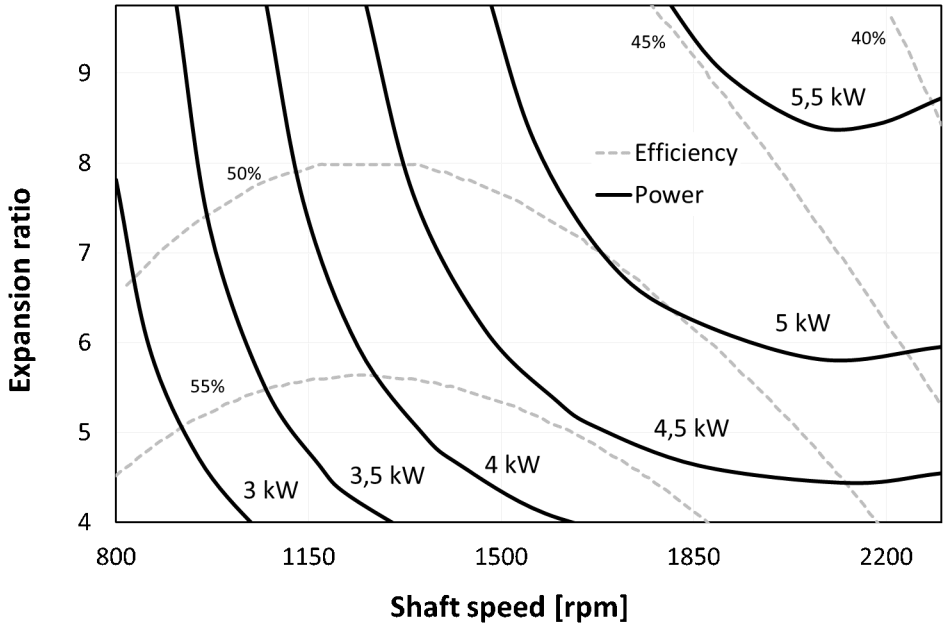

Figure 6.15: 2D maps by varying the expansion ratio by means of the condensation pressure. The inlet temperature is fixed at the saturation temperature of 15 *bar* plus 8 K

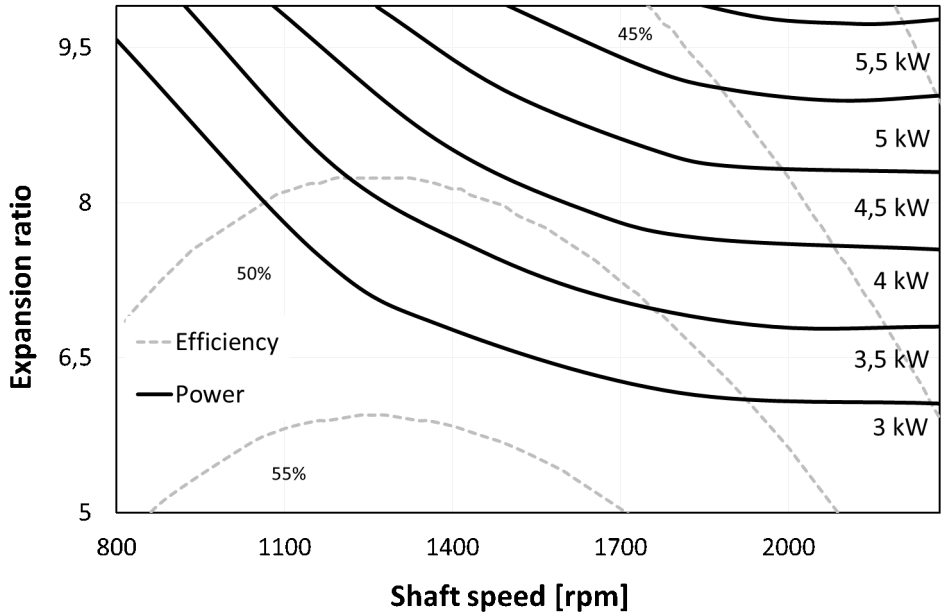

Figure 6.16: 2D maps by varying the expansion ratio by means of the evaporation pressure. The condensation pressure is set to 1.5 *bar*, and the inlet temperature is fixed at the saturation temperature plus 8 K

inlet expander pressure from 7 to 15 *bar*.
One can observe that all the iso-power curves are drawn in areas of the map at lower efficiencies, as also shown in the previous Figure 6.1, for the fact that the extraction of work begins at lower temperatures, so going to decrease the ideal power obtainable from a Carnot machine. Once again is therefore extremely important, when possible, controlling the off-design performance by varying the discharge pressure instead of the evaporation one, otherwise heavy penalties in expansion process efficiency will occur.

6.3 Exergy analysis

As mentioned in Chapter 3, in this subsection, 3 example cases are presented to understand how the irreversibility of the transformations plays a crucial role in the power losses, theoretically exploitable from the scroll expander. This power is the exergy loss marked as $\mathring{W}_{diss}$ in Eq. (3.53). The 3 cases object of the analysis present the same shaft power fixed to 4.5 kW. As it can be seen from the operation map in Figure 6.15, the 4.5 kW iso-power curve extends for a wide range, for both the shaft speed and the expansion ratio.
It was thought then to take the two extreme couple parameters (N and β) of this curve and a couple in the middle, in order to appreciate the change in relative terms of the transformation irreversibility involved in the expansion model. All cases have an evaporation pressure equal to 15 *bar* and a ΔT of superheating equal to 8 K, so the conditions at the entrance are the same and therefore also the exergy of the inlet stream is the same. The first case has the highest shaft speed (2300 *rpm*) and the lowest expansion ratio (about 4.5) with the condensing pressure equal to 3.3 *bar*.
The second case has a speed of 1600 *rpm* and a condensing pressure of 2.8, and the third has the lowest shaft speed (1250 *rpm*) and the highest expansion ratio (about 10) with the minimum condensation pressure equal to 1.5 *bar*. Figures 6.17, 6.18 and 6.19 show the evolution of the power lost due to irreversibility, from case 1 to 3. Starting from the pressure throttling as the first process, it assumes a gradually decreasing relative weight, even if modest. This is justified by the fact that, in order to provide the same power with a reduced expansion ratio, the mass flow rate has necessarily to increase, along with the pressure throttling, that catches up to 6% of the total power losses in case 1, which has the highest mass flow rate. It decreases as soon as the mass flow rate decreases.
Focusing on heat transfers, these are never significant as regards the losses because the wall temperature is always intermediate between the inlet and

outlet temperature of the fluid, while the expansion temperature drop is always rather limited. Consequently, the irreversibility for internal temperature "gaps" are negligible. The losses given by the constant volume transformation increases as the expansion ratio is far from the adapted condition from case 1 to case 3, according to the conclusions of the previous sections. In fact, the work extraction involves the isoentropic and the isovolumic processes, and the latter is less efficient than the isoentropic one, which is the more important as the condensation pressure moves away from the adapted-discharge pressure of the scroll geometry.

The losses related to leakages are approximately constant, around 10% of the power losses. This is explained by the fact that, since there are always chocking conditions in the throat of the simply convergent nozzle that models the leakage losses, also the leakage flow is proportional to the mass flow rate processed at the inlet of the machine and the percentage remains almost constant.
Focusing now on the losses related to the mixing process, they take an important role in all the analyzed cases, while they have an increasing trend going from the case 1 to case 3. This is explained by the fact that the condensation pressure is very far from the pressure in the throat nozzle (less far for cases 1 and 2), and consequently the mixing of the two flow rates have big difference in pressure that causes a detrimental exergy dissipation.
Regarding the power lost by metal friction between the spirals, it can be said that it is absolutely destructive in terms of exergy loss, catching the peak of 48% in the case at the maximum shaft speed. This result is explained by the fact that this net shaft power is degraded into heat and re-injected into the energy balance of the metal envelope.
Finally, the power lost given by heat loss to the environment can be analyzed. If energy balances in the control volume revealed that this term occupied a large part of the involved power, the exergy analysis reveals that it is not so important for expander irreversibility, as it is a relatively low temperature heat source, and so not very interesting in terms of work extraction, if "filtered" with the Carnot efficiency. In none of the cases it exceeds a level of 5.5% of the exergy lost.
From these results the irreversibility due to bad design of machine and those that come from a wrong choice of scroll internal geometry are highlighted. Thus, exergy analysis can figure out the aspects that have to be focused if a new micro-ORC scroll expander is designed. (Once again, one has to remember that the expander adopted in this work come from a bus air conditioning system, i.e. a compressor slightly modified to operate as an expander).
Always with reference to Figure 6.17, 6.18 and 6.19, it can be seen that the leakage mass flow rate is significant as regards the exergy dissipation, because

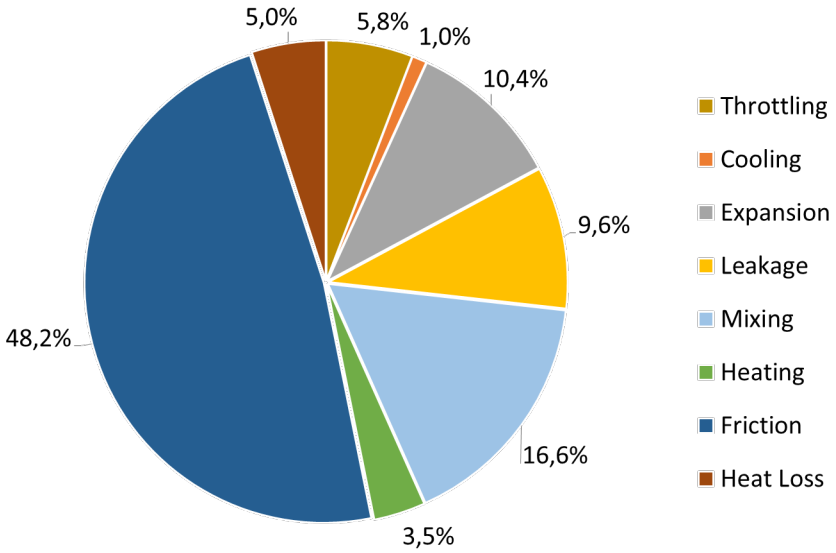

Figure 6.17: Case 1: Relative weights of the exergy losses for an output shaft power of 4.5 kW with inlet pressure of 15 bar and $Tevap$ + 8 K as inlet temperature; N=2300 rpm & $\beta \cong 4.5$;

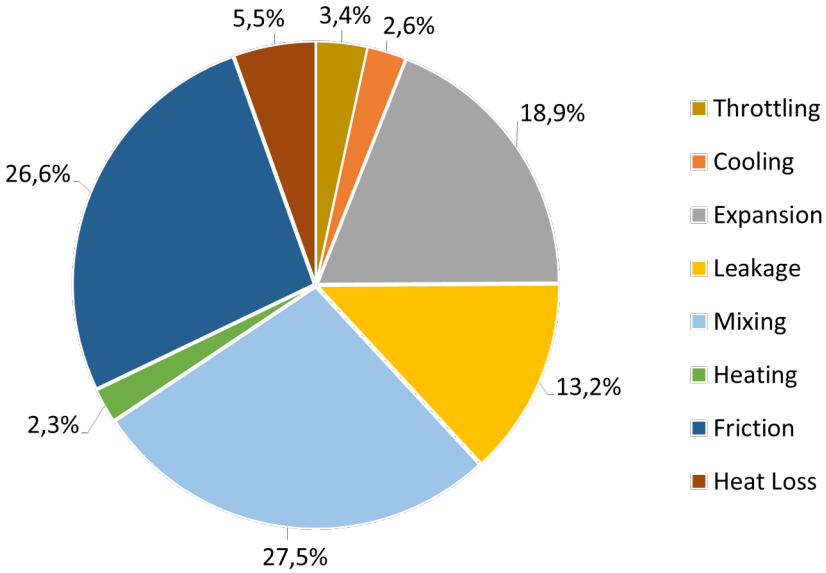

Figure 6.18: Case 2: Relative weights of the exergy losses for an output shaft power of 4.5 kW with inlet pressure of 15 bar and $Tevap$ + 8 K as inlet temperature; N=1600 rpm & $\beta \cong 5.5$

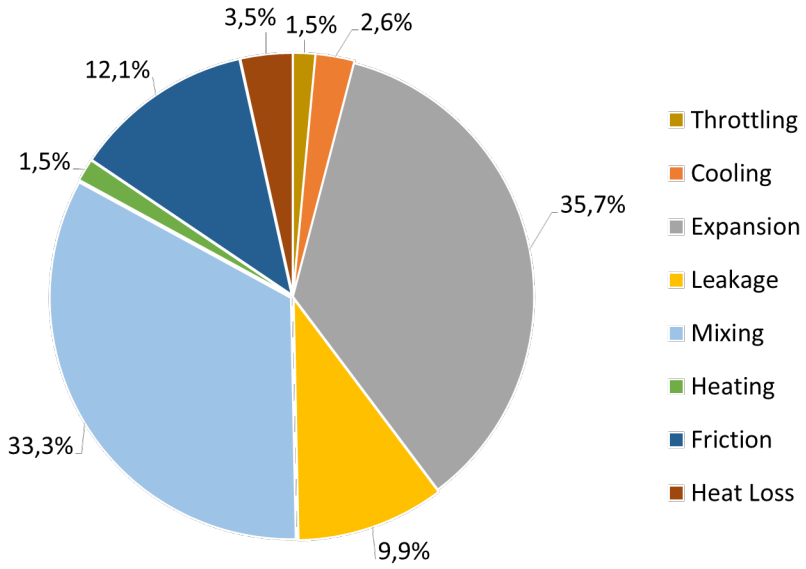

Case 3

Figure 6.19: Case 3: Relative weights of the exergy losses for an output shaft power of 4.5 kW with inlet pressure of 15 bar and $Tevap + 8\ K$ as inlet temperature; N=1250 rpm & $\beta \cong 10$

it affects both the leakage and mixing losses, accounting together for about 27% in the first case, 41% in the second and 43% in the third. It is clear therefore that a great attention to the sealing on both radial and axial gaps must be dedicated. If in the first case the leakage losses are reduced, another critical irreversibility of this machine increases inexorably: the one related to the net power losses given by metal friction. In fact, to provide the same power with a lower expansion ratio, the shaft speed must inevitably increase, at the expense of the net power obtainable from the expander. Then an additional note for the scroll expander designer is the capability of creating a good lubrication regime where the metal slides.
In conclusion it can be seen from Figure 6.17, 6.18 and 6.19 that the sum of the losses related to leakage and those related to the friction dissipation are equal to about 75% in the first case, 68% in the second and 55% in the third case, and have an opposite trend passing from the first to the last case. Where one increases, the other decreases, so a favorable situation for both losses could be never provided. The last big loss is due to the bad choice of the machine as regards the BVR, which must always be as close as possible to the adapted expansion ratio of the machine in its nominal operating

point, otherwise irreversible losses led by the expansion at constant volume increase. Thus it can be seen in the last case that the expansion losses are the highest because the expansion ratio is more far from the adapted condition ($\beta_{adapted} = BVR^{\gamma}$), which is about 3.14 for this expander.

Conclusions

With the present work attention has been focused on a volumetric scroll expander for use in a micro-ORC power plant based on an experimental campaign on a range of operation. The core of this work is the realization and the next implementation in Matlab environment of a scroll expander model starting from a model present in literature, here thoroughly revisited by physic and thermodynamic points of view. The proposed model describes the expander performance and investigates its behavior over a wide operating range. The main outputs that the micro-ORC designer is able to get from this model are the mass flow rate processed, the shaft power and the outlet expander temperature. The most significant results are described below:

- The performance of the expander is strongly influenced by the expansion ratio and the shaft speed. As regards the first, it can be said that the power always increases with the expansion ratio, even if the isoentropic efficiency seriously reduces when moving from the so-called adapted expansion ratio, which is a function of the machine internal geometry, i.e. the Built-in-Volume-Ratio (BVR). This happens because moving from the adapted condition led by an isoentropic expansion, the remaining part of the expansion is obtained by means of a constant volume expansion, less efficient than the isoentropic one.

- As regards the shaft speed, the machine is heavily penalized at the highest speed revolutions, because despite an increase in the mass flow rate processed, the net power losses caused by friction between the metal scrolls in motion are preponderant. Consequently, the expander efficiency always presents a maximum for a given shaft speed.

- As regards the expander inlet temperature the model suggests that it should always be as close as possible to the saturation temperature for the inlet pressure, unlike the conventional Rankine steam cycles where a high degree of superheating is always practiced. This is caused by the fact that for these volumetric machines, the increase in temperature causes an increase in enthalpy available but, in a contrasting way, the

density of the fluid entering the expansion chambers reduces, and then at same volumetric flow rate, the mass flow rate decreasing, leading to negligible increase in shaft power. Furthermore, an increase of the inlet temperature means an increase of heat losses to the external envelope, and this fact is the reason why these machines cannot be considered adiabatic. In addition, elevated degree of superheating led by greater heat transferred to evaporator bring about a reduction of the overall thermodynamic cycle efficiency.

- Assuming a perfect insulation for the external envelope, it turns out that the energy balance of the wall rearranges the heat fluxes, discharging the power dissipated to the outlet fluid, without changing significantly the obtainable shaft power. For this reason it is reported that a possible insulation is worth only in the case of a cogeneration micro-ORC plant, where the expander thermal power dissipation is potentially recoverable, otherwise the scroll insulation means an oversizing of the condenser.

- In the light of the model sensitivity by the various operating parameters, it was considered useful to create 2D and 3D operation maps, in analogy with internal combustion engines (ICEs), representing iso-power and iso-efficiency curves, where the shaft speed and the expansion ratio are varied, while the inlet temperature is fixed and closed to that of saturation, in order to get a clear overview of the scroll expander performance over a wide operating range.

- Finally, an exergy analysis of the transformations involved in the model was conducted: the major irreversibility of the process can be attributed to both a bad design of the expander (note that, because the recent interest in micro-ORC system, expanders investigated in literature originated from compressors slightly modified to operate in reverse mode as expanders), and the wrong choice of the scroll BVR. In fact, it was discovered that the leakage mass flow rate and the deterioration of the net useful power into heat due to friction are the main responsible of the exergy losses linked with the machine design. The first is responsible for both the lower mass flow rate available in the expander chambers and irreversible mixing between the high pressure flow coming from the nozzle used to simulate the leakages, and the outlet constant volume expansion (at condensation pressure). Therefore the exergy dissipation is very important. As regards the choice of the machine for a given application, it is reminded once again that the expansion ratio in nominal conditions has to be as close as possible to the

adapted one. From this exergy analysis both the pressure throttling at the entrance and the internal and external thermal exchanges are practically negligible if compared to the just mentioned irreversibility.

As regards the future developments of this work, the proposed model for the investigated machine could be used with other working fluids, in order to test the scroll expander behavior for the better performance. These simulation will guide the choice for the fluid that better characterizes the behavior of the expander in terms of power output and efficiency. Ultimately, an elevated number of investigated scroll expander, from an experimental and theoretical point of view, is useful for a future analysis oriented to investigate similarity laws, currently available for turbomachinery only.

Bibliography

[1] T. Yanagisawa, T. Shimizu, M. Fukuta, T. Handa, Study on fundamental performance of scroll expander, Trans. Jpn. Soc. Mech. Eng. Ser. B 54 (1988) 2798e2803.

[2] R. Zanelli, D. Favrat, Experimental investigation of a hermetic scroll expander-generator, in: Proc. Int. Compress. Eng. Conf., Purdue, 1994 (Paper 1021).

[3] M. Kane, D. Larrain, D. Favrat, Y. Allani, Small hybrid solar power system, Energy 28 (2003) 1427e1443.

[4] J.A. Mathias, J.J.R. Johnston, J. Cao, D.K. Priedeman, R.N. Christensen, Experimental testing of Gerotor and scroll expanders used in, and Energetic and Exergetic modeling of, an organic rankine cycle, J. Energy Resour. Tech. 131 (2009) 1e9.

[5] V. Lemort, S. Declaye, S. Quoilin, Experimental characterization of a hermetic scroll expander for use in a micro-scale Rankine cycle, P. I. Mech. Eng. A-J. Pow. 226 (2012) 126e136.

[6] R. Bracco, S. Clemente, D. Micheli, M. Reini, Experimental tests and modelization of a domestic-scale ORC (organic Rankine cycle), Energy 58 (2013) 107e116.

[7] S.M.E. Hoque, Experimental investigation of an R134a based organic Rankine cycle, Master Dissertation, University of Ontario Institute of Technology, 2011.

[8] L. Guangbin, Z. Yuanyang, Y. Qichao, W. Le, T. Bin, L. Liansheng, Theoretical and experimental research on scroll expander used in small scale organic Rankine cycle system, P. I. Mech. Eng. E-J. Pro. (2013), http://dx.doi.org/ 10.1177/0954408913506701.

[9] M. Jradi, J. Li, H. Liu, S. Riffat, Micro-scale ORC-based combined heat and power system using a novel scroll expander, Int. J. Low-Carbon Tech. 9 (2014) 91e99.

[10] T. Saitoh, N. Yamada, S.-i. Wakashima, Solar rankine cycle system using scroll expander, J. Environ. Eng. 2 (2007) 708e719.

[11] D. Manolakos, G. Papadakis, S. Kyritsis, K. Bouzianas, Experimental evaluation of an autonomous low-temperature solar Rankine cycle system for reverse osmosis desalination, Desalination 203 (2007) 366e374.

[12] H. Wang, R.B. Peterson, T. Herron, Experimental performance of a compliant scroll expander for an organic Rankine cycle, P. I. Mech. Eng. A-J. Pow. 223 (2009) 863e872.

[13] B.J. Woodland, J.E. Braun, E.A. Groll, W.T. Horton, Experimental testing of an organic Rankine cycle with scroll-type expander, in: Proc. Int. Refrig. Air Cond. Conf., Purdue, 2012 (Paper 52).

[14] B. Twomey, Experimental test results from QGECE laboratory small-scale organic Rankine cycle using a scroll expander, Queensland Geothermal Energy Centre of Excellence, 2012. http://espace.library.uq.edu.au.

[15] R. Peterson, H. Wang, T. Herron, Performance of a small-scale regenerative Rankine power cycle employing a scroll expander, P. I. Mech. Eng. A-J. Pow. 222 (2008) 271e282.

[16] V. Lemort, S. Quoilin, C. Cuevas, J. Lebrun, Testing and modeling a scroll expander integrated into an organic Rankine cycle, Appl. Therm. Eng. 29 (2009) 3094e3102.S. Quoilin, Sustainable Energy Conversion Through the Use of Organic Rankine Cycles for Waste Heat Recovery and Solar Application, Doctor Dissertation, University of Liege, 2011.S. Declaye, S. Quoilin, L. Guillaume, V. Lemort, Experimental study on an open-drive scroll expander integrated into an ORC (organic Rankine cycle) system with R245fa as working fluid, Energy 55 (2013)

[17] S. Declaye, S. Quoilin, L. Guillaume, V. Lemort, Experimental study on an open-drive scroll expander integrated into an ORC (organic Rankine cycle) system with R245fa as working fluid, Energy 55 (2013) 173e183.

[18] S. Quoilin, Sustainable Energy Conversion Through the Use of Organic Rankine Cycles for Waste Heat Recovery and Solar Application, Doctor Dissertation, University of Liege, 2011.

[19] B. Aoun, D.F. Clodic, Theoretical and experimental study of an oil-free scroll vapor expander, in: Proc. Int. Compress. Eng. Conf., Purdue, 2008 (Paper 1925).

[20] N. Zhou, X. Wang, Z. Chen, Z. Wang, Experimental study on organic Rankine cycle for waste heat recovery from low-temperature flue gas, Energy 55 (2013) 216e225.

[21] AirSquared, 2012. http://airsquared.com/products/expanders (accessed 20.10.13).

[22] Eneftech, 2013. http://www.eneftech.com/ (accessed 20.10.13).

[23] H.J. Kim, J.M. Ahn, I. Park, P.C. Rha, Scroll expander for power generation from a low-grade steam source, P. I. Mech. Eng. A-J. Pow. 221 (2007) 705e711.

[24] K. Mayer, Research, development and demonstration of micro-CHP system for residential applications, ECR Int. (2010), http://dx.doi.org/10.2172/ 1011855 (DOE/NT/42216).

[25] Zheng Miao, Jinliang Xu, Xufei Yang, Jinghuang Zou,Operation and performance of a low temperature organic Rankine cycle, Applied Thermal Engineering 75 (2015) 1065e1075.

[26] H. Liu, Y. Shao, J. Li, A biomass-fired micro-scale CHP system with organic Rankine cycle (ORC) e thermodynamic modelling studies, Biomass Bioenergy 35 (2011) 3985e3994.

[27] B. Saleh, G. Koglbauer, M. Wendland, J. Fischer, Working fluids for lowtemperature Organic Rankine Cycles, Energy 32 (2007) 1210e1221.

[28] B.F. Tchanche, G. Papadakis, G. Lambrinos, A. Frangoudakis, Fluid selection for a low-temperature solar organic Rankine cycle, Appl. Therm. Eng. 29 (2009) 2468e2476.

[29] D. Mikielewicz, J. Mikielewicz, A thermodynamic criterion for selection of working fluid for subcritical and supercritical domestic micro CHP, Appl. Therm. Eng. 30 (2010) 2357e2362.

[30] D. Wang, X. Ling, H. Peng, L. Liu, L. Tao, Efficiency and optimal performance evaluation of organic Rankine cycle for low grade waste heat power generation, Energy 50 (2013) 343e352.

[31] H. Xi, M.J. Li, C. Xu, Y.L. He, Parametric optimization of regenerative organic Rankine cycle (ORC) for low grade waste heat recovery using genetic algorithm, Energy 58 (2013) 473e482.

[32] J. Manzagol, P. d'Harboullé, G. Claudet, G. Gistau Baguer, Cryogenic scroll expander for Claude cycle with cooling power of 10 to 100 watts at 4.2 K, in: Proceedings of the Cryogenic Engineering Conference – CEC AIP Conference, Advances in Cryogenic Engineering (2002) 267–274.

[33] F.P. Incropera, P.D. De Witt, T.L. Bergman, A.S. Lavine, Introduction to Heat Transfer, fifth ed., John Wiley & Sons, 2007.

[34] N.P. Halm, Mathematical modeling of scroll compressors, Master Thesis, Purdue University, West Lafayette, IN, 1997.

[35] W.H. MCADAMS, Heat Transmission, New York, McGraw-Hill, 1954.

[36] K.T. Ooi, J. Zhu, Convective heat transfer in a scroll compressor chamber: a 2-D simulation, International Journal of Thermal Sciences 43 (2004) 677–688

[37] C. Cuevas, J. Lebrun, V. Lemort, E. Winandy, Characterization of a scroll compressor under extended operating conditions, Applied Thermal Engineering 30 (2010) 605–615

[38] L. C. Mendoza , J. Navarro-Esbrí, J. C. Bruno, V. Lemort, A. Coronas, Characterization and modeling of a scroll expander with air and ammonia as working fluid, Applied Thermal Engineering 70 (2014) 630e640